Convective Boundary Mixing in Simulations of Massive Stars

by

Austin Davis
B.Sc., University of Victoria, 2014

A Thesis Submitted in Partial Fulfillment of the
Requirements for the Degree of

MASTER OF SCIENCE

in the Department of Physics & Astronomy

Convective Boundary Mixing in Simulations of Massive Stars

by

Austin Davis
B.Sc., University of Victoria, 2014

Supervisory Committee

Dr. Falk Herwig, Supervisor
(Department of Physics & Astronomy)

Dr. Katherine Prestridge, Member
(Department of Physics & Astronomy)

Dr. Jody Klymak, Outside Member
(Department of Earth & Ocean Science)

ABSTRACT

The turbulent convective mixing in the late stage evolution of the core of massive stars is not well understood. One-dimensional (1D) codes that simulate the lifetime of stars rely on models with free parameters in order to model convection. The free parameter determining the strength of the mixing across the boundary of a convection zone is undetermined for the majority of convective boundaries. In this thesis, the effects of convective boundary mixing (CBM) in stellar evolution models is investigated with a focus on the structural changes to massive star cores. An estimate for the amount of mixing present at a convective boundary is made from a three-dimensional O-shell simulation. Using this value, a set of simulations are computed in the 1D stellar evolution code, MESA, that test the effects of CBM of massive star carbon-oxygen (CO) cores.

A three-dimensional (3D) simulation of the O-shell in a $25\mathrm{M}_{\odot}$ stellar model with $Z = 0.02$ is summarized with a focus on determining the diffusion coefficient that would be necessary in a 1D stellar evolution model to reproduce the spherically averaged composition profiles. The diffusion coefficient was then fit with the exponential decaying CBM model (Freytag, Ludwig & Steffen, 1996) and the free parameter, f_{CBM}, was determined.

The sensitivity of the late time evolution of the core in a $25\mathrm{M}_{\odot}$ 1D stellar model at $Z = 0.02$ with respect to variation in the value of f_{CBM} was tested. The goal of this work was not to determine what values of f_{CBM} the stellar model should have, but to investigate the differences in the structure as a result of changing the f_{CBM} values. Past the onset of convection in the first C shell, the values of f_{CBM} change the structure of the star significantly, promoting dredge-ups that mix material from the core to the top of the C shell. The presupernova structure was investigated with a focus on the compactness parameter, $\xi_{2.5} = 2.5\mathrm{M}_{\odot}/R(2.5\mathrm{M}_{\odot})$. The models show significant non-monotonic variation in $\xi_{2.5}$ with respect to f_{CBM}, where $\xi_{2.5}$ spans a range of $(0.12, 0.35)$. The abundances near collapse of the models were also investigated. It was found that Ne ash that was entrained into the C shells through dredge-ups and shell mergers was transported high enough in the star to be ejected by the supernova explosion.

Informed by 3D simulations, this study shows that for values of f_{CBM} for the exponentially decaying CBM model, ranging from $(0.002, 0.032)$, significantly affect the structure of the CO core. Interaction between the carbon (C), neon (Ne) and

oxygen (O) convective shells change the core boundaries and therefore the structure. Although, during Si core burning the affect of the interaction is monotonic, as the simulations collapse shortly after this. The structure of the CO core determines the value of $\xi_{2.5}$, determining whether the model will explode.

Contents

List of Tables

List of Figures

ACKNOWLEDGEMENTS

I would like to thank Dr. Falk Herwig for the generous support and the opportunities he has given me, without which, this work would not exist. And Dr. Katherine Prestridge for providing the wonderfully fulfilling work terms at LANL and accepting the inherent dangers of letting a theorist into her lab. I would also like to thank Dr. John Charonko for teaching me so much in such a short period of time, my family for having patience with me during this degree and Ms. Mara Johnson-Groh, BA, MA for dreaming of Ocean Falls when she should have been leaving me alone to work.

DEDICATION

To anyone who ever thought to themselves, “I wondered what would happen if I changed this default parameter?”

Chapter 1

Introduction

"A thorough theoretical treatment of convective motions and transport of energy is extremely difficult. ...[In] many astrophysical problems... the bottle-neck preventing decisive progress is the difficulty involved in solving the well-known hydrodynamic equations." Dr. Rudolf Kippenhahn, Kippenhahn & Weigert (1990)

1.1 Background

Stars form out of gas clouds primarily composed of H. Small amounts of metals (elements with a higher atomic number than He) can be deposited into the gas cloud from previous stellar events such as stellar winds and supernova explosions. Although the metal content in these clouds is small, pollutants such as C, N and O act as catalysts during H burning, and the inclusion of metals increases the opacity, leading to stronger stellar winds. A massive star is a star with a zero age main sequence mass of $\gtrsim 8M_{\odot}$. A simplistic view of the end of a massive star's life is that it will either explode as a type II supernova, producing a neutron star remnant or collapse onto itself creating a black hole. In the former case, the supernova will process the elements created in the core, enriching the surrounding area. In the latter case, the material will fall into the black hole. The core structure of the star has an impact on whether a black hole or neutron star will be produced, and that structure is dependent on the convective mixing throughout the evolution.

To determine the core structure of a massive star, idealized models are computed. The original stellar models were computed by hand as this excerpt from Kippenhahn & Weigert (1990) describes, which includes a quote from Martin Schwarzschild.

"The growth of computing facilities by leaps and bounds since the 1960's may be illustrated by the remarks of ...[Schwarzschild (1958)] *: 'A person can perform more than twenty integration steps per day', so that 'for a typical integration consisting of, say, forty steps, less than two days are needed'. The situation has changed drastically since those days when the scientist's need for meals and sleep was an essential factor in the total computing time for one model."* [pg.77]

Current 1D codes such as MESA (Paxton et al., 2011, 2013, 2015) simulate the structure and evolution of the star with considerably more accuracy than pencil and paper, although still fall short of providing an accurate and precise picture of what is actually happening in a star. Models such as mixing length theory (MLT) act to treat the highly turbulent convective flows within the star as locally diffusive, neglecting the dynamics of the fluid instabilities that would act to mix material across convective boundaries. Different models for convective boundary mixing (CBM) have been proposed by Freytag, Ludwig & Steffen (1996) and Roxburgh (1989) (among others), all of which extend the convective boundary into the stable fluid surrounding the convection zone. Herwig (2000) tested the variation in the CBM strength on the pulse driven convection zone during the He-flash in intermediate mass stars using the model by Freytag, Ludwig & Steffen (1996). The study showed a larger more efficient third dredge-up and a C enhancement signature with increased CBM (or overshooting), among other things. To date, the variation in CBM has not been studied for 1D massive star models.

1.2 Time Scales in Stellar Evolution

The evolutionary stages of stars span a wide range of time scales. Main sequence lifetimes can be on the order of billions of years, whereas core Fe burning in massive stars can take hours. The nuclear time scale characterizes the core burning lifetime of a star. The thermal time scale gives the pre-main sequence lifetime and well as the length of time needed for the core to contract and start the next evolutionary phase. The dynamic time scale is on the order of the sound crossing time and characterizes the unsupported collapse of a massive star core. The convective turnover time scale gives the amount of time needed to mix material across a convection zone. During most of the evolution, these time scales are separated by orders of magnitude and all characterize critical evolutionary periods in the star's life.

As a massive star evolves, its core burns through a series of elements. The burning in the core produces the luminosity necessary to balance the gravitational force, preventing the core from contracting further. After some time, the fuel is depleted and the support pressure disappears. Gravity acts to contract the core further and the temperature and pressure increase until the conditions are met for the next element to burn. If the burning from this element is exothermic, then support pressure is restored and the process continues. Massive star's burn through H, He, C, Ne, O, Si and Fe in these core burning stages. Fe burning is endothermic and does not provide the necessary support pressure to balance gravity, triggering a core collapse and marking the end of the star's life. Because of the different reactions and luminosities of the star during the core burning stages above, the lifetimes of these stages can change. If the star is assumed to be in hydrostatic equilibrium throughout the core burning stage, then the pressure gradient caused by the luminosity balances the gravitational contraction. The luminosity is produced by the conversion of mass into energy in the core which can be quantified if the reactions in the core are known. The energy produced in the core and the star's luminosity produce the nuclear time scale, given by

$$\tau_{\rm n} = \frac{E_{\rm n}}{L} \tag{1.1}$$

where L is the star's luminosity and $E_{\rm n}$ is the energy from the reactions in the core. In this equation, $E_{\rm n}$ must be taken as the energy released from the fuel that is available to be burnt. For example, during the main sequence, the core H supply is exhausted but an envelope of H is left surrounding the He core. Because massive stars typically have a convective core and a radiative envelope during the main sequence, the material found in the envelope cannot be transported to the core to burn and therefore does not contribute to the energy generation found there. For the sun, assuming that 10% of initial H is burnt in the core, $\tau_{\rm n} \approx 10^{10}$yr (Cox et al., 1968). For more advanced stages of burning $\tau_{\rm n}$ decreases. For a massive star, the main sequence lifetime is on the order of $10^6 - 10^7$yr, whereas the amount of time needed to evolve through C core burning to collapse is $\approx$ 1000yr. O and Ne core burning lasts on the order of months, Si burning is on the order of days.

After a core burning stage has ended, the core contracts and heats until the next core burning stage can begin. When the core burning stops the luminosity from that core burning stage is removed, leading to a deviation from hydrostatic

equilibrium. The star still has internal energy from the previous core burning that must be transported outward, allowing the star to contract. In this case, the internal energy creates a pressure gradient that resists the gravitational collapse preventing the freefall of the material in the star. An approximation for thermal time scale can be given if the assumption is made that there are no nuclear energy sources and the luminosity is constant. Oswalt & Barstow (2013) define this time scale as

$$\tau_{\rm therm} = \frac{U}{L} \tag{1.2}$$

where $\tau_{\rm therm}$ is the thermal time scale (or the Kelvin-Helmholtz time scale), U is the internal energy of the star and L the luminosity. In an idealized case, in which the star is assumed to be in hydrostatic equilibrium with no magnetic fields and is experiencing no mass loss, the internal energy can be approximated by the gravitational binding energy to within an order of magnitude and the thermal time scale is given by

$$\tau_{\rm therm} \approx \frac{GM^2}{RL} \tag{1.3}$$

where M and R are the mass and radius of the star. This is the time scale over which the star will balance thermally. The pre-main sequence happens on a thermal time scale as the gas cloud collapses until the temperature in the core is hot enough to fuse H. For the pre-main sequence of the Sun, $\tau_{\rm therm} \approx 3 \times 10^7$yr.

For the thermal time scale, internal energy provided support pressure to the star as it contracted. In the case of a core collapse supernova, the support pressure provided by the core is removed as the Fe core collapses into itself. Assuming there are no magnetic fields or significant mass loss, the star collapses under the force of gravity. The time scale on which this happens is the dynamic time scale and is given by

$$\tau_{\rm dyn} \approx \left(\frac{R^3}{GM}\right)^{1/2} \approx \frac{1}{(G\bar{\rho})^2} \tag{1.4}$$

where $\bar{\rho}$ is the mean density of the collapsing material. The dynamic time scale is approximately equal to the free fall time scale and also characterizes the sound speed. The dynamical time scale is the time scale at which dynamical information can propagate rather than the time scale for typical fluid dynamics in the star. For example, pressure waves from large convective fluctuations impacting a boundary travel on the dynamical time scale (Oswalt & Barstow, 2013). For the Sun, the dynamical time scale is $\tau_{\rm dyn} \approx$ 1hr (Oswalt & Barstow, 2013). For the Fe core

of a massive star about to collapse, $\tau_{\rm dyn} \approx 0.05$s. Although the shells of material surrounding the Fe core would still be burning at this point, providing luminosity, $\tau_{\rm dyn} \ll \tau_{\rm therm}$ so that the outer layers surrounding the core will still collapse on the dynamic time scale rather than the thermal time scale.

The three time scales given above characterize the major evolutionary time scales of stellar evolution. One other time scale that will become relevant in Chapter 3 and is important in characterizing convection in 1D modes is the convective turnover time scale. For a convective shell inside of a star, the convective turnover time scale is the amount of time needed for the convective flow to transport material from one boundary to the other. This is the amount of time to transport fuel entrained from the upper boundary down to the bottom of the convection zone where it can burn or transport heavier elements dredged up from below to the top where they may be ejected in the supernova explosion. The convective turnover time scale is given by

$$\tau_{\rm conv} = \frac{h}{\overline{|v_r|}} \tag{1.5}$$

where h is the height of the convection zone and v_r is the mean of the absolute value of radial velocity throughout the convection zone and is generally approximated by some form of radial velocity characteristic of the convection. When used with the MLT diffusive velocity (Section 1.3.1), $\tau_{\rm conv}$ gives an estimate for the larger convective timescales of the flow that would be possible in the convection zone. The convective turnover time scale of the Si core near the end of a massive star's life can be on the order of seconds.

At a given time in the star's life, the time scales above span orders of magnitude. In general, the nuclear time scale, thermal time scale and dynamic time scale are ordered as

$$\tau_{\rm n} \gg \tau_{\rm therm} \gg \tau_{\rm dyn} \tag{1.6}$$

For convective regions where the structure does not change rapidly over the lifetime of the convection zone, $\tau_{\rm therm} \gg \tau_{\rm conv} \gg \tau_{\rm dyn}$. Although, during very dynamic events such as supernova, possible mass ejection in POP III star's and shell mergers, the convective flow cannot be considered subsonic so it is possible for $\tau_{\rm conv} \approx \tau_{\rm dyn}$.

Despite the relatively large range of time scales found in the evolution of a star, the fluid dynamics found at $\tau_{\rm conv}$ (and much smaller for turbulent flows), have significant structural and evolutionary effects on the star.

1.3 Stellar Structure and Modelling

Star's are dynamic, gravitationally bound spheres of fluid. They are able to fuse elements in their cores, due to the release of gravitational potential energy. This fusion produces new elements as well as large amounts of energy that must be transported toward the surface by radiation and convection. The material produced by this nuclear burning can be mixed away from the core by convection. Fluid instabilities on convective boundaries, collectively referred to as convective boundary mixing (CBM) act as a catalyst, increasing the efficiency of the convective transport of material. If material from advanced burning stages in massive star's can be transported away from the core, then it is possible for that material to be ejected in the supernova explosion and go on to enrich further generations of stars.

Due to the range of time scales found in stellar evolution, codes used to solve the structure equations presented below use various assumptions in an attempt to simplify the problems. To simulate the lifetime of a star on the nuclear time scale, $\tau_{\rm n}$, 1D codes are used, which are unable to model fluids accurately. Diffusion is used in place of convection and the details of the fluid flows that determine how materials mix are not considered.

In order to investigate the effect of fluid dynamics in stellar interiors, 3D codes are used to simulate specific convective regions. Because convective flows in stars are highly turbulent, with Reynolds numbers (Re) as high as $Re \approx 10^{17}$, significant amounts of computational resources are needed to resolve even the first few orders of magnitude of the energy cascade. The difficulties in attempting to resolve the flow limits the total amount of time of the simulations, usually on the order of a few convective turnover time scales.

In the following sections, the stellar structure equations will be presented along with the assumptions used to derive them (Section 1.3.1). A brief discussion of the dominant energy transport mechanisms are presented in Section 1.3.2. Convective boundary mixing is considered and the exponentially decaying diffusion coefficient model is presented in Section 1.3.3, and the use of 1D and 3D models are discussed in Section 1.3.4.

1.3.1 Stellar Structure Equations

During long periods of a star's evolution, core burning provides support pressure preventing it from contracting. The core burning stages happen on the nuclear time

scale, $\tau_{\rm n}$, and because $\tau_{\rm n}$ is much greater than the other characteristic time scales (Equation 1.6), the star is assumed to be in hydrostatic equilibrium for most of its evolution. The equations that describe the stellar structure and evolution of a star also assume the star is not rotating, has no significant magnetic fields and no binary companions in order to greatly simplify the equations (Kippenhahn & Weigert, 1990). Because the fluid is gravitationally bound and supported by pressure from burning in the core, spherical symmetry is also assumed. The Lagrangian forms of the stellar structure equations as given by Kippenhahn & Weigert (1990) are

$$\frac{\partial r}{\partial m} = \frac{1}{4\pi r^2 \rho} \tag{1.7}$$

$$\frac{\partial P}{\partial m} = -\frac{Gm}{4\pi r^4} \tag{1.8}$$

$$\frac{\partial l}{\partial m} = \epsilon_n - \epsilon_\nu + \epsilon_g \tag{1.9}$$

where r, m, P, l, ρ are the local values for radius, mass, pressure, luminosity and density respectively. In Equation 1.9, the ϵ terms are the energy released per unit time per unit mass, where ϵ_n is the energy generation by specific nuclear reactions, ϵ_ν is the loss due to neutrinos and ϵ_g is the gravitational energy used for expansions or contractions. Equation 1.7 is the conservation of mass equation and provides a transformation between the Eulerian and Lagrangian forms of the stellar structure equations. Equation 1.8 is the momentum equation. In this form, hydrostatic equilibrium has been assumed but during a contraction on the dynamic time scale, τ_{dyn}, this is not valid. During an expansion or contraction, the acceleration term, $-(4\pi r^2)^{-1}\partial^2 r/\partial t^2$, is added to the momentum equation (Kippenhahn & Weigert, 1990). Equation 1.9 is conservation of energy and the terms included in the equation (ϵ_n, ϵ_ν and ϵ_g) represent the dominant energy sinks and sources throughout most of the evolution. The terms in Equation 1.9 depend on structural properties such as temperature, density and radius as well as other variables, coupling them to Equations 1.7 and 1.8.

Equations 1.7 and 1.8 can be derived from the continuity and momentum equations from Navier-Stokes equations if the assumptions above are applied to a spherically symmetric, self gravitating fluid (Kippenhahn & Weigert, 1990; Cox et al., 1968; Oswalt & Barstow, 2013).

The stellar structure equations above describe changes in the star's structure in

response to energy generation in its interior, although they do not contain energy transport. Energy transport within a star is driven by convection and radiation, which have different consequences for the stellar structure.

1.3.2 Convection, Radiation and Conduction

From Cox & Giuli on the subject of the mixing length theory of convection: *"...mixing length theory represents an extreme simplification of the actual physical process of convection. One does not therefore expect quantitative results derived on the basis of this theory to have high accuracy or reliability."* Cox et al. (1968)

The two dominating energy transport mechanisms in stars are radiation and convection. Convection transports energy and material adiabatically within convection zones and is the most efficient of the transport mechanisms whereas conduction is generally negligible.

Radiation can be treated as a diffusive process as the mean free path for a photon during H burning in the stellar interior is on the order of 1cm, much smaller than the radius of the star (Kippenhahn & Weigert, 1990). Because of the large radial temperature gradients and the assumption of spherical symmetry, radiation diffuses radially outward. Similarly, conduction is treated as diffusive although it is negligible for most stellar environments (Kippenhahn & Weigert, 1990). The mean free path of the particles limits the energy transport by conduction. Although, for some gasses the scattering cross section of the particles is small, the high densities in burning regions reduce the mean free path to much less than that for photons. The velocities of the particles are also much less than the speed of light. This means that the diffusion coefficient for conduction is orders of magnitude smaller than that for radiation, and conduction has little effect on the energy transport in stars.

Unlike radiation and conduction, convection can transport material as well as energy, acting to mix the convective material and change the structure of the star. Convection occurs when radiation is unable to transport the energy efficiently enough. In these regions, the temperature builds until a displaced fluid element cannot radiate its energy away fast enough to remain dynamically stable. With the assumptions used to derive the governing equations in Section 1.3.1, a condition for convective stability is given below by the radiative and adiabatic temperature gradients.

The radiative temperature gradient, $\nabla_{\rm rad}$, can be derived using the radiative trans-

port equation in Lagrangian form,

$$\frac{\partial T}{\partial m} = \frac{-3\kappa L}{64a\pi^2 c r^4 T^3} \tag{1.10}$$

where κ is the opacity, c is the speed of light, a is the radiation density constant, r is the radius, m is the mass and T the temperature (Kippenhahn & Weigert, 1990). This equation comes from finding the diffusive flux of radiation in terms of the energy density. Dividing Equation 1.10 by the expression for hydrostatic equilibrium (Equation 1.8) and expressing the equation in terms of natural logarithms produces the radiative temperature gradient.

$$\nabla_{\rm rad} \equiv \left(\frac{d\ln T}{d\ln P}\right)_{\rm rad} = \frac{3\kappa L P}{16\pi c a G m T^4} \tag{1.11}$$

The adiabatic temperature gradient, $\nabla_{\rm ad}$, can be derived from the first law of thermodynamics in terms of T and P, given by

$$dq = c_p dT - \frac{\delta}{\rho} dP \tag{1.12}$$

where c_p is the specific heat and $\delta = (\partial \ln \rho / \partial \ln T)_P$. For an adiabatic process, $ds = dq/T = 0$. The adiabatic form of Equation 1.12 can be solved for dT/dP in terms of natural logarithms. The expression for the adiabatic temperature gradient is given by

$$\nabla_{\rm ad} \equiv \left(\frac{d\ln T}{d\ln P}\right)_s = \frac{P\delta}{T\rho c_p} \tag{1.13}$$

For a displaced fluid element that is able to remain stable, the radiative temperature gradient must be less than the adiabatic temperature gradient. This is the Schwarzschild criterion for convective stability, and for a stable fluid

$$\nabla_{\rm rad} < \nabla_{\rm ad} \tag{1.14}$$

If $\nabla_{\rm rad} \geq \nabla_{\rm ad}$, then radiation is unable to transport the energy efficiently enough and the region is considered to be convective.

Equation 1.14 does not consider contributions from composition in determining convective stability. For H and He convection zones in low and intermediate mass stars, the convective boundaries are dominated by steep entropy gradients rather than mean molecular weight gradients (although mean molecular weight gradients

are still large compared to massive star interiors). In the cores and shells of massive stars during the late time evolution, both the entropy and mean molecular weight gradients are small enough so that entropy is not always dominating the dynamic stability. In these regions, the contribution from mean molecular weight is more significant than during H burning and the convective criterion should reflect this.

The Ledoux criterion for convective stability is similar to the Schwarzschild criterion although it includes the mean molecular weight gradient. The Ledoux criterion for convective stability is given by

$$\nabla_{\rm rad} < \nabla_{\rm ad} + \frac{\phi}{\delta}\nabla_{\mu} \tag{1.15}$$

where $\phi = (\partial \ln \rho / \partial \ln \mu)$, μ is the mean molecular weight and ∇_{μ} is the mean molecular weight gradient (Kippenhahn & Weigert, 1990). The stabilizing term, $(\phi/\delta)\nabla_{\mu}$, is generally positive because $\delta > 0$, $\phi > 0$, and $\nabla_{\mu} \equiv (d \ln \mu / d \ln P)$ and typically increases with pressure. This means that in most cases, $(\phi/\delta)\nabla_{\mu}$ increases convective stability.

Based on one of the stability criteria above, mixing length theory (MLT) is applied to regions that are considered to be convective. Although MLT gives the diffusion coefficient later used in the CBM model, the formulation and sensitivity of MLT itself is not the focus of this thesis. MLT comes with its own free parameter and uncertainties, which are not tested in this work. Below, the equations and assumptions used in MLT will be presented although not discussed in detail.

MLT treats convection as a diffusive process such that the fluid elements are considered to be mixed after traveling a length $l_{\rm MLT} = \alpha_{\rm MLT} H_P$, within the previously determined convection zone. The parameter, $\alpha_{\rm MLT}$ is a free parameter and H_P is the pressure scale height. The theory assumes that a displaced convective element will remain in pressure equilibrium throughout the displacement, but will retain its heat such that over a distance, $l_{\rm MLT}$, it has a temperature difference due to the temperature gradient across the convective region. This means that the flow must remain subsonic as pressure differences will not equilibrate at the sound speed. Hydrostatic equilibrium is also assumed so that the star is in a steady state on the dynamic time scale, $\tau_{\rm dyn}$. This means that the mass flux at a point in the 1D convection zone is zero, as the same amount of mass is *moving* up as is *moving* down. The MLT equations should only be used on a time scale much longer than the convective turnover time scale, $\tau_{\rm conv}$, for the diffusive approximation to be valid. This assumption is certainly not true when

computing the diffusion coefficient in the late stages of evolution of a massive star, as the time step can be on the order of seconds whereas $\tau_{\rm conv}$ in the envelope could be on the order of days.

The five equations of MLT following the derivation of Cox et al. (1968) are

$$F_{\rm rad} = \frac{4acgT^4}{3\kappa P}\nabla_{\rm rad} \tag{1.16}$$

$$F_{\rm conv} = \frac{\rho\bar{v}c_p l_{\rm MLT}T}{2H_P}(\nabla_{\rm rad} - \nabla') \tag{1.17}$$

$$F = F_{\rm rad} + F_{\rm conv} = \frac{4acT^4}{3\kappa\rho H_P}\nabla_{\rm rad} \tag{1.18}$$

$$\bar{v}^2 = \frac{\rho g^2 Q H_P}{8P}(\nabla_{\rm rad} - \nabla') \tag{1.19}$$

$$\frac{\nabla_{\rm rad} - \nabla'}{\nabla' - \nabla_{\rm ad}} = \frac{\Gamma}{1-\eta} \tag{1.20}$$

where $F_{\rm rad}$ is the radiative energy flux, $F_{\rm conv}$ is the convective flux. ∇' in the temperature gradient for the displaced fluid elements and $\nabla_{\rm rad}$ is the radiative temperature gradient and represents the temperature gradient of the surrounding convection zone. $\bar{v}$ is the average speed of the rising fluid element over the distance $\alpha_{\rm MLT}$ (the *diffusive velocity*) and Q can be expressed in terms of ρ, T and μ, defined by

$$-Q \equiv \left(\frac{\partial \ln\rho}{\partial \ln\mu}\right)_{P,T}\left(\frac{\partial \ln\mu}{\partial T}\right)_P + \left(\frac{\partial \ln\rho}{\partial \ln T}\right)_{\mu,P} \tag{1.21}$$

Γ and η are given by the expressions below where η gives the contribution from nuclear burning in the convection zone.

$$\Gamma = \frac{c_p\kappa\rho^2\bar{v}l_{\rm MLT}}{6acT^3} \tag{1.22}$$

$$\eta = \frac{(v - QH_P)\epsilon\kappa\rho^2 l_{\rm MLT}}{16acT^4} \tag{1.23}$$

When there is no nuclear burning in the convection zone, $\epsilon = 0$ and Equation 1.20 becomes

$$\frac{\nabla - \nabla'}{\nabla' - \nabla_{\rm ad}} = \frac{c_p\kappa\rho^2\bar{v}l_{\rm MLT}}{6acT^3} \tag{1.24}$$

The MLT equations give an anisotropic diffusion coefficient based on $\bar{v}$, which mixes the material across the convection zone. If there is local nuclear burning within the convection zone, certain species can be produced which are then diffused. If a particular element is produced quickly with respect to the local diffusive time scale and builds up in a particular region, say somewhere in the centre, then the diffusive approximation is not valid as the element could be advected away from that location, rather than being mixed over a distance l_{MLT}. This shenario implies that the diffusive time scale is less than the convective turnover time scale.

Although the Schwarzschild and Ledoux convection criteria give regions in the star where the fluid is convective, and MLT gives a diffusion coefficient for that convection, the momentum and dynamic interactions of the fluid on the boundary are not taken into account by these methods. Instead diffusion ends abruptly according to the convection criterion used. In order to represent the dynamical mixing that takes place across convective boundaries, a model is needed to represent this CBM.

1.3.3 Convective Boundary Mixing

The mixing of fluid across the boundaries of a convection zone is typically referred to as CBM or overshooting. These general terms come from the use of 1D stellar evolution codes that are unable to capture the fluid dynamics present at these boundaries and must resort to simplified models. CBM refers to an ensemble of fluid instabilities that could be present at the boundary of a convection zone such as, Kelvin-Helmholtz and Rayleigh-Taylor instabilities, gravity waves launched by penetrative convection and boundary layer separation (Herwig et al., 2014) (Figure 1.1). These instabilities act to transport material across convective boundaries so that it can mix with the convecting fluid, affecting the evolution.

If the diffusive approximation of MLT is made for convection, the convection zone is represented by a spatially varying diffusion coefficient that ends abruptly on the convective boundaries. Different CBM models have been used to represent the mixing that would be present across the boundary in many stellar locations (Freytag, Ludwig & Steffen, 1996; Roxburgh, 1989). One CBM model, called instantaneous CBM (or instantaneous overshooting), extends the convective boundary by some fraction of the pressure scale height into the surrounding fluid. Rosvick & VandenBerg (1998) used the instantaneous CBM model by Roxburgh (1989) to better match isochrones to stellar populations by extending the convective core of main sequence stars. The

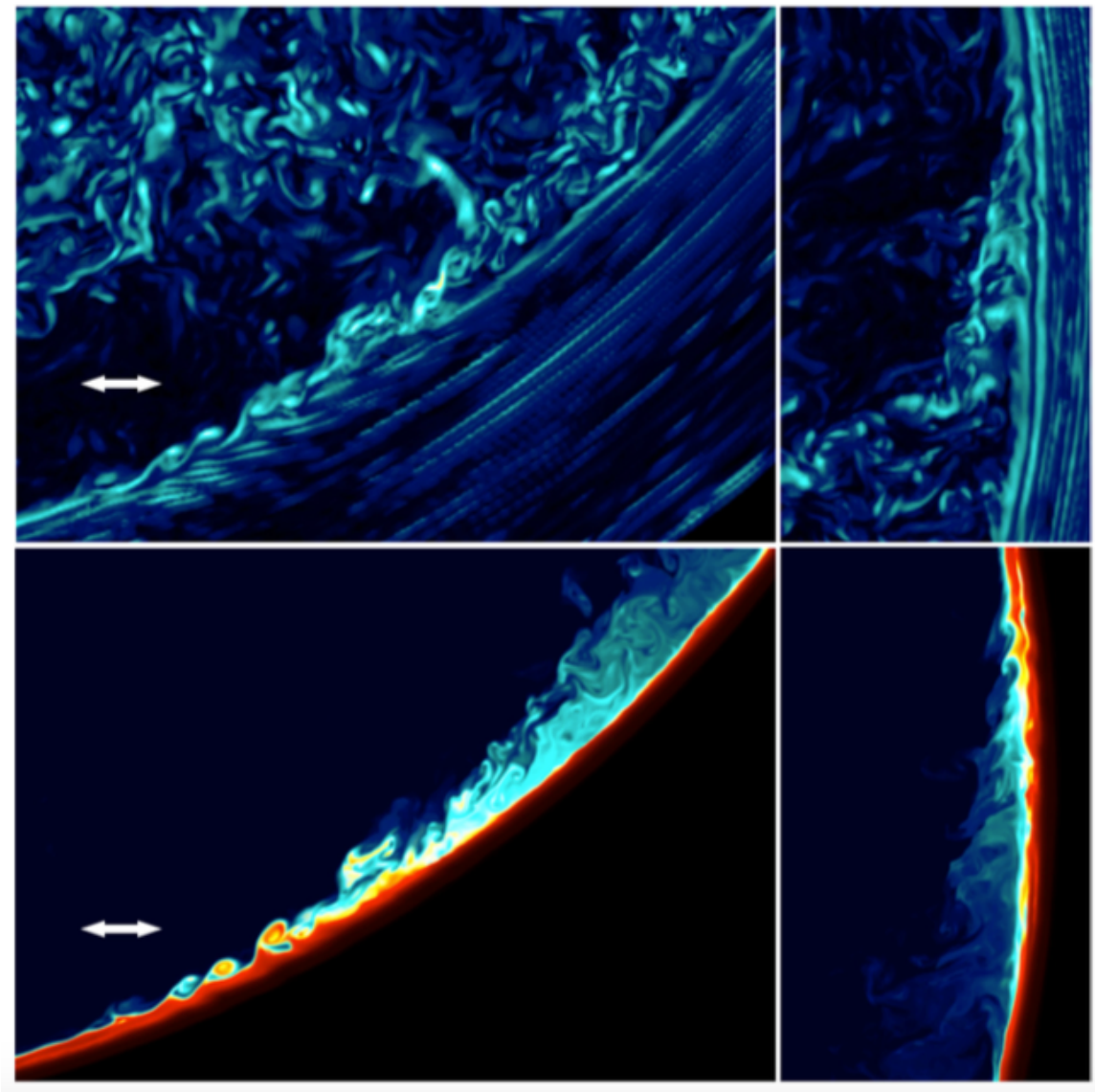

Figure 1.1: Figure taken from Woodward, Herwig & Lin (2015) of Kelvin-Helmholtz instabilities along the boundary between the He-shell flash convection zone and the stable H and He mixture above. The white arrow indicates the 500km initial transition layer between the gasses. The 1D analogy of mixing instabilities such as this constitute the CBM model in Equation 1.25.

exponentially decaying CBM model of Freytag, Ludwig & Steffen (1996) assumes that the diffusion coefficient at the convective boundaries exponentially decays into the stable fluid and allows material to enter the convection zone. The exponentially decaying diffusion coefficient is the focus of this work and is given by

$$D_{\mathrm{CBM}} = D_0 \, e^{\frac{-2z}{f_{\mathrm{CBM}} H_{\mathrm{p}}}} \tag{1.25}$$

where, z is the distance to the convective boundary, and H_{p} and D_0 are the pressure scale height and the diffusion coefficient, which are taken at the convective boundary. The free dimensionless parameter f_{CBM} is used to determine the strength of the mixing.

The inclusion of exponentially decaying CBM during the He-flash in AGB stars changes the evolution both chemically and structurally. Herwig (2000) showed that models calculated with CBM have a larger extent in mass of the pulse driven convection zone followed by a deeper, efficient third dredge-up, among other things. This efficient dredge-up is able to mix ^{12}C and ^{16}O created by the pulse driven convection zone into the envelope, creating a ^{12}C enhancement signature.

Denissenkov et al. (2012) showed that, in novae, exponentially decaying CBM between the boundary of the accreted H rich envelope and the CO white dwarf (WD) better reproduce the enrichment of C, N and O that is observed. With CBM strengths similar to that found in the He shell flash convection zone, the bottom boundary of the thermonuclear runaway convection zone mixes ^{12}C and ^{16}O from the WD into the envelope. This mixing has the effect of producing a fast CO nova with a higher surface luminosity and a higher H burning temperature.

Although direct observation of the convective boundaries found in stellar interiors is not possible, indirect evidence has been given by fitting isochrones to stellar populations (Rosvick & VandenBerg, 1998) and by examining C enhancement in AGB stars (Herwig, 2000). The late stages of massive star evolution however, remain a problem, as no observational evidence is available for the interior during this stage of evolution. As a result, information about the stellar interior must come from simulations.

1.3.4 Modeling and Simulations

The problem of stellar evolution incorporates many branches of physics including fluid dynamics, single and multi-body gravitational interactions, energy transfer, electricity and magnetism, thermodynamics, quantum mechanics and nuclear physics as well

as other things that may only dominate in specific circumstances such as relativistic effects. Any one of these branches of physics provides problems that are not currently solvable either analytically or computationally due to a lack of advancement in theory or computational resources. In order to form a general description of the stellar evolution problem that is able to produce reasonable solutions, governing equations must be formed out of dominant physical mechanisms and solved. Because it is not currently possible to solve even a short list of the mechanisms above on stellar evolutionary time scales, approximations must be made that are specific to the evolutionary phase or physical mechanism of interest.

1D Models

Although the fluid flows present in stars are critical in understanding their evolution, 1D stellar evolution codes approximate convection and other dynamical mixing mechanisms by diffusive processes (Section 1.3.2). The motivation behind this is so that a solution can be approximated on the time scale of the stars life (millions to billions of years). Because the convective turnover time scales, $\tau_{\rm conv}$, of convection zones in some stars can range from days to seconds it is not practical to attempt to simulate the entire evolution of a convection zone, which evolve on the nuclear time scale, $\tau_{\rm n}$, and can last billions of years. Because of this computational limitation, the stellar structure equations (Equation 1.7, 1.8, 1.9) are solved in 1D rather than hopelessly trying to simulate turbulent fluid flows over $\tau_{\rm n}$.

1D stellar evolution codes attempt to approximate the evolution of a star with multiple physical mechanisms under a large number of assumptions. A solution can be obtained from these codes that contains contributions from models for convection, nuclear reactions, dynamic expansion and contraction and rotation, for example. Most importantly, the 1D models used in the codes can be solved over $\tau_{\rm n}$ when implicit time steps are used. This means that 1D simulations can be run over the main sequence as well as the late stages of burning in massive stars. These simulations are able to span the range of time scales found in stellar evolution and give the time evolution of the star as a whole.

Despite the ability to span the range of time scales, the models used in the codes are often far to simplistic to give trustworthy solution. As discussed in Section 1.3.2, MLT gives a diffusive approximation to convection but does not include boundary effects. In an attempt to make the mixing across the boundaries more representative

of physical CBM, the exponentially decaying mixing model given by Equation 1.25 can be used. Although this model is a better representation of convection, it does not come without a price as f_{CBM} is a free parameter that may change for different convections zones throughout the star. Because it is impossible to directly observe any evidence of what its value would be in the interior of a massive star, 3D simulations of the convection zones are necessary in order to constrain this parameter.

3D Models

In 3D, the assumptions used above to derive the stellar structure equations are removed and the governing equations become the Euler equation due to the high Reynolds numbers found in stars ($Re \approx 10^{17}$). Such simulations require large computational domains and time steps that are much smaller than the convective turnover time scale, τ_{conv}. Because $\tau_{\mathrm{conv}} \ll \tau_{\mathrm{nuc}}$, these simulations are only able to capture a short period in the evolution of a particular convective region.

Based on the considerations in Section 1.3.1, there are two general approaches used in simulating stellar environments in 3D. First, an attempt can be made to couple many physical mechanisms to the governing equations in order to approximate the solutions for a particular stellar location. This multi-physics method selects a limited number of mechanisms relevant to the problem, for example, Eulerian fluid dynamics, localized nuclear burning and a large domain including multiple convection zones with different convective turnover time scales (Meakin & Arnett, 2006) as well as turbulence models, which are necessary to compensate for the numerical dissipation of the low resolution fluid flows. Although these simulations attempt to show the interaction between coupled physical mechanisms, the flows remain drastically under-resolved and the reaction networks must be small. The limitation of this method is the large amount of computing power necessary in order to generate meaningful results. The second approach is to reduces a particular problem to one or two dominating physical mechanisms, generally Eulerian fluid flow with coupled energy sources (Jones et al., 2016; Woodward, Herwig & Lin, 2015). This method attempts to understand the effect of one dominating mechanism correctly before adding any additional physics that may or may not change the global fluid flow. Consequently, the computing power that would have gone into calculating the other models can be used to increase the resolution of the simulation in an attempt to better resolve the turbulent fluid flow and convective boundaries.

Despite the limitations of 3D simulations in that they only span a short period of the evolution of the star, the information that they provide in terms of the dynamics of convection and convective boundary mixing is invaluable, as the dynamics of the stellar interior cannot be determined by any other method. The dynamics feed back to the structure and the core structure of a massive star is a contributing factor on whether or not the star will explode as a type II supernova.

1.4 Supernova and Pre-supernova Structure

When massive stars end their lives, they leave behind either a neutron star or black hole remnant. If a neutron star is formed the star would end its life as a type II supernova. Stars that leave behind black hole remnants are thought to produce *failed* supernovae, a long, low luminosity transient ($L \approx 10^{39}\mathrm{erg s}^{-1}$ for about 1yr (Lovegrove & Woosley, 2013)). Connections between the presupernova structure in the core and the success or failure of supernova explosion has been studied by O'Connor & Ott (2011) and Ertl et al. (2016). O'Connor & Ott (2011) found that there is a connection between the exploitability of massive stars and a core density like parameter of the presupernova structure. This parameter is called the *compactness* and it is defined as

$$\xi_M = \left.\frac{M_{\mathrm{bary}}/\mathrm{M}_\odot}{R(M_{\mathrm{bary}})/1000\mathrm{km}}\right|_{t=t_{\mathrm{bounce}}} \tag{1.26}$$

where M_{bary} is the baryonic mass and $R(M_{\mathrm{bary}})$ is the radius in which a mass of M_{bary} is enclosed. The mass is generally set to $M_{\mathrm{bary}} = 2.5\mathrm{M}_\odot$ at the time of the bounce, t_{bounce} (O'Connor & Ott, 2011). Sukhbold & Woosley (2014) studied the sensitivity of $\xi_{2.5}$ to ZAMS mass and found the relation to be non-linear. A plot of $\xi_{2.5}$ with respect to ZAMS mass shows so called *islands of non-explodability* where $\xi_{2.5}$ increases to higher values (Figure 1.2), meaning that some stars in a given ZAMS mass interval will be harder to explode than their neighbours.

1.5 Goals of this work

The goal of the work presented in this thesis is to investigate the CBM during selected evolutionary stages in massive star simulations. To date, the sensitivity of the structure of massive star cores with respect to CBM has not been studied in detail despite

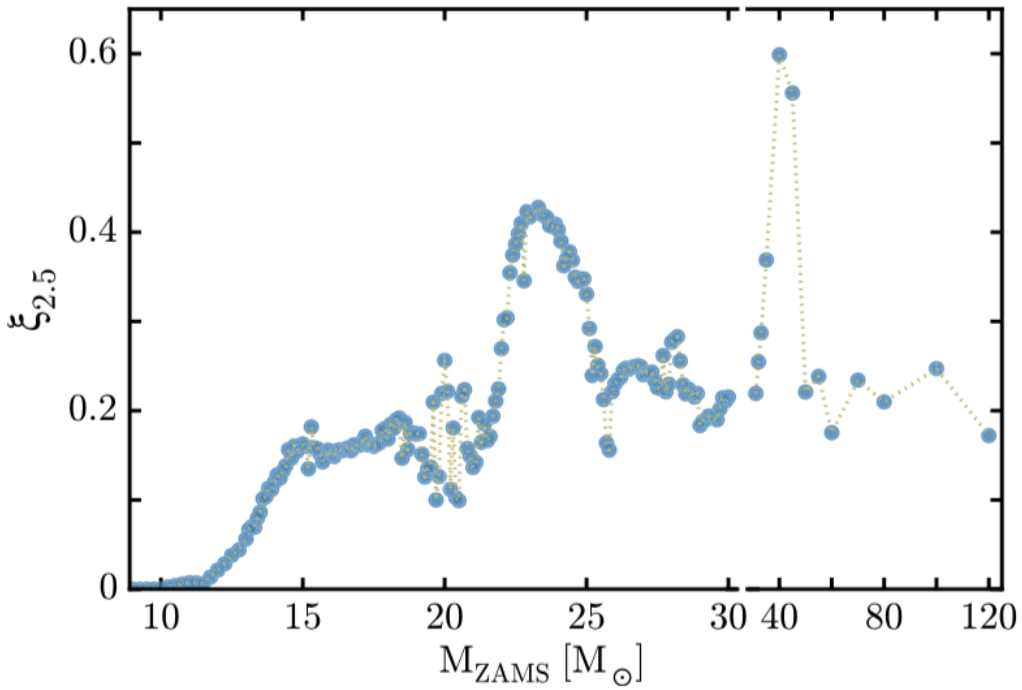

Figure 1.2: Compactness vs ZAMS mass from Sukhbold et al. (2016). The plot shows the islands of non-explodability around $M_{\mathrm{ZAMS}} \approx 23\mathrm{M}_\odot$ and $M_{\mathrm{ZAMS}} \approx 40\mathrm{M}_\odot$. Larger values of $\xi_{2.5}$ are simulations with higher core density and will be harder to explode than lower values.

the close proximity of convection zones found there. Chapter 2 focuses on determining the diffusion coefficient and f_{CBM} model parameters that would be needed in a 1D stellar evolution code to reproduce the results from the spherically-averaged mixing in the 3D simulation. A method is presented in which the diffusion coefficient can be found from radially averaged composition profiles from a 3D O-shell simulation. The goal of Chapter 3 is to investigate the structural variation in the post He core burning of a $25\mathrm{M}_\odot$ stellar model at solar metallicity with respect to changes in the CBM parameter, f_{CBM}. A series of 1D simulations was run with different values of f_{CBM} and the evolutionary and presupernova structure was compared. Although the work in Chapter 2 suggests a value of f_{CBM} for the O-shell in a $25\mathrm{M}_\odot$ simulation, the goal of Chapter 3 is not to determine the f_{CBM} values used in 1D simulations. The structural variations of the 1D model with respect to the f_{CBM} are what is important, as these values are, for the most part, unknown for many convection zones and have a significant impact on the evolution. The work presented here acts to motivate the study of convection and CBM in the advanced evolutionary stages of massive stars

by linking the CBM models to the explodablility of simulations and further galactic chemical enhancement.

Chapter 2

Mixing Models from 3D Hydro Simulations

This chapter outlines the paper *Idealised hydrodynamic simulations of turbulent oxygen-burning shell convection in* 4π *geometry* written by S. Jones, R. Andrassy, S. Sandalski, P. Woodward, F. Herwig (Jones et al., 2016) and myself. Section 2.1 gives a brief summary of the work presented in the paper completed by the authors above. Jones and I primarily completed Section 2.2, which focuses on determining the diffusion coefficient and the value of $f_{\rm CBM}$ from the 3D hydrodynamic simulation. Because 1D stellar evolution models do not accurately represent convective mixing, the 3D simulations presented below act to better capture the hydrodynamics of the first convective O-shell. The value for $f_{\rm CBM}$ found from the 3D simulation acts to motivate the study of CBM on the structure and evolution found in 1D models, presented in Chapter 3.

2.1 Paper Summary

The paper by Jones et al. (2016) simulates the first O-shell of a $25 M_{\odot}$ 1D MESA simulations in 3D, using the PPMstar hydrodynamic code. The setup for the PPMstar simulation was taken from the MESA model with some adjustments and a series of seven simulations were run at 768^3 and 1536^3 resolution. From these simulations, the entrainment rate at the upper convective boundary was studied along with changes to the luminosity and how to map the large scale 3D results back into 1D models.

For the O shell simulations, a gamma law equation of state is used for a two

fluid stratification. In the MESA simulation, the peak O burning luminosity is found near the bottom of the convection zone. To model this, convection is driven by a constant luminosity source implemented by a spherically symmetric distribution extracted from the 1D stellar evolution simulation. The luminosity profile includes the relevant nuclear reactions present at the bottom of the convection zone as well as the neutrino losses. Only the convecting region of the O-shell and the overlaying radiative region separating the convective C and O shells are simulated.

A difference in the entrainment rate, $\dot{M}$, between the 768^3 (D1) and 1536^3 (D2) simulations was found. The two simulations had the same luminosity of $L = 1.18 \times 10^{11}\mathrm{L}_\odot$ and only differed by resolution. The entrainment rate of the D1 simulation was found to be $1.15 \times 10^{-6}\mathrm{M}_\odot\mathrm{s}^{-1}$ were as the D2 simulations gave an $\dot{M}$ value of $1.33 \times 10^{-6}\mathrm{M}_\odot\mathrm{s}^{-1}$. The two simulations have a difference in $\dot{M}$ of 16% and because of this relatively small difference, a heating series was performed at 768^3 where the luminosity was artificially increased and the entrainment rate determined.

The heating series consisted of six simulations with increasing luminosity from $L = 1.18 \times 10^{11}\mathrm{L}_\odot$ to $L = 5.91 \times 10^{12}\mathrm{L}_\odot$ (See Jones et al. (2016), Table 1 for more information). Andressy found that the entranment scales with the driving luminosity as

$$\dot{M} = \frac{2}{5}\alpha_i \frac{\mu_1\mu_2}{\mu_2 - \mu_1}\frac{L}{\mathrm{R}^* T} = 29.0\alpha_i \frac{L}{\mathrm{R}^* T} \tag{2.1}$$

where $\mu_2 > \mu_1$ and is the mean molecular weight of the fluid, α_i is a dimensionless parameter and R^* is the gas constant. For the O-shell simulations, $\mu_1 = 1.802$ and $\mu_2 = 1.848$.

2.2 1D Diffusion Coefficient from the 1536^3 3D Simulation

In 1D stellar evolution models, convection is treated as a diffusive process. One of the main goals of performing 3D hydrodynamic simulations of specific convective regions is to inform those 1D models. The work outlined below and completed with the help of Jones was motivated by the following question: *what diffusion coefficient profile would have been needed in 1D in order to reproduce the spherically-averaged mixing in the 3D simulations?* In an attempt to answer this question, the diffusion equation was discretized and solved numerically for the specially dependent diffusion

coefficient. The discretized diffusion equation is given by

$$x_m(X_k^n - X_k^{n+1}) = \frac{X_k^{n+1} - X_{k-1}^{n+1}}{x_l}\Delta t\ D_k + \frac{X_k^{n+1} - X_{k+1}^{n+1}}{x_r}\Delta t\ D_{k+1}\ , \tag{2.2}$$

where

$$\begin{aligned} x_r &= r_{k+1} - r_k\ , \\ x_l &= r_k - r_{k-1}\ , \\ x_m &= \frac{1}{2}(r_{k+1} - r_{k-1})\ . \end{aligned}$$

where r and t are the radius and time, X is the mass fraction of the entraining fluid and D is the spatially varying diffusion coefficient. The space and time discretization are given by the indices k and n respectively and Δt is the time difference between the time steps. For the spherically averaged data on a mesh with spacing Δx presented in Jones et al. (2016), $x_r = x_l = x_m = \Delta x$.

Jones wrote a code to calculate the diffusion coefficient given two composition profiles from the PPMstar simulations separated by a time Δt. The initial and final composition profiles, taken at 620s and 1140s, were averaged over 400s ($\approx \tau_{conv}$) in an attempt to decrease the fluctuations in the centre of the convection zone. At early times in the simulation (< 300s), these fluctuations are caused by the highly turbulent convective mixing in this region. As material from the convectively stable layer above is entrained into the convection zone the fractional volume increases quicker at the top than at the bottom creating a fractional volume gradient (Figure 2.1).

The diffusion coefficient calculated from the 3D data is plotted in Figure 2.2 (brown line) and compares the diffusion coefficient profiles from other MLT methods. The fluctuations in the fractional volume profiles appear as noise in the diffusion coefficient profile around 5Mm $\lesssim r \lesssim$ 6Mm. In this region the gradient of the fractional volume profiles approaches zero with some residual fluctuations and the method for calculating the diffusion coefficient becomes numerically unstable. A physical interpretation of this is that the final composition profile is flat so there is no unique diffusion coefficient that would reproduce this. Many diffusion coefficients are possible and the solution here are more representative of a minimum value. Near the boundaries of the convection zone the gradient of the composition is large and the diffusion coefficient becomes smooth, dropping off exponentially. Figure 2.2 includes

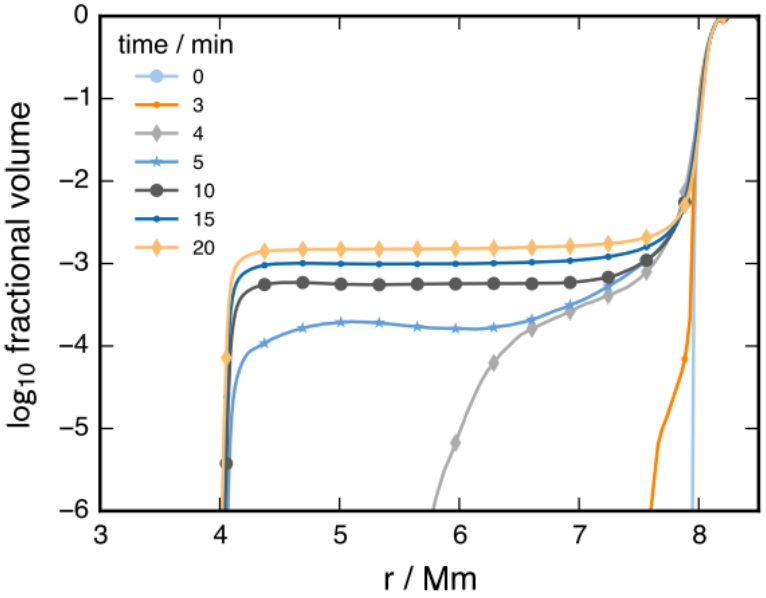

Figure 2.1: Figure from Jones et al. (2016). The figure was created by Jones and is the fractional volume vs radius for the PPMstar O-shell simulation. The profiles show the fractional volume of the overlying fluid increasing in the convection zone in time. The averaged profiles used in the diffusion coefficient calculation are not shown. The initial profile taken at $t_1 = 620\text{s} = 10.3\text{min}$ and final profile at $t_2 = 1140\text{s} = 19\text{min}$ were averaged over a 400s interval centred on those points. Considerable fluctuations in the composition were found at times less that 5min for low values of the log of fractional volume (not shown in figure).

other diffusion coefficients calculated by Jones. The grey dashed line is the diffusion coefficient used by MLT in the MESA simulation which is larger than the PPMstar values at the boundaries and smaller in the centre of the convection zone. The blue dash-dotted line is the diffusion coefficient calculated in the same form as in MLT as $D = v\alpha H_P/3$ where the velocity has been taken as the radially averaged velocity from the PPMstar simulation. In this form of the diffusion coefficient, α is a free parameter and H_P is the pressure scale height. In looking at the models from this study and Herwig et al. (2006), Jones, Andrassy and Herwig found that the luminosity scales with velocity in 3D and that MLT velocities are too low by a factor of $\approx 2-3$.

The diffusion coefficient for the upper convective boundary of the O-shell is plotted in Figure 2.3 along with the composition profiles (brown and grey) and the convective boundary region (between the two dotted lines). Jones gives the blue asterisk line as the recommended diffusion coefficient for MLT and is given by $D_{\text{RCMD}} = v_{\text{MLT}} \times \min(\alpha H_P, |r - r_{SC}|)$ where r_{SC} is the Schwarzschild boundary

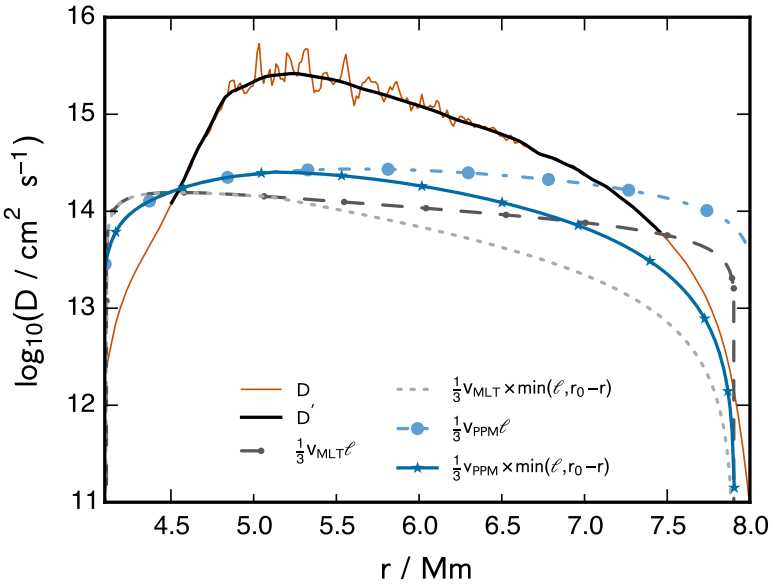

Figure 2.2: Figure taken from Jones et al. (2016). The figure was created by Jones and is a plot of the diffusion coefficient profiles from the spherically averaged composition and velocity profiles of the PPMstar O-shell simulation. The dark orange line is the diffusion coefficient calculated using the inverse diffusion coefficient method (Section 2.2). The black line is a cubic spline fit to a piece-wise linear downsampled of the noisy region between 5Mm $\lesssim r \lesssim$ 6Mm. Here, $l = \alpha H_P$ where α is a free parameter in MLT and H_P is the pressure scale hight.

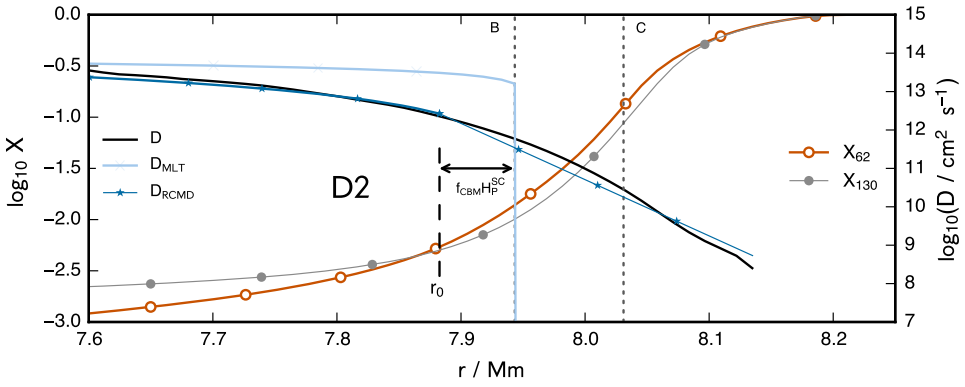

Figure 2.3: Figure taken from Jones et al. (2016). The region considered to be the convective boundary is found between the two dotted vertical dotted lines. The black solid line is the diffusion coefficient calculated by the method in Section 2.2. The light blue line in the MLT diffusion coefficient. D_{RCMD} is the recommended diffusion coefficient. The brown and grey lines are the composition profiles used in the diffusion coefficient calculation.

and r is the radius. Fitting the exponentially decaying CBM model to the diffusion coefficient at a distance of $f_{\rm CBM}H_P$ from r_{SC} gives a value of $f_{\rm CBM} = 0.03$.

The $f_{\rm CBM}$ value found above is relatively high compared to that found by Herwig (2000) of $f_{\rm CBM} = 0.016$ for the AGB He-flash convection zone and the value determined by Denissenkov et al. (2012) of $f_{\rm CBM} = 0.004$. Although these $f_{\rm CBM}$ values are for different stellar sites and were not determined in the same manner as above, in 1D studies involving the late stage evolution of massive stars, the $f_{\rm CBM}$ values are generally taken to be small. An $f_{\rm CBM} = 0.002$ is used in Jones et al. (2015) and the 1D simulation used to initialize the work presented in this chapter. The range of values given above for $f_{\rm CBM}$ naturally lead to the question of how does a stellar model change with changes to the CBM parameter, $f_{\rm CBM}$.

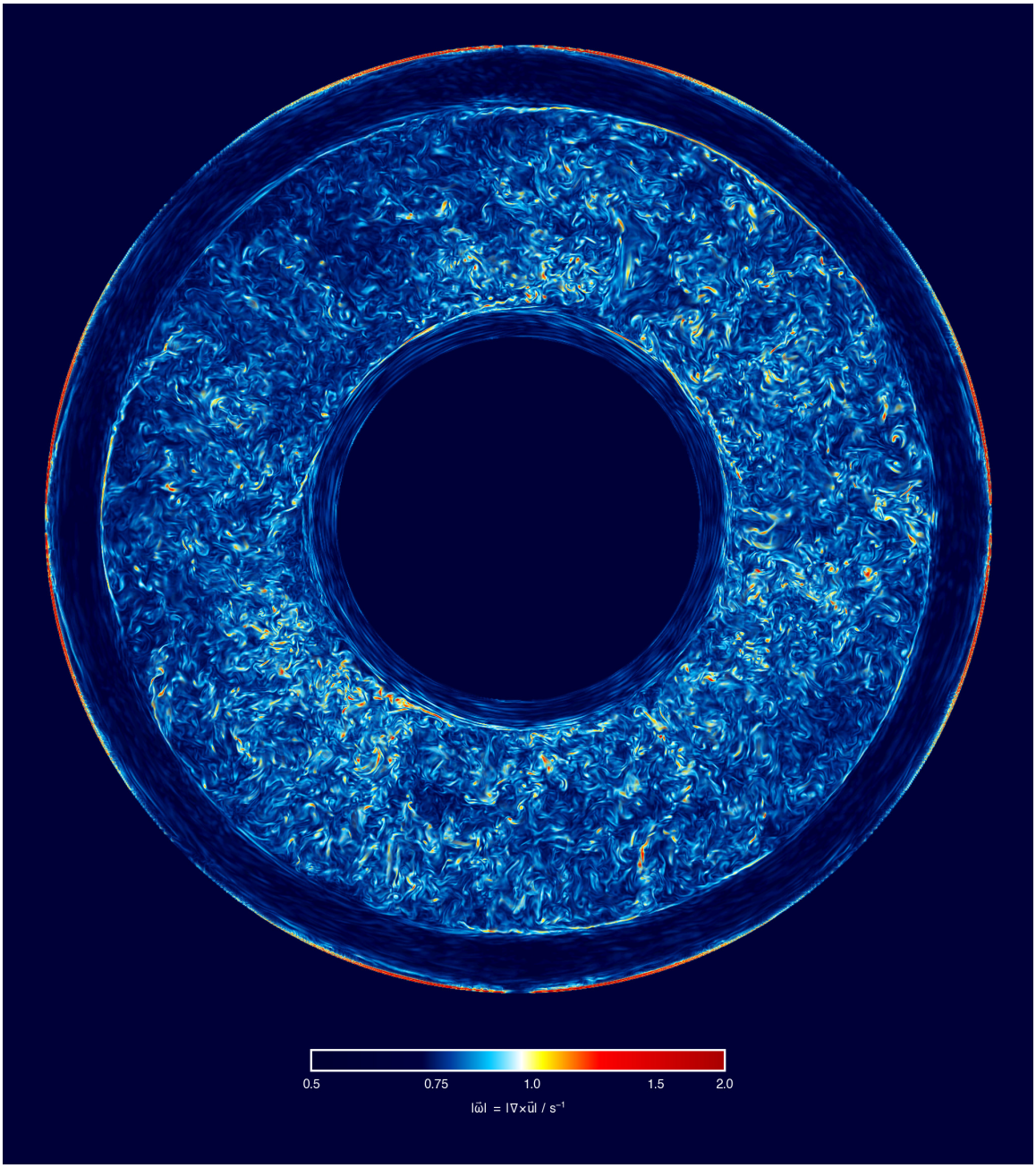

Figure 2.4: Figure taken from Jones et al. (2016) of the vorticity in the O-shell simulation at 1536^3 spatial resolution. The centre of the image shows the inert core under the O-shell as the region of no vorticity. The convection zone is shown by the turbulent region surrounding the core. The stable upper fluid is overlying the convection zone.

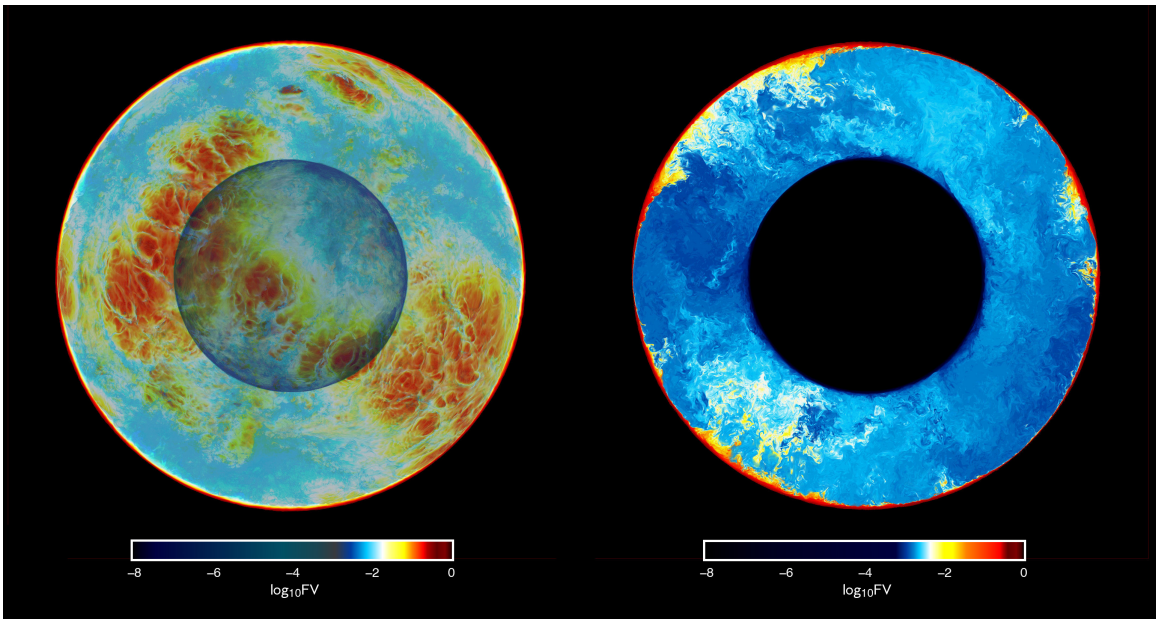

Figure 2.5: Figure taken from Jones et al. (2016) of the log fractional volume of the entrained fluid in the 1536^3 PPMstar O-shell simulation. The image on the left is a 3D rendering of the entrained material through the back hemisphere. The image shows the semi transparent core boundary in the centre. The image on the right shows the a slice of the same simulation. The transport of material by convection is apparent by the asymmetric down drafts and updrafts of material.

Chapter 3

Convective boundary mixing in a post-He core massive star model

This chapter contains an extended version of the work presented in *Convective boundary mixing in a post-He core massive star model* written by A. Davis, S. Jones, and F. Herwig. At the time of writing this thesis, the paper is in preparation for submission.

3.1 Introduction

Convection in stellar interiors is highly turbulent with Reynolds numbers, Re $\approx 10^{16}$. At the boundaries of convective regions, fluid instabilities act to mix material across these boundaries. The material that is *entrained* into the convection zone can then be mixed and transported across the convection zone by the large-scale flows found there. This convective boundary mixing (CBM) has consequences for the following evolution of the star. CBM in the He-shell flash convection zone in asymptotic giant branch (AGB) stars can lead to the production of carbon stars (Herwig, 2000). The CBM found in the late-time evolution of the O-shell in massive stars can potentially lead to shell mergers with the overlying C-shell (Jones et al. (2016); Meakin & Arnett (2006)). The inclusion of CBM in the thermonuclear runaway convective boundary of an accreting CO white dwarf (WD) can mix ^{12}C and ^{16}O into the envelope, and increase the H burning temperature (Denissenkov et al., 2012).

A massive star is a star with a zero age main sequence (ZAMS) mass $\gtrsim 8M_{\odot}$, and can end its life as type II supernova. For a star with a ZAMS mass of about $25M_{\odot}$, when the He-burning core has been depleted, a core of He ash in the form of

C and O is left behind. During the remainder of the evolution, the star will build up concentric shells that burn He, C, Ne, O and Si, around an Fe-core. These shells are tightly packed in radius and can exhibit strong convection (Rauscher et al., 2002; Meakin & Arnett, 2006; Jones et al., 2016). Nearly adiabatic convection can be present at the base of a shell due to large temperatures gradients. These convection zones are generally separated by radiative region composed of the ash from the shell burning above. Mixing mechanisms such as shearing, penetrative convection, gravity waves and boundary layer separation, collectively referred to as CBM, act to mix surrounding material into the convection zone. Generally, material mixed from above by the CBM mechanisms can transport fuel down to depths in the convection zone where it can burn. Alternatively, ash mixed in from below can be transported further out from the stellar interior were it could be ejected by the supernova explosion (Fryer et al., 2012). The core burning stages of a massive stars are sensitive to the CO-core mass left behind from the previous He burning stage, influencing the timing, extent and luminosity, amongst other evolutionary characteristics (see, e.g., Sukhbold & Woosley (2014)).

The work outlined in this chapter presents the differences found in the stellar structure of 1D stellar evolution models of massive stars with respect to increasing CBM strength in post He-core evolution. The exponentially decaying form of the diffusion coefficient proposed by Freytag, Ludwig & Steffen (1996) is used as a model for CBM. The structure of each core burning evolutionary phase, simulated with different CBM values, is investigated in terms of core boundaries and convection zones, and the resulting presupernova structure is studied. Section 3.2 outlines the model, model parameters and simulations as well as comparing the main sequence and He-core burning to previous work. Section 3.3 describes the results including evolutionary compactness diagrams and the final abundances in terms of production factors. These results are summarized in Section 3.4 and discussed in Section 3.5.

CBM has a significant impact on the structure of the metal burning cores of the models. Enhanced CBM implemented during core C, Ne and O burning change the structure drastically due to the interacting of the C and Ne shells. These structural changes cause non-monotonic variation in the presupernova compactness, determining if the star will explode or not. Shell mergers and dredge-ups of Ne ash into the C shell change the abundances in the C shell and can possibly be ejected by the potential supernova explosion, provided the fallback radius in located within the C shell or lower, and the simulation has enough time left in its evolution to mix material passed

the fallback radius.

3.2 Methods

3.2.1 The MESA model

The MESA model template taken from Jones et al. (2015) was modified to run with MESA revision 7109. The model uses a ZAMS mass of $25M_{\odot}$ and has a metallicity of $Z = 0.02$ with relative abundances of the metals after Grevesse & Noels (1993). The physics was changed to adopt the Ledoux criterion for convection and account for semiconvective mixing (Section 1.3.2). It also uses a smaller nuclear reaction network (Table 3.1). The Ledoux criterion for the position of the convective boundaries was used to account for shells of varying composition and entropy that develop during the late time evolution of massive stars (Sukhbold & Woosley, 2014; Woosley, Heger & Weaver, 2002). The Ledoux criterion and semiconvection can change the Fe-core mass by decreasing the CO-core mass and increasing the C/O ratio after He burning, as well as inhibiting electron capture reactions present during Si-shell burning (Woosley & Weaver, 1988; Woosley, Heger & Weaver, 2002; Jones et al., 2015). The efficiency parameter of semiconvection is taken to be $\alpha_{semi} = 0.1$ (Langer, Fricke & Sugimoto, 1983), and is considered to be fast semiconvection (Woosley & Heger, 2007). The model uses a custom reaction network that changed for each burning stage (Table 3.1). A larger network is used for core Ne and O burning than main sequence and He-core burning to more accurately capture the nuclear reactions involving heavier species found there. For core Si burning, the network is reduced to 21 species, as MESA revision 7109 cannot accurately reproduce the nuclear burning that is present at that point in the evolution.

CBM is taken into account by the exponentially decaying mixing model from Equation 1.25. $f_{\rm CBM}$ is a free parameter of the model and the parameter of interest for this study and will be applied to the metal burning convection zones. A metal burning convection zone is a convection zone where the peak energy generation does not come from H or He burning.

3.2.2 Set of CBM simulations

In MESA revision 7109, the CBM parameter for metal burning convection zones is applied to all metal burning convection zones. This means that, for example, a specific $f_{\rm CBM}$ value will be applied to a C-shell as well as the O-core evolving simultaneously. Currently there is no convincing model for how CBM should depend on the specific reactions dominating the energy production at the bottom of a convection zone. Additionally, if individual $f_{\rm CBM}$ values could be applied to each metal burning convection zone and a simulation was calculated for each core burning stage, then the number of simulations required is the number of $f_{\rm CBM}$ values tested, to the fourth power (for C, Ne, O and Si-core burning stages). To reduce the complexity of the CBM study, the code was not modified and the stellar structure was determined for the metal burning $f_{\rm CBM}$ values presented below (Table 3.2).

Initial tests of the MESA model showed nonlinear cumulative effects on the structure with respect to $f_{\rm CBM}$ values throughout the evolution. The tests showed that structural changes during the previous burning phase greatly affected the preceding one. In order to investigate the effects of different CBM strengths on the metal burning convection zones that develop inside of the massive star simulations, the MESA simulation was run several times at specific evolutionary stages with different values of $f_{\rm CBM}$ (Figure 3.1). Although potentially unphysical, this method studies the sensitivity of the MESA simulations stellar structure with respect to CBM strength, at different times in the later stages of evolution.

The MESA model was run to collapse with fixed CBM values for the metal burning convection zones of $f_{\rm CBM} = 0.002$. From here on, this simulation is referred to as the `TEMPLATE` simulation. This `TEMPLATE` simulation was then used as the starting point for the other simulations in the CBM study (Figure 3.1). At the beginning of C, Ne and Si-core burning, a snapshot of the `TEMPLATE` simulation was taken and the value of $f_{\rm CBM}$ was then varied over a range of values, (0.012, 0.022, 0.032) (Figure 3.2, Table 3.2). This produced nine simulations that branched from the `TEMPLATE` (`C1`, `C2`, `C3`, `ONe1`, `ONe2`, `ONe3`, `Si1`, `Si2` and `Si3`), where each simulation is indexed by the core burning stage followed by the increase in strength of the CBM (Table 3.2). For example, `ONe3` branches from the `TEMPLATE` at the beginning of Ne-core burning with $f_{\rm CBM} = 0.032$. The conditions used to determine when to branch from the `TEMPLATE` simulation are given by the central temperature. The `C` set of simulations branch from the `TEMPLATE` when $logT_{\rm C} = 8.88$, the `ONe` set branch at $logT_{\rm C} = 9.15$

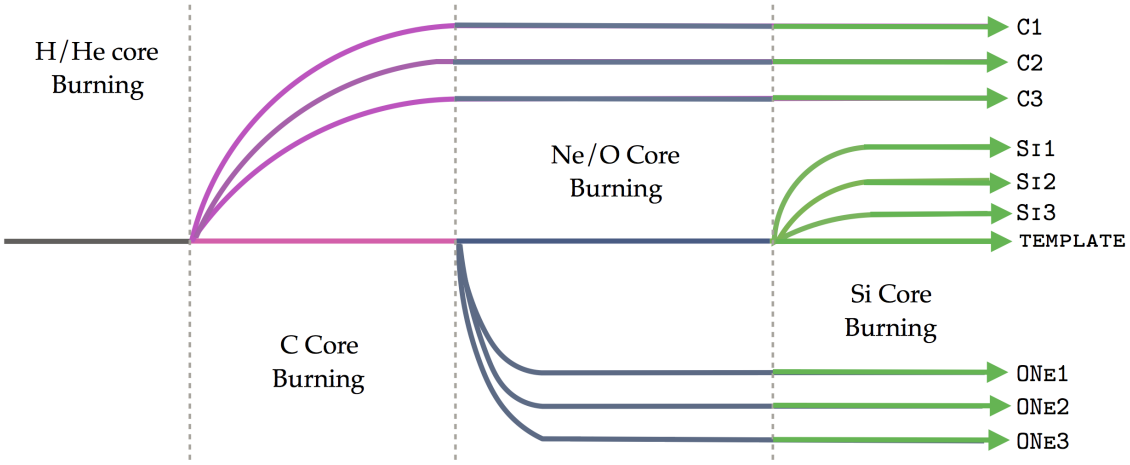

Figure 3.1: A diagram of the simulations computed for this study. Each solid line represents a simulation. The colours, separated by dashed lines, represent different core burning stages and the label at the end of each line is the run index (Table 3.2). The `TEMPLATE` simulation was run to collapse with minimal $f_{\rm CBM}$ and all subsequent runs use a radial profile of the structure from the template as a staring position.

and the `Si` set branch at $logT_{\rm C} = 9.39$.

The values of $f_{\rm CBM}$ were chosen to span CBM strengths ranging from the lowest value such that the simulation would converge $f_{\rm CBM} = 0.002$ to a large value of $f_{\rm CBM} = 0.032$. Jones et al. (2016) found $f_{\rm CBM} = 0.03$ for the upper boundary of an O-shell in the $25 M_{\odot}$ 3D hydrodynamic simulation in Chapter 2, although the implementation presented here is for the upper and lower convective boundaries. Additionally, in Jones et al. (2016), CBM was decayed from an amount, $f_{\rm CBM} H_P$ inside of the Schwarzschild convective boundary. This parameter is generally denoted by f_0 and represents a linear shift of the CBM model into the convection zone. In this study the value of $f_0 = 0.002$ for all simulations. This value was fixed so that only the value of $f_{\rm CBM}$ was tested.

Some CBM was needed in the `TEMPLATE` simulation in order to smooth the numerical discontinuities that arise at the sharp convective boundaries. The minimal values of $f_{\rm CBM} = 0.002$ and $f_0 = 0.002$ used in the `TEMPLATE` are the smallest CBM values that will allow the code to converge without the use of smoothing modules that can be turned on in the code.

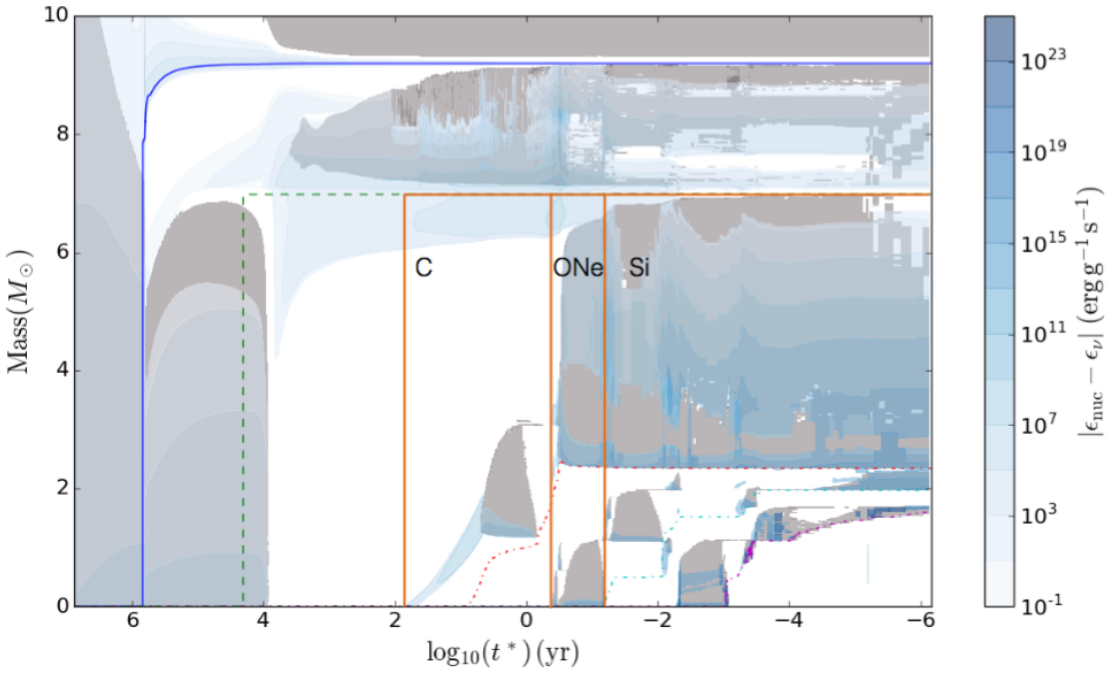

Figure 3.2: The regions of the MESA simulation under investigation. The Kippenhahn diagram is taken from the `TEMPLATE` simulation. Grey areas represent regions that are convectively unstable and the blue contours are regions of positive energy generation where ϵ_ν is the specific energy loss rate due to neutrino production. The x-axis is given in log of the time until the star collapses. The solid blue line marks the CO-core ($X_{\rm H} < 10^{-2}$), the dashed green line in the CO-core boundary ($X_{^4{\rm He}} < 10^{-2}$), the dash-dotted red line in the ONe-core ($X_{^{12}{\rm C}} < 10^{-2}$), the dash-dotted light blue line is the Si-core ($X_{^{16}{\rm O}} < 10^{-2}$) and the dash-dotted magenta line is the Fe-core ($X_{^{28}{\rm Si}} < 10^{-2}$). The orange lines mark the region of interest for this study where the vertical orange lines mark the beginning of core burning stages. These vertical orange lines mark the points where the CBM is increased for each of the respective run sets (`C`, `ONe`, `Si`).

Table 3.1: Networks used in MESA.

Networks used in MESA. The columns are the atomic number of the elements on the left most column.

	H, He, C	Ne, O	Si
H	1, 2	1, 2	1
He	3, 4	3, 4	3, 4
Li	7	7	-
Be	7	7	-
B	8	8	-
C	12, 13	12, 13	12
N	13-15	13-15	14
O	15-18	15-18	16
F	17-20	17-20	-
Ne	18-22	18-22	20
Na	20-23	20-23	-
Mg	22-26	22-26	24
Al	24-27	24-27	-
Si	27-28	27-31	28
P	-	30-33	-
S	-	31-35	32
Cl	-	35, 37	-
Ar	-	36-38	36
K	-	39	-
Ca	-	40, 42	40
Sc	-	45	-
Ti	-	46	44
Cr	-	-	56
Fe	56	56	52-56
Ni	-	-	56

Table 3.2: MESA Simulation Parameters

Selected values for each simulation. The columns labeled $f_{\rm CBM}$, followed by a core burning stage, are the CBM parameters, which are dimensionless, implemented during that burning stage. The column labeled $M_{\rm CO}$ is the CO-core mass at the end of He-core burning and is the same for each simulation, as they branch from the TEMPLATE later in the evolution (Figure 3.1, 3.2). $M_{\rm ONe}$ is the mass of the ONe-core when the simulations begin to burn Ne in the core (Section 3.2.2). $M_{\rm Si}$ is the mass of the Si-core when convection stops there. $M_{\rm Fe}$ is the mass of the Fe-core at $log(t^*) = -6$. The presupernova compactness, $\xi_{2.5}$, taken at $log(t^*) = -6$, the values do not change much past this point.

Name	$f_{\rm CBM}$(H, He)	$f_{\rm CBM}$(C)	$f_{\rm CBM}$(Ne, O)	$f_{\rm CBM}$(Si)	$M_{\rm CO}[{\rm M}_\odot]$	$M_{\rm ONe}[{\rm M}_\odot]$	$M_{\rm Si}[{\rm M}_\odot]$	$M_{\rm Fe}[{\rm M}_\odot]$	$\xi_{2.5}$
TEMPLATE	0.002	0.002	0.002	0.002	6.93	1.77	1.51	1.59	0.272
C1	0.002	0.012	0.012	0.012	-	1.74	1.41	1.47	0.172
C2	0.002	0.022	0.022	0.022	-	1.77	1.60	1.56	0.304
C3	0.002	0.032	0.032	0.032	-	1.86	1.82	1.60	0.354
ONe1	0.002	0.002	0.012	0.012	-	-	1.46	1.46	0.159
ONe2	0.002	0.002	0.022	0.022	-	-	1.61	1.54	0.249
ONe3	0.002	0.002	0.032	0.032	-	-	1.68	1.52	0.152
Si1	0.002	0.002	0.002	0.012	-	-	-	1.62	0.217
Si2	0.002	0.002	0.002	0.022	-	-	-	1.54	0.162
Si3	0.002	0.002	0.002	0.032	-	-	-	1.43	0.120

3.2.3 H and He-core burning comparison

Because the MESA model used here is a modified version of that used by Jones et al. (2015), the CO-core mass, the convective core lifetimes and the $^{12}C/^{16}O$ ratio in the core at the end of core He burning will be compared to those in Jones et al. (2015). Woosley & Weaver (1988) studied the effects of CBM, semiconvection and Coulomb corrections on massive star models and showed that the He-core evolution is sensitive to the mixing models used. During He-core burning in some massive star models, if small amounts of semiconvection and CBM are used, a numerical instability develops where the He-core bifurcates due to a composition barrier (Woosley, Heger & Weaver, 2002). This region would normally be convective by the Schwarzschild criterion. The effect of this bifurcation decreases the CO-core mass after He-core burning and subsequently changes the Fe-core mass. The effects of using the Ludoux criterion and semi-convection are investigated below by comparing the model used here to the result from Jones et al. (2015), as the MESA model used there was modified for this study.

The CO-core mass given by the `TEMPLATE` simulation gives a percent difference of 6.13% from the mean of the three values given by Jones et al. (2015) of $6.53M_{\odot}$, and 1.61% from the MESA simulation by Jones et al. (2015). The CO-core mass found in the `TEMPLATE` simulation is $6.93M_{\odot}$ using the Ledoux criterion and semiconvection. From Jones et al. (2015), the MESA model using the Schwarzschild convection criterion obtains a value of $6.82M_{\odot}$ and is the highest among the values found. The other two CO-core masses are $6.48M_{\odot}$ and $6.28M_{\odot}$ from the GENEC and KEPLER codes respectively.

The $^{12}C/\ ^{16}O$ ratio found in the core of the `TEMPLATE` simulation is 0.334. Jones et al. (2015) gives two values of the $^{12}C/\ ^{16}O$ ratio at the end of core He burning, one calculated from the network used in the stellar evolution code and one from a post processing network. The values from the network used in the stellar evolution code will be used here. The $^{12}C/\ ^{16}O$ ratio at the end of core He burning in the MESA simulation given by Jones et al. (2015) is 0.360. The values given by the GENEC and KEPLER codes are 0.372 and 0.235 respectively. The $^{12}C/\ ^{16}O$ ratio found in the `TEMPLATE` simulation has a percent difference of 7.22% from the MESA simulation given by Jones et al. (2015).

The main sequence lifetime of the `TEMPLATE` simulation is 6.911Myr and the He-core burning lifetime is 0.635Myr (Figure 3.3). The MESA simulation by Jones et al.

(2015) gives a main sequence lifetime of 6.919Myr and a He-core burning lifetime of 0.651Myr. The percent differences of the lifetimes of the TEMPLATE simulation compared to that of Jones et al. (2015) are 0.12% and 2.5% for the main sequence and He-core burning respectively. A larger difference is found during He-core burning then the main sequence in both time and the amount of mass contained within the convective core (Figure 3.3). The mass enclosed by the convective He-core in the TEMPLATE is larger than the model from Jones et al. (2015). Although, the He-core from the TEMPLATE initially forms with more mass, the two convective cores grow at approximately the same rate up until a point close to the maximum enclosed mass. At this point the model from Jones et al. (2015) slows its growth faster than the TEMPLATE. The larger initial mass and the slow stop of the convective He-core lead to the larger CO-core mass discussed above.

Because of the relatively small variations found in the TEMPLATEsimulation compared to the simulations given by Jones et al. (2015), the main sequence and He-core burning evolution of the TEMPLATEsimulations are taken to be similar enough to the models presented by Jones et al. (2015). The variation of the simulations presented here are therefore representative of variations that would be found in other codes, if similar CBM studies were preformed.

3.2.4 Time Resolution Sensitivity

The time resolution was tested for the main sequence and He-core burning evolutionary phases of the TEMPLATE model to make sure the CO-core mass at the end of He burning did not change significantly. The CO-core mass was tested because the evolution of the metal burning cores is sensitive to this value, as this values mimic a different ZAMS mass (Sukhbold & Woosley, 2014).

MESA solves the stellar structure equations as well as other modules implicitly in time and space. The spatial resolution was tested by Jones et al. (2015) and was not repeated here. Through the evolution of the TEMPLATE simulation, the time step is limited primarily by the two parameters, `varcontrol_taget` and `dX_nuc_drop_limit`. The `varcontrol_taget` parameter acts as a target for the time step by limiting the variation in the structure. Between time steps the difference between a given structural parameter is checked against this value and the time step is adjusted depending on how the variation compares to the value. The parameter `dX_nuc_drop_limit` limits the change in abundances from nuclear burning and mixing, and the time step

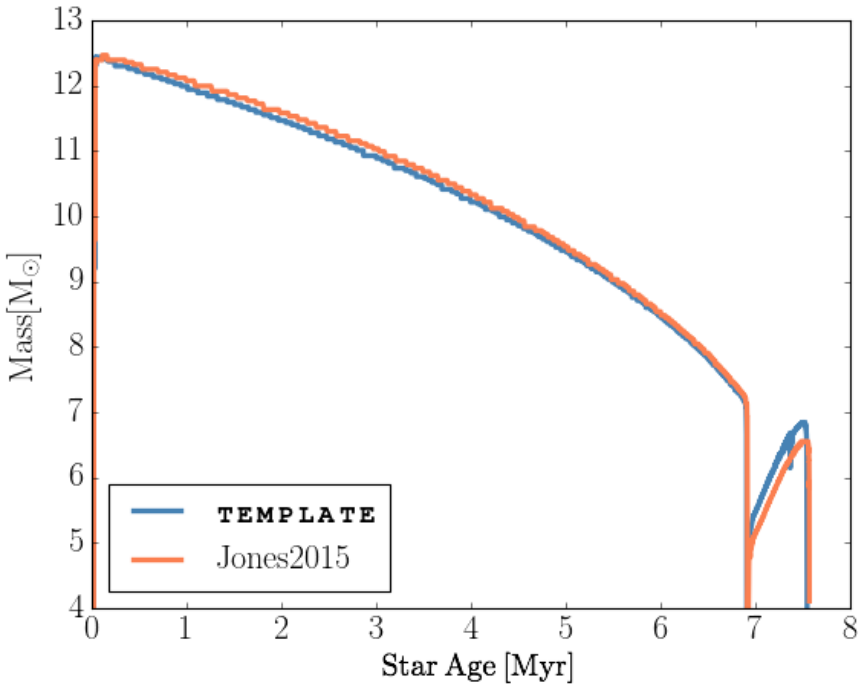

Figure 3.3: The convective core mass along the main sequence and He-core burning for the TEMPLATE simulation and the M25 MESA simulation from Jones et al. (2015) (Figure 1 of Jones et al. (2015)). The two core masses show good agreement along the main sequence but the TEMPLATE simulation has a higher convective He-core mass.

is reduced by a fraction of this value if the limit is reached. Throughout the main sequence and He-core burning of the TEMPLATE simulation, varcontrol_taget primarily controls the time step, although near the end of He-core burning, when mixing from above the convective He-core becomes important, dX_nuc_drop_limit limits the time step. The two parameters where varied independently over a range of values and the CO-core mass, $M_{\rm CO}$, was plotted (Figure 3.4). Variations in $M_{\rm CO}$ is large for values of varcontrol_taget ≥ 0.0001. At values less than this, the $M_{\rm CO}$ shows a variation of $\approx 0.04 M_\odot$, relatively small compared to the larger values. The values of dX_nuc_drop_limit give a variation of $0.054 M_\odot$ which is much less that that of the varcontrol_taget variation of $0.52 M_\odot$. The values chosen for the simulations were varcontrol_taget $= 5 \times 10^{-5}$ and dX_nuc_drop_limit $= 1 \times 10^{-4}$ as to provide a reasonable result without over-resolving stages of evolution.

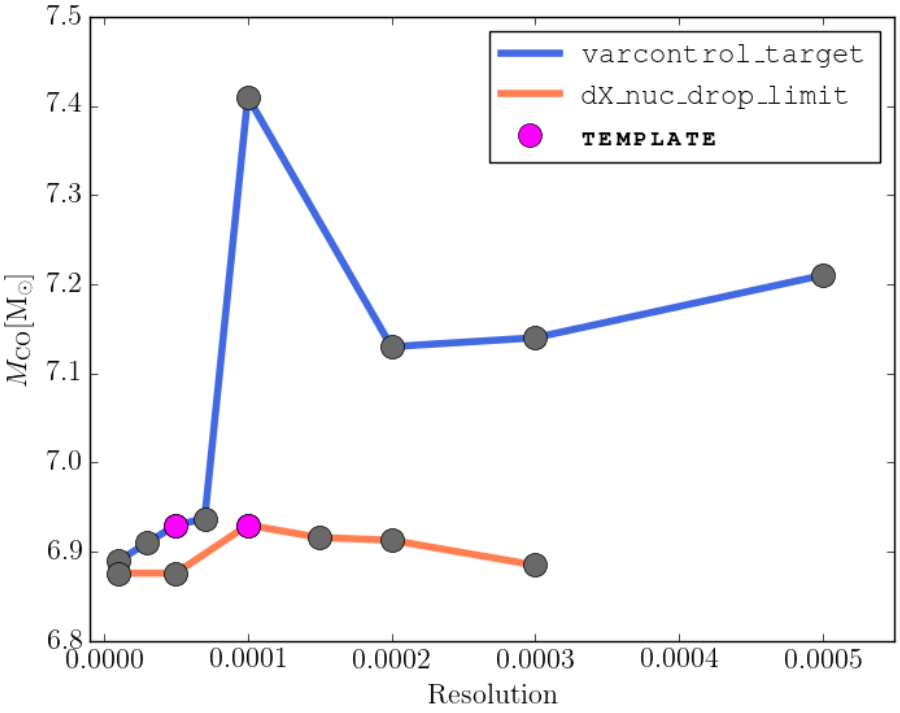

Figure 3.4: Values of M_{CO} after He-core burning for different values of `varcontrol_target` and `dX_nuc_drop_limit`. The plot shows the value of M_{CO} drop for small values of `varcontrol_target` whereas the simulation is not as sensitive to changes in `dX_nuc_drop_limit`. The pink dotes represent the values used to compute the simulations.

3.3 Results

The post He-core structure of the simulations for each run set (C, ONe and Si) is compared below. For each set of simulations, the relevant burning stages are examined with a focus on the effects of convection on the stellar structure. Each model was run to collapse so that the effects of different $f_{\rm CBM}$ values could be seen in later burning stages and the presupernova structure. The presupernova compactness and production factors are also determined for each run. Although the nucleosynthesis is not the primary focus of this investigation, key results are demonstrated with appropriate abundance profiles. Main structural differences arise from the interaction of C, Ne and O convection zones during C, Ne and O core burning. These differences in structures have a non-monotonic affect on the compactness of the simulations. Structural differences are caused primarily by dredge-ups and shell merges between the C and Ne shells. Evidence of these mixing mechanisms can appear in the abundances of the material ejected by the supernova explosions, provided the Ne ash can be mixed high enough by the C shell.

3.3.1 CBM from core He depletion: The C simulations

C-core burning

In the TEMPLATE simulation and all of the simulations which implement enhanced CBM from the beginning of C burning, C-core burning begins radiatively and then transitions into convection as the first convective C-shell forms (Figure 3.5). Once this convective shell forms, it grows as material from above and below is mixed into the convection zone. At similar times during the convective C-shell evolution, when the C-burning luminosity reaches its peak, simulations with enhanced CBM have a slightly smaller ^{12}C/ ^{20}Ne ratio (Figure 3.6). Entrainment from above mixes ^{12}C, ^{20}Ne and ^{16}O into the convection zone where the ^{12}C can burn. From below, entrainment erodes the ONe-core formed by previous radiative C burning, mixing ^{20}Ne, ^{24}Mg and ^{25}Mg into the convection zone. At the bottom boundary the amount of entrainment increases for larger values of $f_{\rm CBM}$ deepening the C-shell in mass coordinate (Figure 3.7). This increased entrainment can reduce the ONe-core mass experienced by the next convective C-shell, and subsequently, the Ne-core. Table 3.2 gives the ONe-core masses at the beginning of Ne burning, which in the C2 and C3 cases, are effected by the second convective C-shell (Figure 3.5).

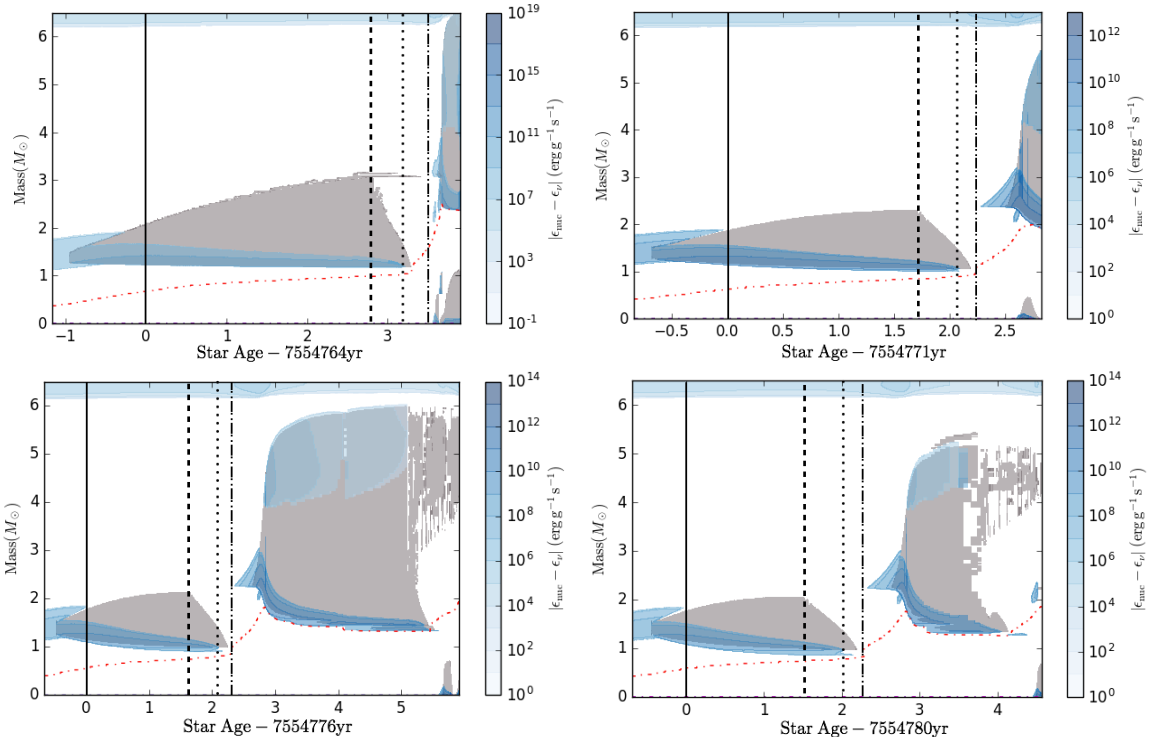

Figure 3.5: Kippenhahn diagrams for the `C` simulations with increasing values of $f_{\rm CBM}$. The diagrams are for the **`TEMPLATE`** (top left), `C1` (top right), `C2` (bottom left) and `C3` (bottom right) simulations. They show the evolution of the first C-shell up to the beginning of the convective Ne-core. The x-axis is time from the point of maximum L_C in the convective C-shell (Figure 3.8). L_C is the luminosity due to C burning. The dashed black line is the point where convection reaches its maximum extent in mass and the dotted black line is the point where convection reaches its lowest (Figure 3.7). The dash-dotted black line refers to Figure 3.9, where the structure left behind by convection can be seen.

The C burning luminosity, $L_{\rm C}$, of the first convective C-shell decreases with increasing values for $f_{\rm CBM}$ (Figure 3.8). The relatively low values of $L_{\rm C}$ show when convection stops, around $L_{\rm C} \approx 10^{5.5}{\rm L}_\odot$ for all simulations. In the **`TEMPLATE`** case the first convective C-shell lasts for $\approx$ 1.1yr longer then the cases with enhanced CBM, with a lifetime of 4.2yr. The lifetimes of the `C1`, `C2` and `C3` simulations are 2.9yr, 2.7yr and 2.6yr respectively. The $L_{\rm C}$ of the **`TEMPLATE`** simulation decreases slower and obtains a higher maximum than the other cases, leading to the longest lifetime for this shell (Figure 3.8). The simulations with enhanced CBM, which have shorter lifetimes, experience lower maximum $L_{\rm C}$ (Figure 3.8). These simulations also entrain less material from above before convection stops (Figure 3.5, 3.7). The entropy profiles of these shells at the maximum extent of the convection show that simulations

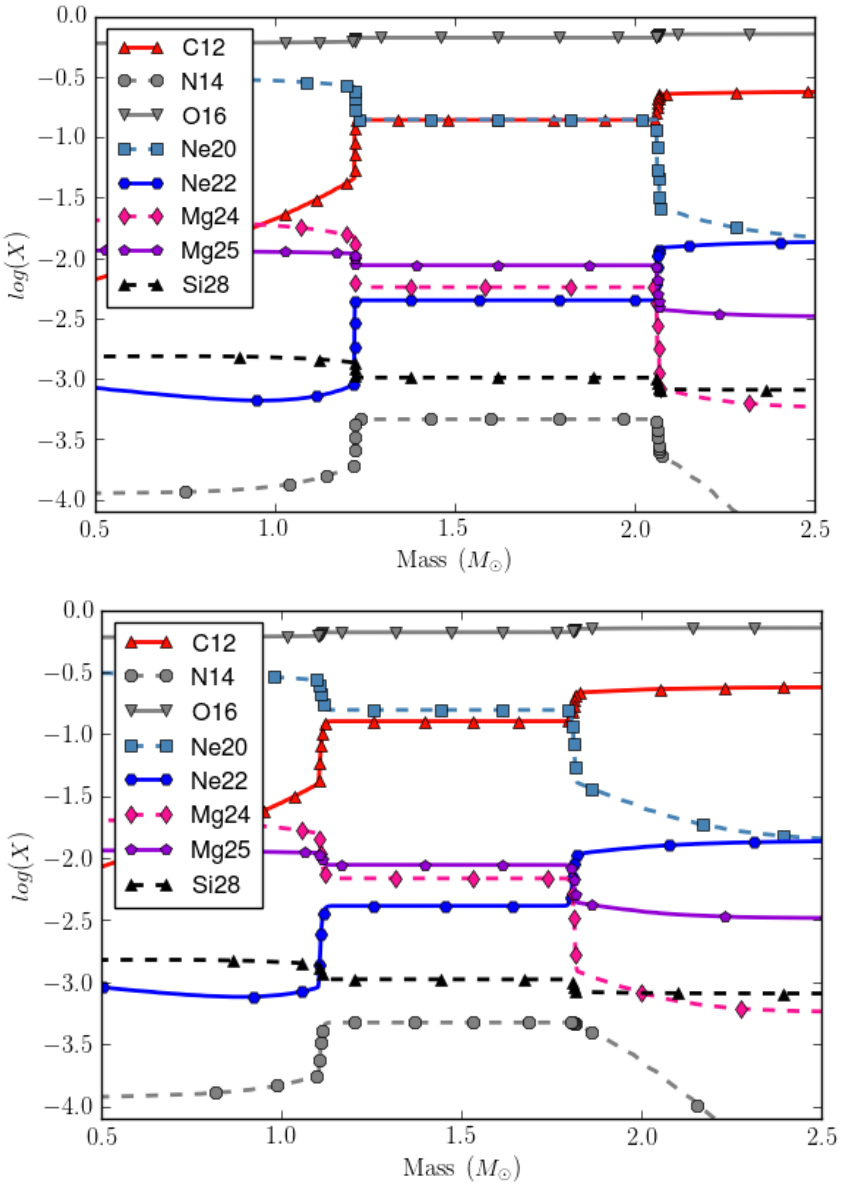

Figure 3.6: Abundance profiles for the `TEMPLATE` and `C2` simulations. The profiles are taken at the maximum L_C (solid black lines in Figure 3.5). The horizontal composition in the centre of each plot shows the position of the first C-shell. The `C2` simulation is representative of the `C1` and `C3` simulations which show similar trends in abundances.

with enhanced CBM are less effective at mixing ash higher in mass coordinate and therefore less ^{12}C, ^{20}Ne and ^{16}O will be mixed in from above. However, simulations with enhanced CBM extend deeper into the ONe-core with increasing $f_{\rm CBM}$ (Figure 3.7). As these shells extend deeper, C ash is mixed into the convection zone, primarily increasing the abundances of ^{20}Ne and ^{24}Mg (Figure 3.6).

The distribution of ash left behind by the first convective C-shell determines the starting point for the second C-shell (Figure 3.5, 3.9). All simulations run in this study experience a second convective C-shell although the evolutionary timing and position of that shell change depending on the CBM strength. After the end of the first convective C-shell, radiative C burning increases the ONe-core mass (Figure 3.5). As with the first convective C-shell, the second convective C-shell begins as radiative C burning although the following convection zone quickly develops. This radiative burning starts at the highest extent of the first convective C-shell. C ash mixed up by the first convection zone becomes frozen into the structure after convection stops (Figure 3.9). This frozen in upper boundary of the first C-shell defines the bottom boundary of the second C-shell until CBM is able to transport material across it, deepening the convection zone in mass (Figure 3.5, 3.9). In the `TEMPLATE` simulation, with minimal CBM, the second C-shell doesn't extend significantly deeper into the unburnt C below (Figure 3.5). In cases where the CBM is high, larger amounts of ^{12}C are entrained from above, mixing with the C ash entrained from below. The deeper the ^{12}C is transported, the deeper the second C-shell can reach before burning out or being extinguished by Ne or O-core burning.

Ne, O and Si-core burning

If the enhanced CBM is allowed to continue in the `C` simulations past Ne-core burning, the interaction of the convection zones will affect not only the C-shells but the Ne and O-cores as well. The simulations found in Figure 3.10 are the continuation of the `C` core simulations run to collapse. In these cases the internal structure left behind by the CBM in the C-shells, discussed in Section 3.3.1, directly affects the remaining evolution of the simulation (Figure 3.5, 3.10). Two of these effects are the number of convective C-shells that develop, and the shell mergers that appear in simulations with high values of $f_{\rm CBM}$.

The `TEMPLATE` simulation has two large convective C-shells during its evolution (Figure 3.5, 3.10). This simulations second convective C-shell experiences limited

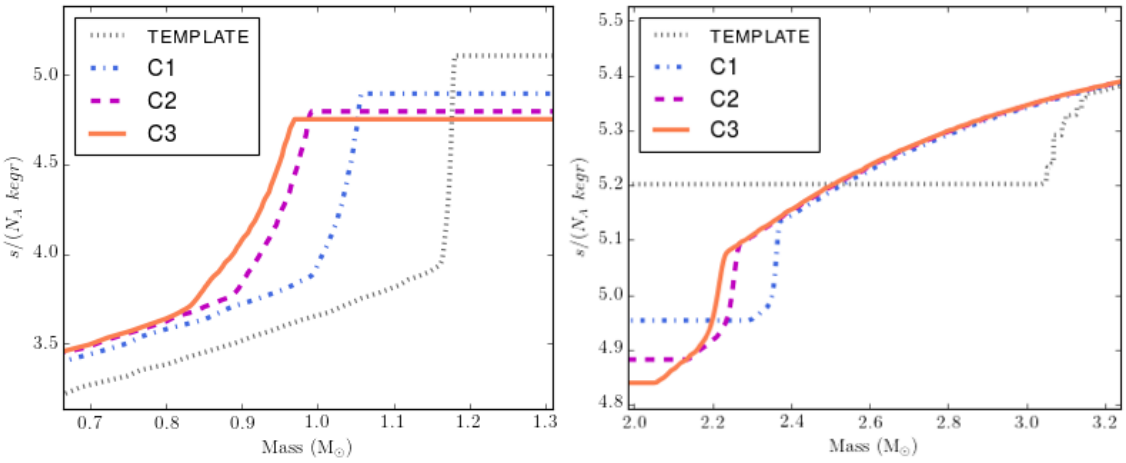

Figure 3.7: Entropy plots for the bottom (left) and top (right) of the first convective C-shell of the `C` simulations. The entropy profiles of the bottom of the convection zone are taken when L_C drops and the shell reaches it deepest in mass (black dotted line in Figure 3.5). The entropy profiles of the top of the shell are taken when the shell reaches its maximum height in mass (black dashed line of Figure 3.5).

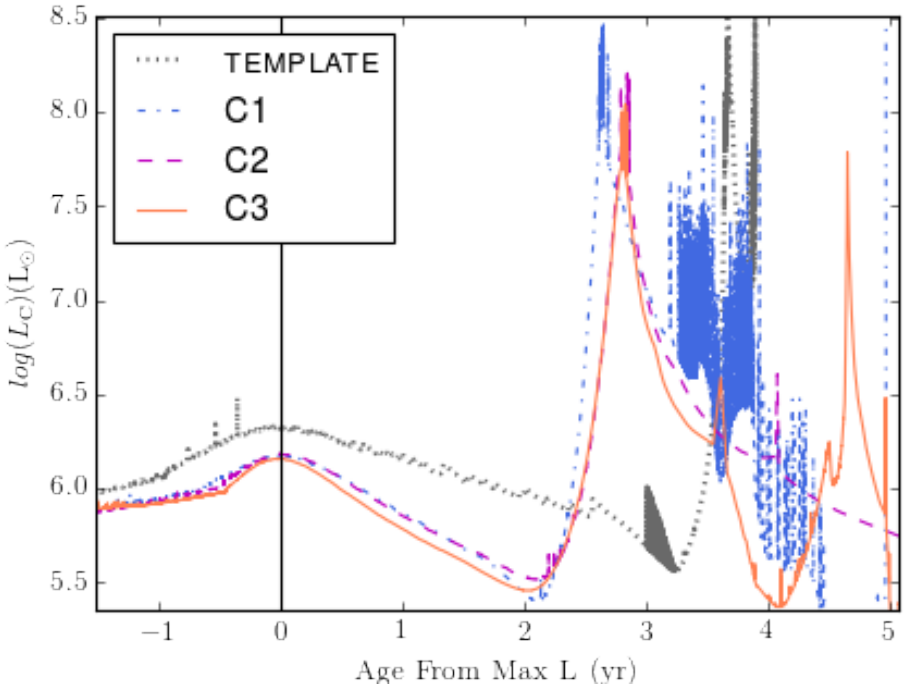

Figure 3.8: Plot of the log of the luminosity due to C burning, L_C, across the first convective C-shell (Figure 3.5). The x-axis is time in years from the maximum L_C (solid line). The convection zones can be seen for times less then $\approx$ 3yr. The spikes found to the right of the plot are due to C-shell interactions with the Ne and O burning cores and shells later in the evolution.

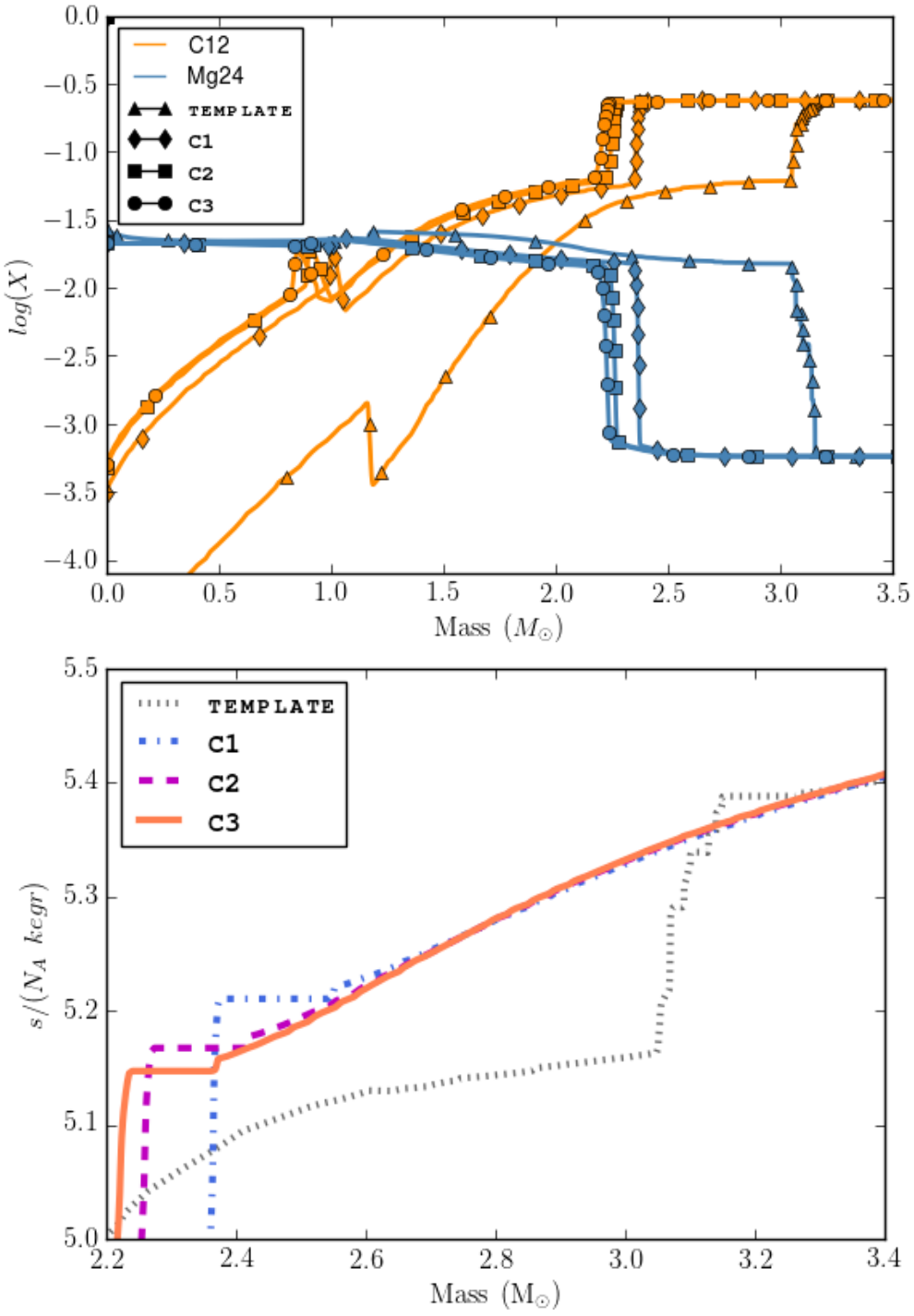

Figure 3.9: The plot on the left is the abundance of ^{12}C and ^{24}Mg left behind by convection in the first C-shell for the `C` simulations (dash-dot line of Figure 3.5). The plot on the right is the entropy profile when the second C-shell begins to convect. Convection in the second C-shell starts at the highest extent in mass of the first C-shell as seen by the flat portion of the entropy profile.

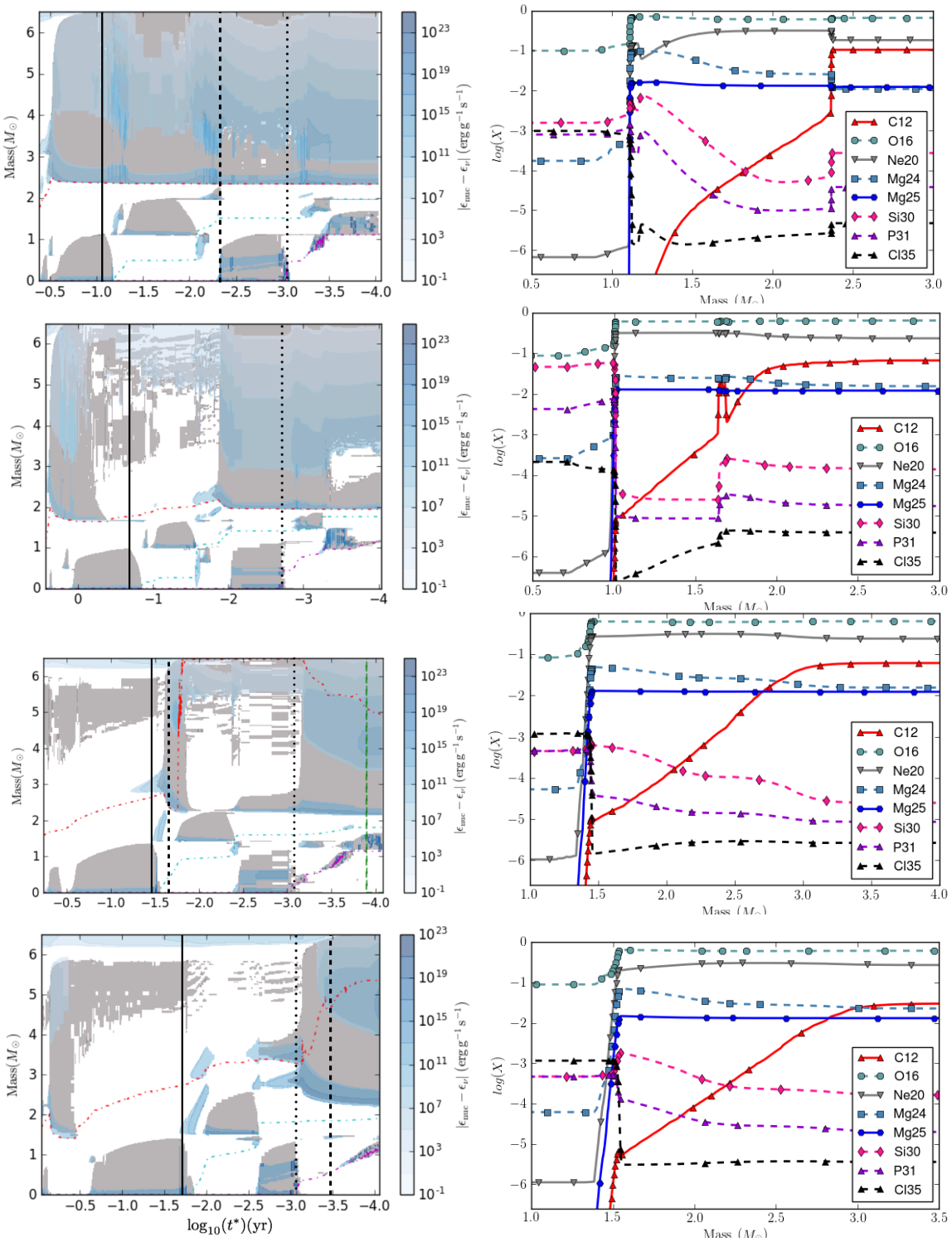

Figure 3.10: Kippenhahn diagrams for the `C` simulations with increasing values of $f_{\rm CBM}$. Starting from the top, the diagrams are for the `TEMPLATE`, `C1`, `C2` and `C3` simulations. The diagrams show the evolution from Ne-core burning to $\approx$ 1hr before collapse. The evolution here is a continuation from Figure 3.5. The plots on the right are abundance profiles taken at the point of highest $L_{\rm O}$ in the O-core (solid black line). $L_{\rm O}$ is the luminosity due to ^{16}O burning. The dotted black lines are the points where the entropy profiles are taken in Figure 3.11. The dashed black lines refer to Figure 3.12, 3.17 and 3.18.

entrainment from below so that the ONe-core mass, after this shell has developed, remains roughly constant at about $2.35M_{\odot}$ (Figure 3.10, 3.11). In the `C1` simulation, which experiences three convective C-shells throughout its evolution, the second convective C-shell starts before Ne-core burning. After the convective O-core forms, the bottom convective boundary of the second C-shell moves further out in mass, decreasing the mass contained by the convection zone (Figure 3.10). During O-shell burning, the ONe-core mass increases to a maximum value of about $2.1M_{\odot}$ before convective Si-core burning begins and a third convective C-shell forms. The bottom boundary of this shell begins to entrain material and the ONe-core mass drops to around $1.9M_{\odot}$ before the end of the stars life (Figure 3.11). For the `C2` simulation, four convective C-shells are experienced during the evolution. O-core burning between the second and third convective C-shells pushes the ONe-core boundary up to $2.7M_{\odot}$ (Figure 3.10, 3.12). When the third convective C-shell forms, entrainment from the bottom is large enough to reach the ash left behind by radiative Ne burning, in the form of ^{16}O, ^{24}Mg and ^{28}Si (Figure 3.11, 3.12). This shell reaches a depth of $2.27M_{\odot}$ at the black dotted line in Figure 3.12. Although the convective boundary only reaches the top of the Ne ash deposit, because this convective shell spans a large portion of the star, the ^{16}O, ^{24}Mg and ^{28}Si that is mixed into the convection zone is brought up to the top, at around $6.5M_{\odot}$. The `C3` simulation also develops four C convection zones during its evolution (Figure 3.5, 3.10). Where the `C2` simulation experiences something like a classical *dredge-up* (convection entrains ash from a previous burning stage), in the `C3` simulation the convective Ne and C-shells merge after convective Si-core burning (near the dotted line in Figure 3.10). During Si-core burning, a radiative Ne-shell forms at about $2.6M_{\odot}$. At this point in time, C starts burning radiatively at the bottom of the ONe-core boundary, $3.4M_{\odot}$. The C-shell becomes convective and begins to erode the ONe-core (Figure 3.15). After this, the Ne-shell also starts to convect, mixing material in from the top. The difference in entropy between the Ne and C-shell is relatively small in this case, at $\Delta s/N_{A}\text{kerg} \approx 0.2$ (Figure 3.11). In the `TEMPLATE` simulation, a Ne-shell forms under the second C-shell with an entropy difference of $\Delta s/N_{A}\text{kerg} \approx 2$ (Figure 3.13). The convective boundaries of the two shells meet and form one convection zone spanning $4.4M_{\odot}$ (Figure 3.16). Relative to the C-shell in the `TEMPLATE` simulation, the abundances of ^{24}Mg and ^{28}Si increase as the ash from form Ne burning is mixed into the convective C-shell (Figure 3.17).

The `C` simulations all experience two significant burning regions in the large convective C-shells, one at the top and the other at the bottom (Figure 3.10). Figure 3.18

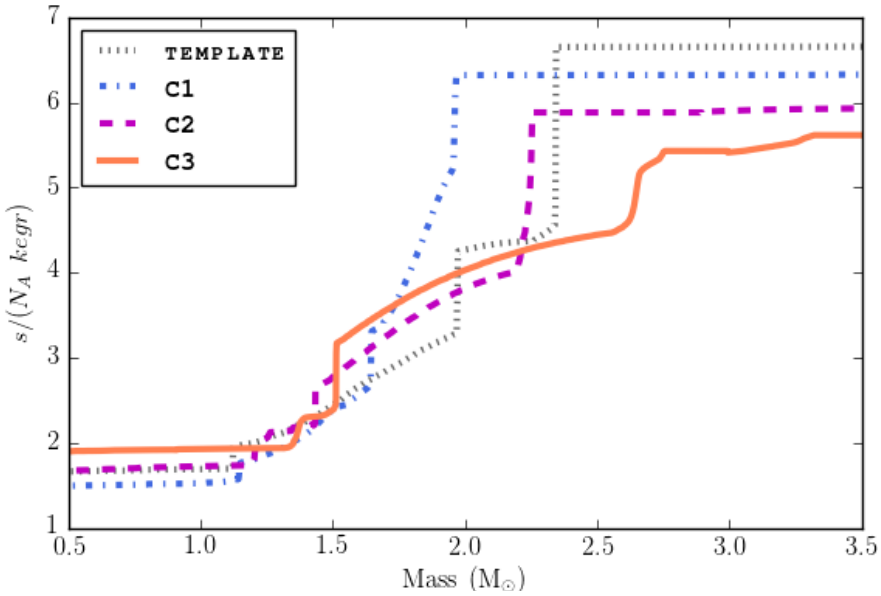

Figure 3.11: Entropy profiles for the `C` simulations. The profile for the `TEMPLATE` simulation is taken at the maximum luminosity due to O burning in the O-core (solid black line in Figure 3.10) and the profile for the `C1` simulation is taken at the end of Si-core burning (dotted black line in Figure 3.10). The profile for the `C2` simulation shows the depth of the third C-shell after it has entrained Ne burning ash from below (dotted black line in Figure 3.10). The `C3` profile is taken before the C Ne-shell merger around $2.5-3.5 M_\odot$ (dotted black line in Figure 3.10). Both the `TEMPLATE` and `C1` profiles show the depth of the C-shell near the end of the stars life, as these values do not change significantly passed these points.

shows the specific luminosity from $^{12}C + {}^{12}C$, $^{20}Ne + \alpha$ and $^{24}Mg + \alpha$. Peak energy generation at the top comes from ^{20}Ne and ^{24}Mg α capture, as ^4He can be mixed into the convection zone from above. Deeper in the convection zone, $^{12}C + {}^{12}C$ dominates the energy production from about $2.5 - 4.2 M_\odot$. The C burning produces ^4He in this region and this ^4He is used in further α capture on ^{20}Ne and ^{24}Mg at the bottom of the convection zone. Although the profiles for ^{20}Ne and ^{24}Mg are fairly flat in Figure 3.18, the profile of ^4He has a minimum in the convection zone. Because the ^4He profile is not flat, the time scale in which ^4He is being consumed and produced in much faster then the convective turn over time scale, which is about 5hr. This implies that the instantaneous mixing assumption of MLT might not be valid. In 3D, a convective flow such as this would need to be treated as a convective reactive flow, where the fluid dynamics are coupled to the reactions. This is necessary because the local turbulent mixing in a given region would determine the concentration of each species and the energy from the reactions would affect the fluid dynamics.

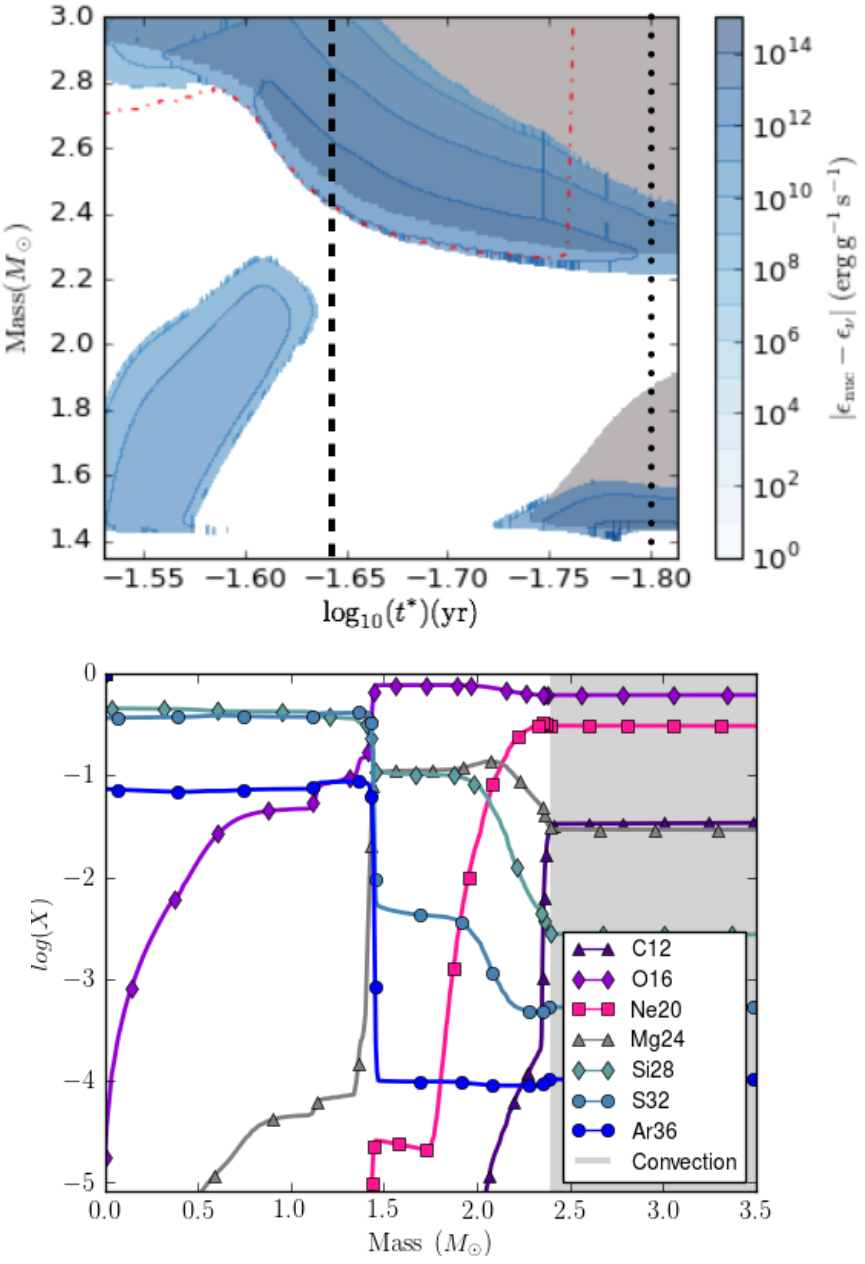

Figure 3.12: Kippenhahn diagram and abundance profile from the `C2` simulation as the third C-shell bottom boundary approaches the Ne burning ash below. The dashed black line is the point where the abundance profile is taken. This is the same dashed black line as in Figure 3.10. The upper convection zone in the figure is the bottom of the C-shell, a radiative Ne burning region is on the left and the convection zone on the right is an O-shell. The thin dash-dotted red line is the ONe-core boundary. The dotted black line is the point where the convective boundary reaches it deepest in mass. The abundance profile shows the bottom boundary of the convective C-shell mixing in Ne ash from below (grey shaded area).

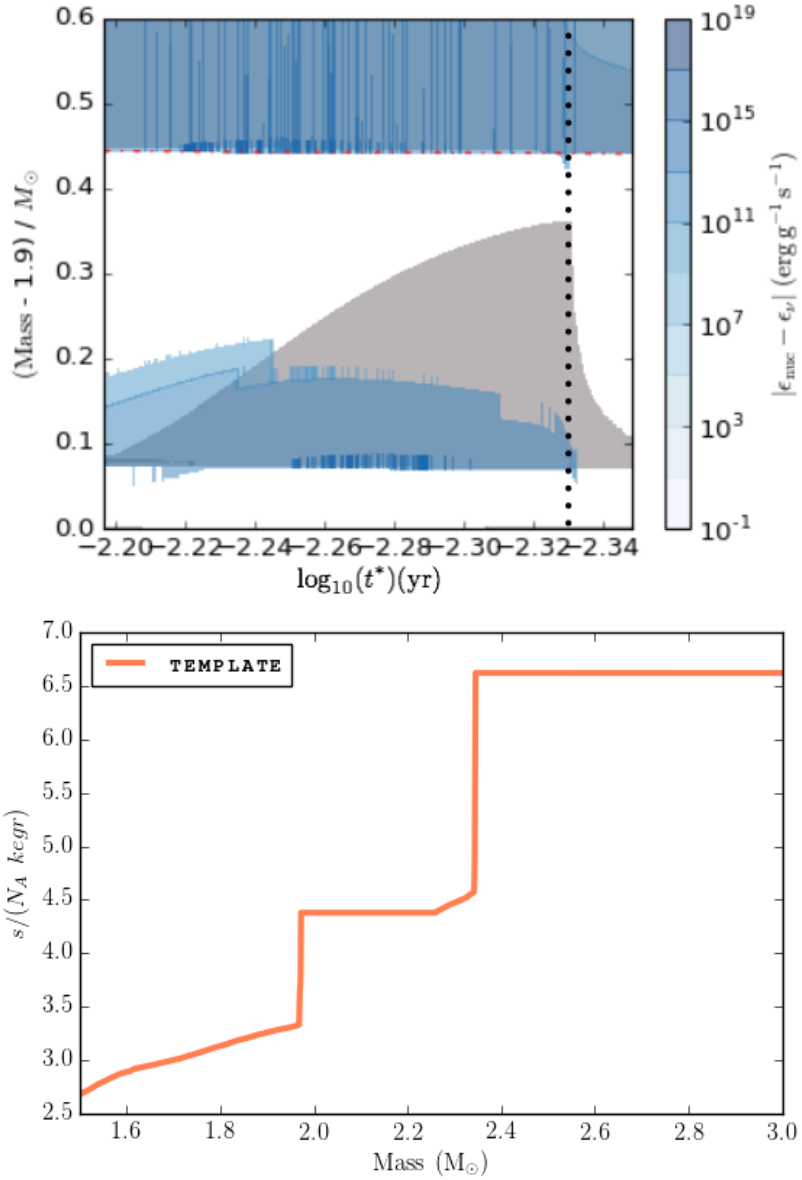

Figure 3.13: Kippenhahn diagram and entropy profile from the `TEMPLATE` simulation. The Kippenhahn diagram shows a Ne-shell underneath a convective C-shell. The entropy profile shows the large entropy gradient between the two convection zones relative to the `C3` simulation (Figure 3.11).

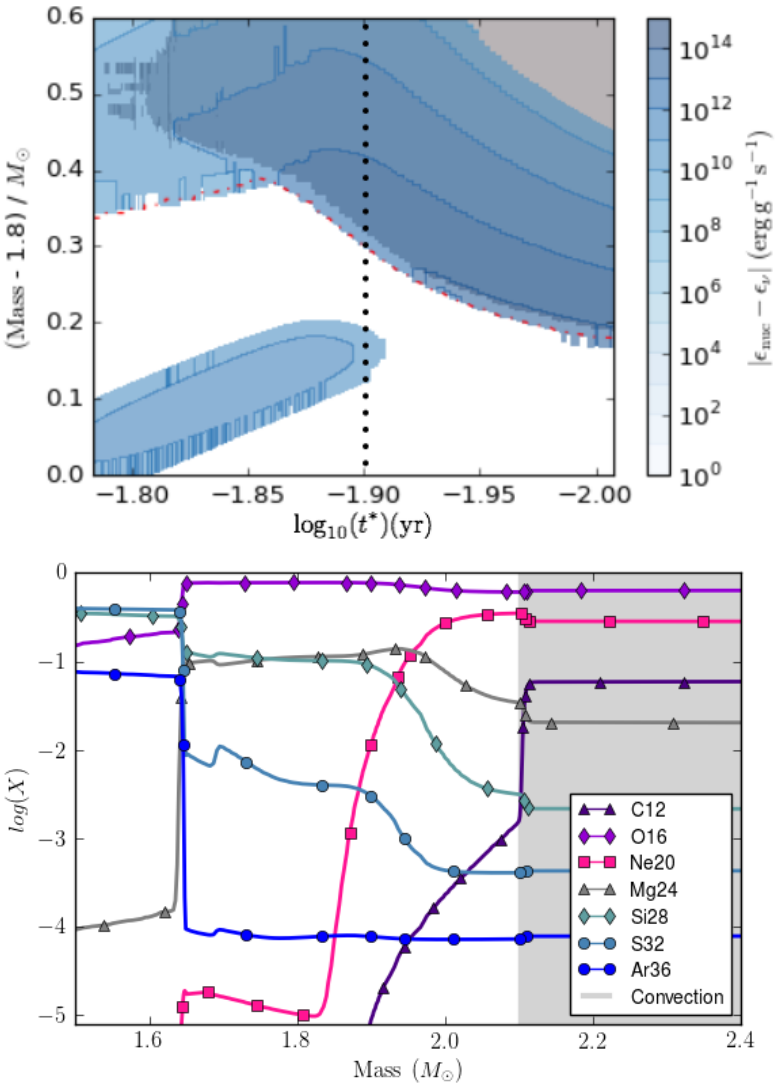

Figure 3.14: Kippenhahn diagram and abundance profile from the `C1` simulation. The bottom radiative region is burning Ne, the upper convection zone is a C-shell. The black dotted line is the point where the abundance profile is taken. The abundance profile shows the ash left behind from the radiative Ne burning as the C convection zone mixes material in from the bottom.

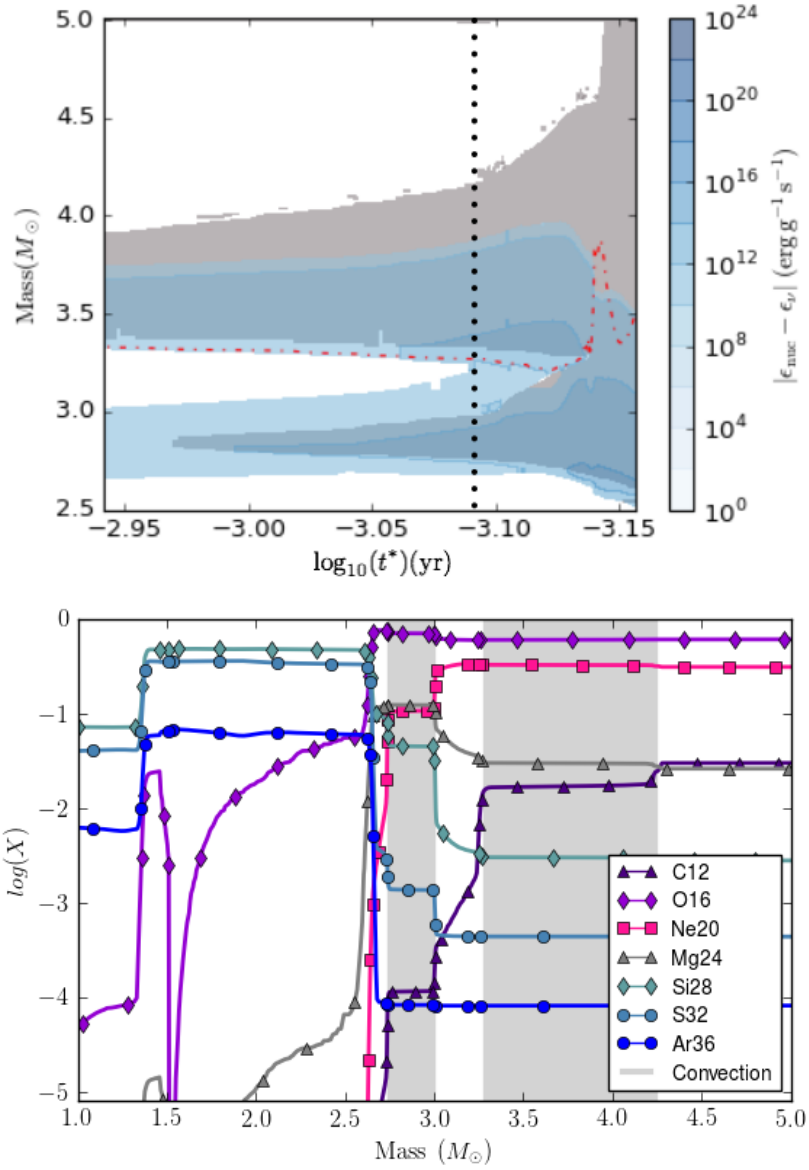

Figure 3.15: Kippenhahn diagram and abundance profile from the `C3` simulation. The Kippenhahn diagram shows the merger of the Ne (bottom) and C (top) shells. The red dash-dotted line is the ONe-core boundary, and the dotted black line is the point where the abundance profile is taken and is the same dotted line as in Figure 3.10. The grey shaded regions on the abundance profile are the convection zones in the Kippenhahn diagram.

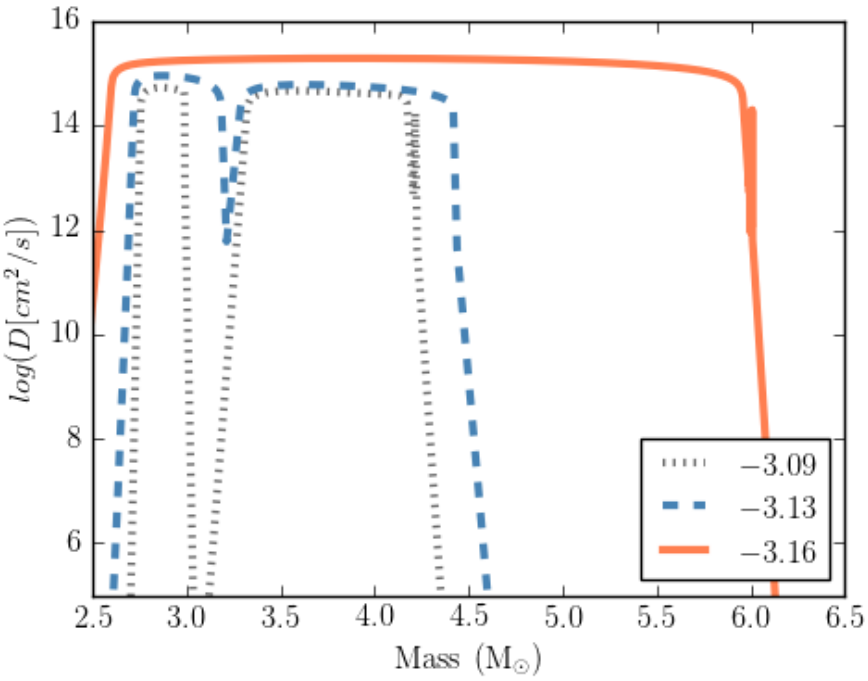

Figure 3.16: Log of the diffusion coefficient over the Ne-O shell merger found in the `C3` simulation. The value in the legend is the time in $log(t^*[\text{yr}])$ over the merger. See Figure 3.10.

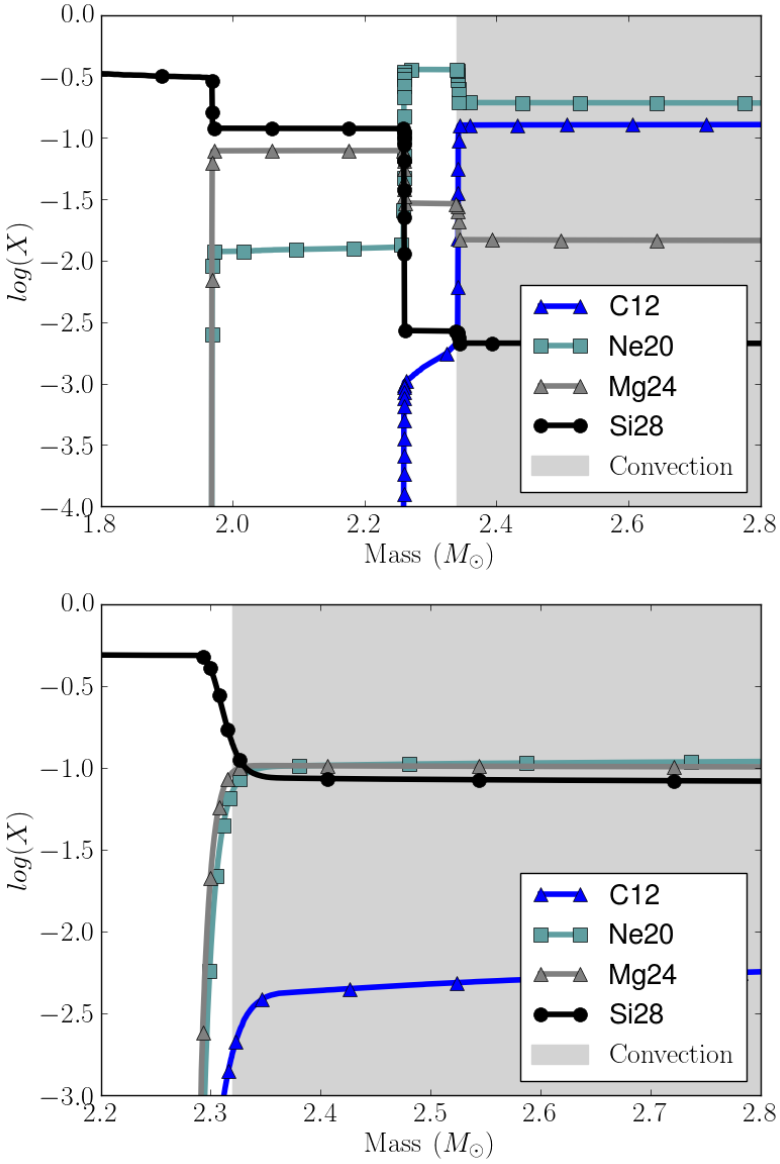

Figure 3.17: Abundance profiles for the `TEMPLATE` (top) and `C3` (bottom) simulations. The abundance profile for the `TEMPLATE` is taken at the dotted black line in Figure 3.13 and shows the distribution of selected elements between the C-shell and radiative Ne burning region. The `C3` abundance profile is taken at $log(t^*[\mathrm{yr}]) = -3.47$ (dashed black line in Figure 3.10) and shows the distribution of species after the C-Ne shell merger.

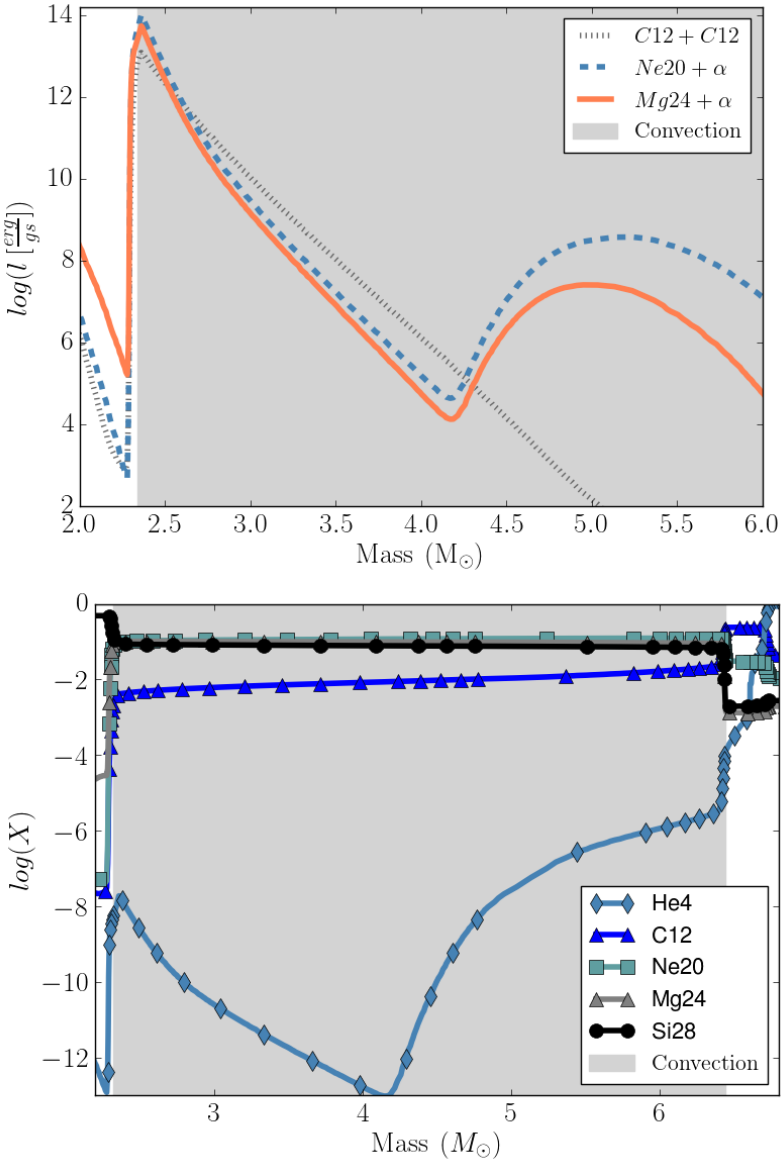

Figure 3.18: Specific luminosity and abundance profile for the C3 simulation after the merger at $log(t^*[\mathrm{yr}]) = -3.47$ (dashed black line in Figure 3.10). The luminosity profile shows the two energy generation regions in Figure 3.10. The abundance profile shows the distribution of ^{4}He in the convective C-shell.

3.3.2 CBM from core Ne ignition: The ONe simulations

Ne and O-core burning

The ONe simulations implement CBM from the beginning of Ne-core burning using the TEMPLATE simulation for the C-core evolution. Because the value for $f_{\rm CBM}$ is applied to all metal burning convective boundaries, some of the characteristics of the enhanced CBM seen in the C simulations are present in the ONe simulations. These simulations show differences in the number of convective C-shells that form, and experience dredge-ups of the C-shells into the Ne ash.

The ONe1 and ONe2 simulations both experience three convective C-shells throughout their evolution as compared to the TEMPLATE which has two (Figure 3.5, 3.19). In many of the simulations in this study (TEMPLATE, C and ONe), when the convective Ne-core forms there is little to no convection in the C-shell above. For simulations with no convective C-shell at this point, the end of convective Ne-core burning is followed by the formation and growth of a convective C-shell. For simulations that have formed a small convective C-shell, after convective Ne-core burning the C-shell mixes in more material from below and increases in mass. The amount of CBM present in this C-shell can delay the formation of the convective O-core (Figure 3.19, 3.20). In the TEMPLATE simulation this does not happen. The second convective C-shell remains until collapse with a bottom boundary at $\approx 2.35 M_{\odot}$. The convective O-core follows Ne-core burning with a relatively short delay of 0.04yr or about 15 days (Figure 3.20). The ONe1 simulation is similar in that the delay from convective Ne-core burning to convective O-core burning is also relatively short, 0.07yr (26 days). Although, for this simulation, the second convective C-shell does not last to collapse, it is extinguished before the end of convective O-core burning at a depth of $\approx 1.77 M_{\odot}$ (Figure 3.19). The ONe2 simulation has a delay of 1.07yr before convective O-core burning (Figure 3.20). In this case the CBM in the second C-shell pushes the bottom boundary to a depth of $1.5 M_{\odot}$. After the bottom boundary of this C-shell recedes, O-core convection starts (Figure 3.19). The ONe3 simulation is similar to ONe2 with a delay of 1.26yr before convective O-core burning. The convective C-shell then recedes after reaching $\approx 1.55 M_{\odot}$ and convection in the O-core begins (Figure 3.19).

As with the C simulations, the ONe1, ONe2 and ONe3 simulations mix Ne burning ash into a C-shell through dredge-ups. In ONe simulations with enhanced CBM, radiative Ne burning reaches a depth high enough for the C-shells to dredge-up the Ne ash (dotted black lines in Figure 3.19). Abundance plots taken at this time

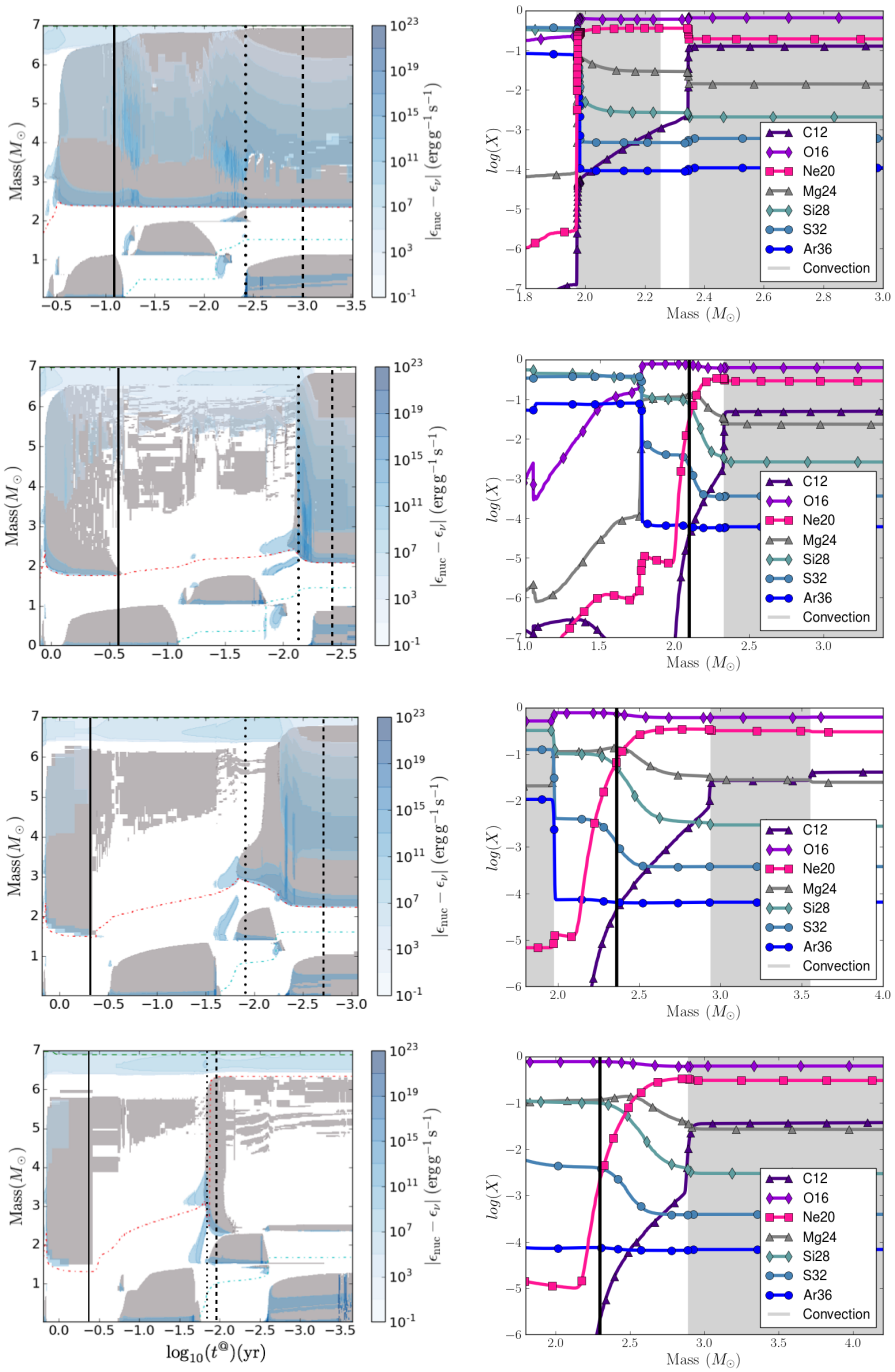

Figure 3.19: Kippenhahn diagrams and abundance profiles for the ONe simulations with increasing values of $f_{\rm CBM}$. Starting from the top, the diagrams are for the TEMPLATE, ONe1, ONe2 and ONe3 simulations. The x-axis of the Kippenhahn diagrams is the log of the time left until the end of convective Si-core burning. The dotted black lines are the point where the abundance profiles are taken. The dashed black line is the point where the abundance profiles are taken in Figure 3.21. The solid line in the Kippenhahn diagram is the point where the C-shell that forms after Ne-core burning reaches is maximum depth in mass. The solid black line in the abundance profile in the maximum depth of the convective C-shell will reach before the end of convective Si-core burning.

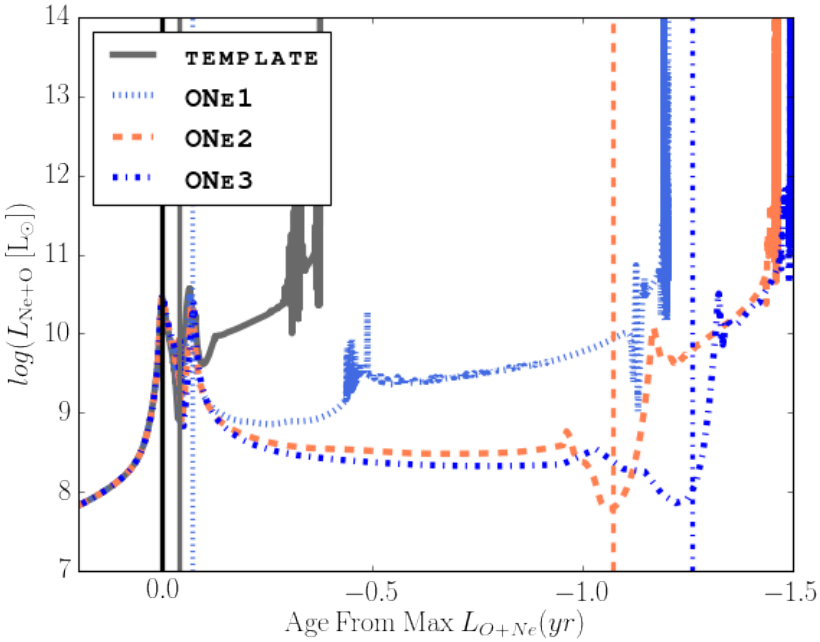

Figure 3.20: Luminosity due to $^{16}O + {}^{16}O$ and $^{20}Ne + \alpha$. The x-axis is time in years from the maximum luminosity in the Ne convective core (solid black line). The vertical lines mark the point in time when the O-core becomes convective. The end of each run can be seen as L_{O+Ne} grows and appears vertical.

show the Ne ash distribution lying under the convective C-shell (Figure 3.19). The enhanced CBM in these simulations promote the growth of the C-shell, decreasing the bottom boundary before the end of core Si burning (black solid line in the abundance profiles of Figure 3.19). The dredge-ups mix ^{24}Mg, ^{28}Si and ^{32}S into the C-shell where they are transported up to a depth $> 6M_\odot$. After the dredge-ups the abundances ^{24}Mg in the convective C-shell increased with increasing values of $f_{\rm CBM}$, whereas the abundance of ^{28}Si increases from the `TEMPLATE` simulation to the `ONe2` simulation but remains roughly the same for the `ONe2` and `ONe3` simulations (Figure 3.21). The C abundance decreases with increasing $f_{\rm CBM}$ with the `ONe3` simulation having more than an order of magnitude less ^{12}C than the `TEMPLATE` and `ONe1` simulations (Figure 3.21).

Despite the lack of influence from enhanced CBM in the C-core as in the `C` simulations in Section 3.3.1, similar characteristics arise in the Ne C-shell dredge-ups and the interactions of the C and Ne-shell formation.

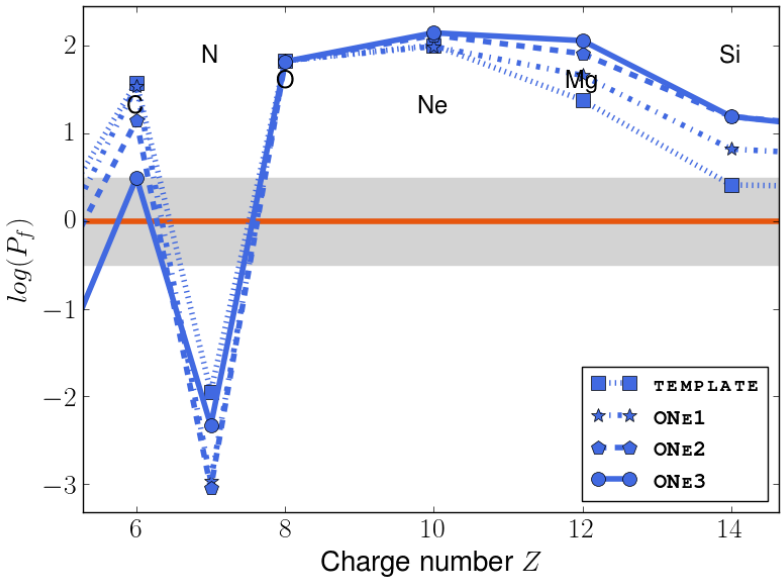

Figure 3.21: Production factor in the C-shell for the ONe simulations after the Ne-C shell dredge-ups. The profiles are taken at the black dashed lines in Figure 3.19. The production factor relative to solar abundance is taken in the same region of the C-shell for the ONe simulations.

Si-core burning

After the beginning of core Si burning the ONe simulations were run to collapse so that the stellar structure left behind by the enhanced CBM in the Ne and O-core could affect the remaining evolution of the simulation. Two of these effects are the number of Si convection zones that develop and the depth of the C-shell near collapse.

The ONe1 and ONe2 simulations develop a convective Si-core followed by two convective Si-shell (Figure 3.22). The second Si-shell of these simulations decreases in mass and forms a thin convective layer over the Fe-core. In the ONe simulations as well as the TEMPLATE, a Si-shell is present at $log(t^*) \approx -6$ around $1.5 M_\odot$ although the TEMPLATE and ONe3 simulations only develop one Si-shell. In the ONe1 and ONe2 simulations, the bottom boundary of the C-shell is at a depth of $2.05 M_\odot$ and $2.22 M_\odot$ respectfully (Figure 3.22, 3.23). The TEMPLATE and ONe3 simulation only forms one convective Si-shell. When these shells forms, the bottom boundary of the convective C-shell is at a mass of $2.34 M_\odot$ and $2.04 M_\odot$ respectively. One difference between the simulations that form one convective Si-shell and the ones that form two, is the Si-core mass before the convective Si-shells start (Figure 3.23). The TEMPLATE and ONe3 simulations have the largest Si-core mass before the start of the convective

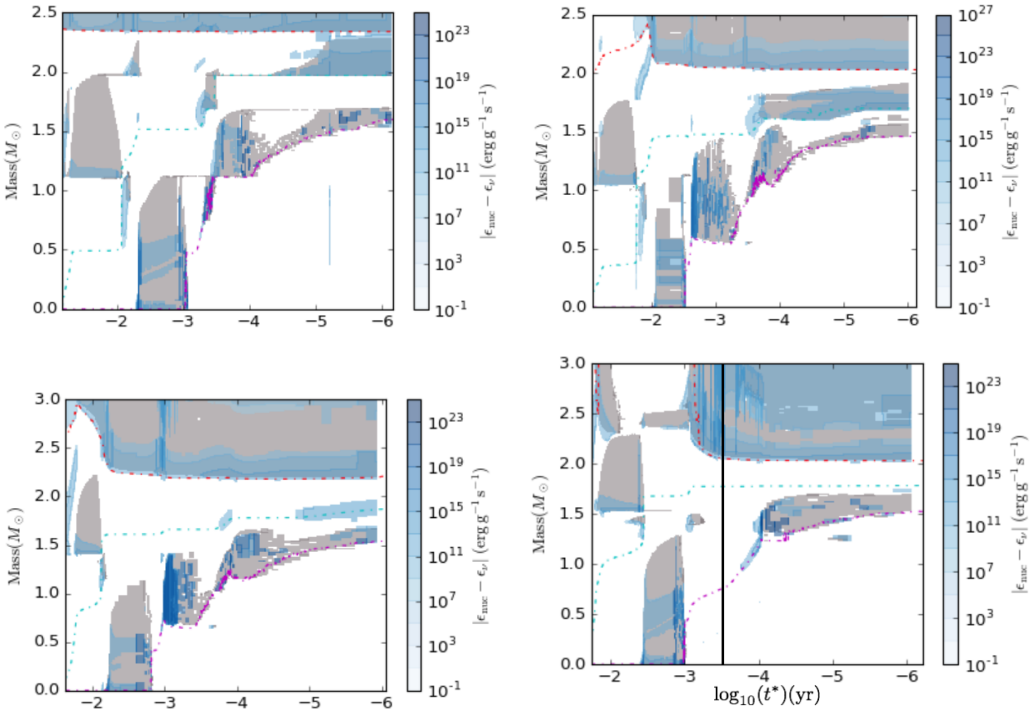

Figure 3.22: Kippenhahn diagrams for the ONe simulations during Si-core burning. Starting from the top, the diagrams are for the TEMPLATE, ONE1, ONE2 and ONE3 simulations. The x-axis is the log of the time left until collapse. The solid black line is the point where the abundance profile is taken in Figure 3.24.

Si-shell of 1.97M$_\odot$ and 1.78M$_\odot$. These boundaries do not increase significantly during the formation of the shells (Figure 3.22). The ONE1 and ONE2 simulations have a Si-core mass of 1.46M$_\odot$ and 1.62M$_\odot$ respectively, before Si-shell burning.

In the ONE1 and ONE2 simulations, at the end of the first O-shell, the bottom boundary of the third C-shell decreases in mass, mixing in Ne ash (Section 3.3.2). These C-shells remain convective until collapse. For the ONE3 simulation, a fourth convective C-shell develops at the end of Si-core burning (Figure 3.22). The bottom boundary of this shell goes deep enough to reach O ash left by the first O-shell (Figure 3.24). The depth of the dredge-ups in these simulations is the last major event in the stars life that will change the ONe-core mass (Figure 3.23). In the ONE1 and ONE2 simulations, this happens at the end of the second O-shell. In the ONE3 simulation, there is no C-shell present when the second O-shell ends, instead this final dredge-up happens at the end of the convective Si-core and is deep enough to entrain O burning ash from the second O-shell (Figure 3.22).

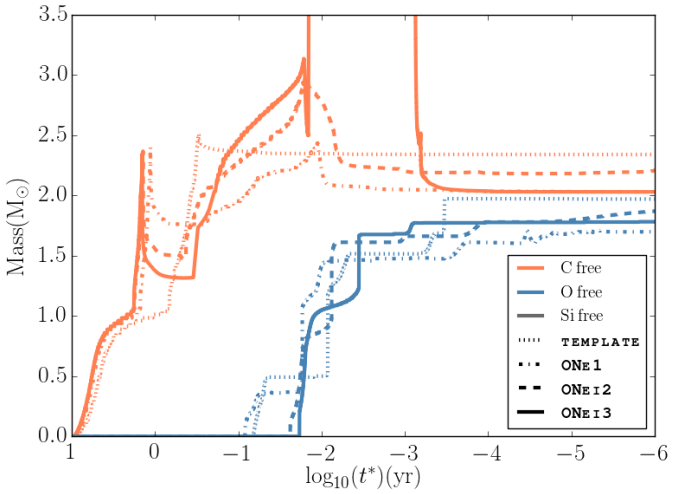

Figure 3.23: The ONe and Si-core masses for the `ONe` simulations. The x-axis is log of the time left until collapse and the y-axis is the enclosed mass from the core. The plot shows the differences in the core masses with respect to the amount of CBM implemented during core Ne, O and Si burning. The small differences in the lines at the end of core C burning ($log(t^*) \approx 1$) is due to differences in the evolutionary time for each simulation. In the `ONe3` simulation, the C-shell present at $log(t^*) \approx -1.5$ recedes and the ONe-core mass moves out to enclose $6.3 M_\odot$ before the fourth convective C-shell develops at $log(t^*) \approx -3$.

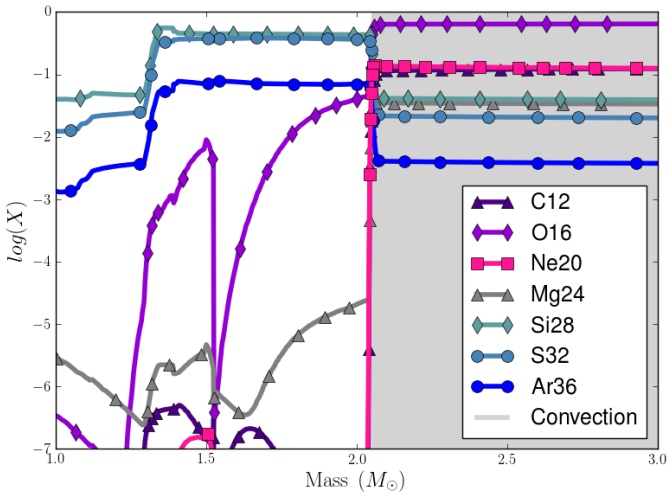

Figure 3.24: The abundance profile of the `ONe3` simulation taken at the solid black line in Figure 3.22. The plot shows the bottom boundary of the C-shell and the distribution of ash left by the previous O burning shell.

3.3.3 CBM from core Si ignition: The Si simulations

As with the ONe simulations, the Si simulations branch from the TEMPLATE at the beginning of core Si burning, and then implement enhanced CBM from that point until collapse. A log central temperature of $log(T_C) = 9.39$ marks the point where the Si simulations begin, which means the enhanced CBM is applied to the Ne and O-shells that form after O-core burning as well as the Si-core and shells that develop (Figure 3.25).

Si-core burning

During Si burning the Ne, O and Si convective shells form relatively close to each other in mass. Because the entropy gradients are smaller in this region than further out, there is a potential for nearby convective shells to merge. In the Si1, Si2 and Si3 simulations, after convective core Si burning, an O-shell forms (dashed line in Figure 3.25) at $log(t^*) \approx -3.5$. The TEMPLATE simulation forms an O-shell later on in its evolution. In the Si1 and Si2 simulations, a convective Ne-shell exists above the O-shell during its formation. The three convective shells are only separated from the convective C-shell by a very small mass, in some cases, $< 0.05 M_\odot$. Despite the proximity and enhanced CBM of these shells, they do not merge (Figure 3.26). Strong entropy gradients between these shells inhibit the mixing across the shell boundaries and prevent the shells from merging (Figure 3.27). Although these shells don't merge, because of the enhanced CBM of the Si simulations and the small separation of the convective shells, some mixing still occurs between them. The exponential decay of the diffusion coefficient across the boundary allows for a region outside of the convection zone to mix with material from the convection zone. In this case, both convection zones are mixing into this small radiative region separating them (Figure 3.26). Although mixing between these convective shells is shown in the Si simulations, the net effect of this mixing is relatively small with respect to the abundances in the C-shell (Figure 3.30).

Similar Ne and O-shells form later in the stars life as well (Figure 3.25). Specifically, in the Si2 simulation, a convective Si-shell approaches an O-shell underlying the convective C-shell (black solid line in Figure 3.25). A slow mixing event such as this would have little effect on the abundances in the C-shell. This is because the convective turn over time scale of the C-shell at this time is $\approx$ 5hr, and the star has roughly the same amount of time left before collapse. Therefore, any mixing event

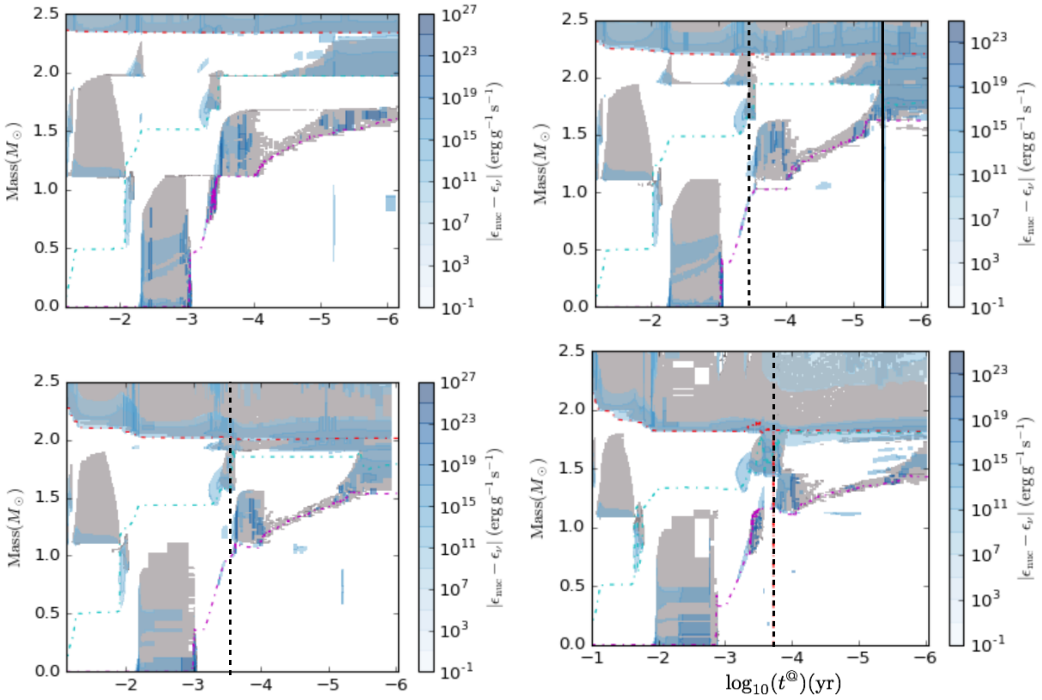

Figure 3.25: Kippenhahn diagrams for the `Si` simulations. Starting from the top, the diagrams are for the `TEMPLATE`, `Si1`, `Si2` and `Si3` simulations. The black dashed lines are where the entropy profiles are taken in Figure 3.27. The convection zone at the top of every diagram is the second C-shell and the convective core starting at $log(t^*) \approx -2$ is the convective Si-core.

that didn't significantly decrease the convective turn over time scale of the C-shell may not be able to mix material high enough in time to surpass the fallback radius.

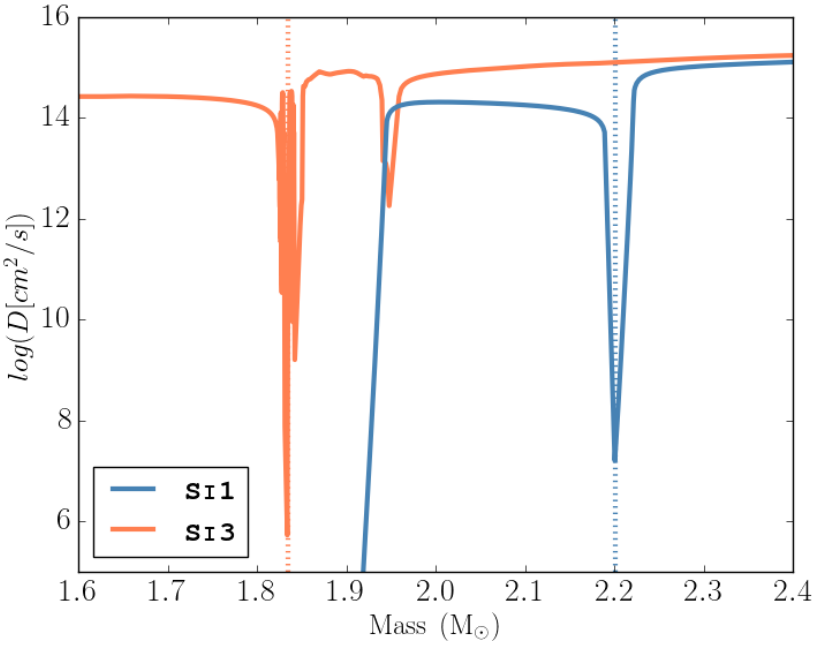

Figure 3.26: The diffusion coefficient used by MESA for the `SI1` and `SI3` simulations for the bottom of the C-shell. The profiles are taken at the black dashed lines in Figure 3.25. The dotted lines are the convective boundaries between the convection zones. The `SI2` simulation was excluded for clarity as the diffusion coefficient around this boundary becomes noisy similar to the boundary for the `SI3` simulation.

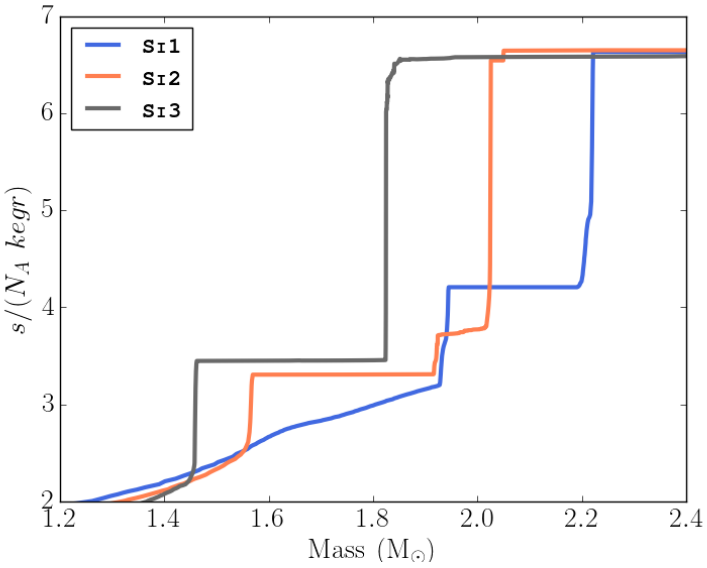

Figure 3.27: Entropy for the `SI1`, `SI2` and `SI3` simulations for the bottom of the C-shell. The profiles are taken at the black dashed lines in Figure 3.25.

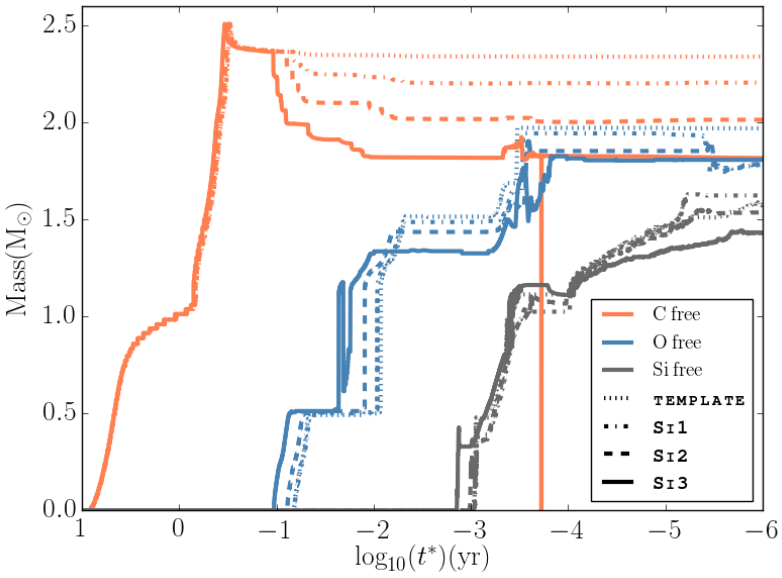

Figure 3.28: The ONe, Si and Fe-core masses for the `SI` simulations. The x-axis is log of the time left until collapse and the y-axis is the enclosed mass from the core. The plot shows the differences in the core masses with respect to the amount of CBM implemented during core Si burning. The small differences in the lines before core Si burning is due to differences in the evolutionary time for each simulation.

3.3.4 Compactness Evolution

The bounce compactness of a massive star, given by Equation 1.26, is a parameter that has been shown to be significant in determining the success of a supernova explosion, where lower values of the bounce compactness have been found to favour explosions (O'Connor & Ott, 2011). The parameter is generally evaluated at the presupernova stage, where the presupernova stage is defined for when the infall velocity of the Fe-core reaches 1000km/s. A mass of $M = 2.5\mathrm{M}_{\odot}$ is generally chosen as it is the relevant mass scale for black hole formation (O'Connor & Ott, 2011) and characterizes the density gradient outside of the Fe-core (Sukhbold & Woosley, 2014). Sukhbold & Woosley (2014) found that, among other things, the non-monotonicity of the presupernova compactness is strongly dependent on the ONe and Si-cores and their interaction with the C and O burning shells. The position and timing of these shells are, in turn, dependent on the strength of the CBM used to compute them.

If the presupernova compactness provides a reasonable estimate for the bounce compactness, then investigating how the compactness changes throughout the evolution of the star with respect to CBM should provide more insight into the non-monotonicity found by Sukhbold & Woosley (2014). The evolutionary compactness at $M = 2.5\mathrm{M}_{\odot}$ is plotted in Figure 3.29 and the presupernova compactness is given in Table 3.2. The three plots are of $\xi_{2.5}$ for the three core CBM cases. In these three cases the CBM in the metal burning convection zones changes the value of $\xi_{2.5}$ significantly. For the C-core simulations the value of $\xi_{2.5}$ ranges from $(0.17, 0.32)$. For the `C1`, `C2` and `C3` simulations, an increase in the value of f_{CBM} corresponds to an increase in $\xi_{2.5}$. The `TEMPLATE` simulation does not share this pattern as it is closer to the value given by the `C2` simulation. The `ONe` simulations show more nonlinearity than that in the `C` simulations. The values of $\xi_{2.5}$ range from $(0.15, 0.27)$ with the `TEMPLATE` simulation being the highest and the `ONe3` simulation being the lowest. In this case, the `ONe1` and `ONe3` simulations have similar values, with $\xi_{2.5} = 0.16$ for the `ONe1` simulation, while the `ONe2` simulation has a value closer to the `TEMPLATE` at $\xi_{2.5} = 0.25$. The ONe-core mass shows a similar trend in that the values of the ONe-core mass of the `ONe1` and `ONe3` simulations at $log(t^*) \approx -6$ are closer than the `TEMPLATE` and `ONe2` simulations (Figure 3.23). The ONe-core masses of the `ONe1` and `ONe3` simulations are both $2.03\mathrm{M}_{\odot}$ whereas the ONe-core masses for the `TEMPLATE` and `ONe2` simulations are $2.33\mathrm{M}_{\odot}$ and $2.21\mathrm{M}_{\odot}$ respectively. For the `Si` simulations, as the CBM increases, $\xi_{2.5}$ decreases, spanning a range of $(0.12, 0.27)$

(Table 3.2). The ONe-core mass for these simulations is plotted in Figure 3.28. As the CBM increases, the dredge-ups of the C-shell overlying the Si burning core deepen in mass, mixing in more material and decreasing the size of the ONe-core(Figure 3.25, 3.28). The `Si` simulations don't experience the dramatic C-shell formation and recession of the `ONe` simulations, potentially leading to a more predictable evolutionary compactness.

Although changes to the CBM strength effect the value of $\xi_{2.5}$, which spans a range of $0.12 \leq \xi_{2.5} \leq 0.35$, from Sukhbold & Woosley (2014), the ZAMS mass of $25M_{\odot}$ lies at the edge of a bump in the ZAMS mass-$\xi_{2.5}$ relation. The region between these bumps in the mass evolution of $\xi_{2.5}$ have been given the name, *islands of non-explodability* (Sukhbold & Woosley, 2014). Because the ZAMS mass of the star studied here is on the edge of one of these islands of non-explodability, the large variations found in $\xi_{2.5}$ with respect to CBM may be due to changes in the ONe-core mass mimicking a different ZAMS mass.

3.3.5 Production Factors

During a Type II supernova explosion, the supernova remnant in the form of a black hole or neutron star, will rob the star of some of the metals produced near the core, as this material will go into making the remnant rather than be ejected (Fryer, 2009). This means that a significant amount of the material the star produces will not be ejected and used for further star formation. Fryer et al. (2012) gives equations for this *fallback* mass, the amount of mass from the star that will be used to form the remnant. The equations are formulated with respect to two types of explosions, a *rapid* explosion and a *delayed* explosion. The rapid explosion is one that occurs in the first 250ms after the bounce and a delayed explosion is one that happens over a longer time scale (Fryer et al., 2012). The values of the remnant mass are given by

$$M_{\text{delay}} = 1.1 + 0.2e^{\frac{M_{\text{zams}}-11.0}{4.0}} - (2.0 + Z_{\text{s}})e^{0.4(M_{\text{zams}}-26.0)} \tag{3.1}$$

$$M_{\text{rapid}} = M_{\text{delay}} - 1.85 + 0.25Z_{\text{s}} + 10.0(1.0 + Z_{\text{s}})e^{(\frac{M_{\text{zams}}-23.5}{1.0+Z_{\text{s}}})^2} \tag{3.2}$$

Here, M_{zams} is the ZAMS mass and for Equation 3.2 is $\geq 22M_{\odot}$, Z_{s} is the metallically with respect to solar, M_{delay} in the delayed explosion remnant mass and M_{rapid} is the rapid explosion remnant mass.

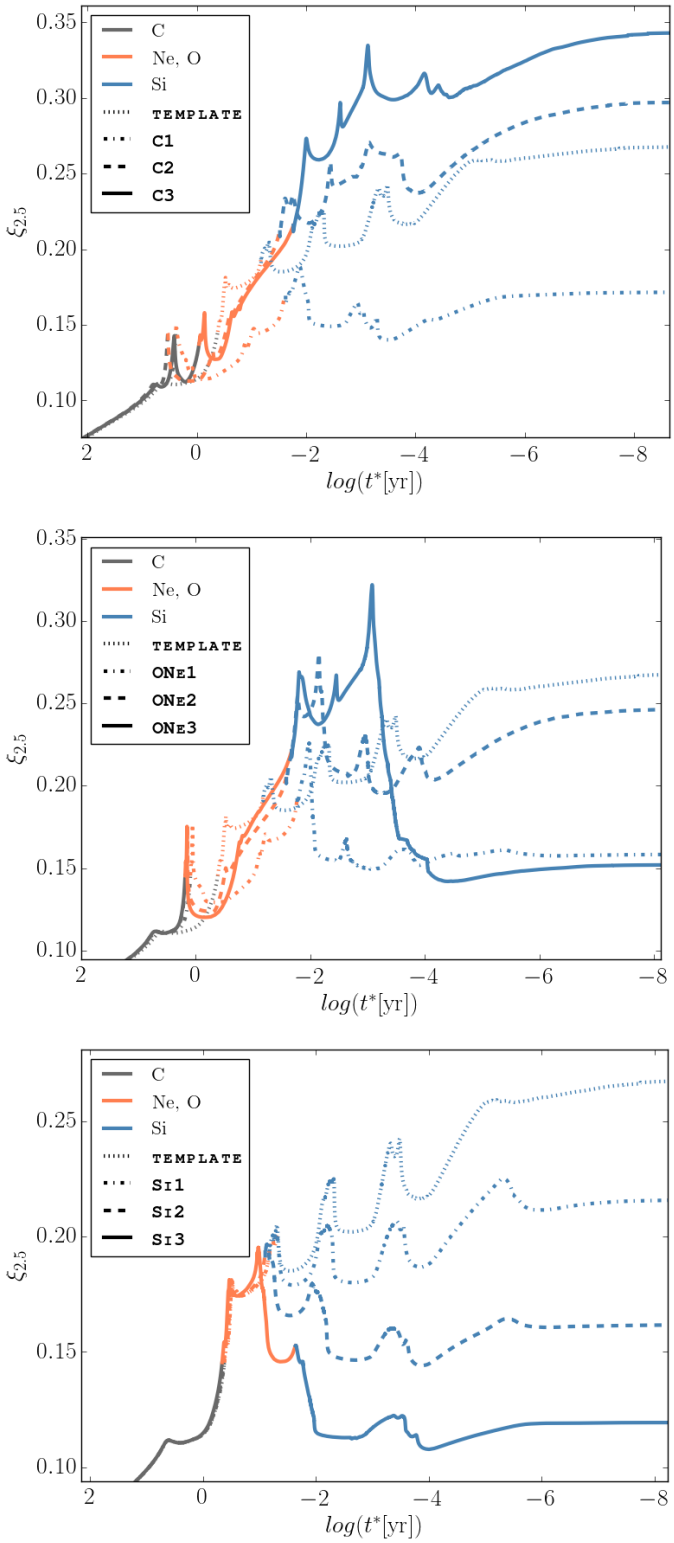

Figure 3.29: Evolutionary compactness for the three sets of simulations. The x-axis in given in log of the time left until collapse. The colours of the line represents the core burning stage where grey is C-core burning, orange is Ne and O-core burning and blue is Si-core burning. Each set of simulations diverges from the template soon after the enhanced CBM is implemented. Differences in the evolutionary compactness before this are due to differences in the age of the simulations.

For the $25M_\odot$ model with metallicity of $Z = 0.02$ used in this work, $M_{\rm delay} = 5.7M_\odot$ and $M_{\rm rapid} = 15.5M_\odot$. The value for $M_{\rm rapid}$ is greater than the mass of the star at collapse (Figure 3.31), implying that the material from the envelop that has be ejected by winds will be the only material used to enrich subsequent star formation. If the remnant mass of the simulations considered here can be described by $M_{\rm delay}$, because this fallback mass is near the top of the C-shell, then material processed by the metal burning regions of the star can be brought up to the top of the C-shell through dredge-ups and shell mergers.

One way to examine the effects of enhanced CBM on the final state the star is to look at the production factors of the mass ejected by the explosion. Figure 3.30 gives the production factors of the C, ONe and Si simulation sets. The greatest deviation from the TEMPLATE simulation is found in the C simulations. In the C set, the amount of C is not significantly different from the initial solar abundance, whereas the TEMPLATE simulation is enhanced by a factor of 10. Ne, Mg and Si also show large nonlinear variation due to the complexity of the Ne and C-shell interactions (Section 3.3.1). The C3 simulation produces the least amount of Ne whereas the C1 simulation produces the most, with a variation of about one order of magnitude. Simulations with the lowest Ne production (C2 and C3) produce the most Mg and Si where simulations with high Ne (TEMPLATE and C1) produce lower amounts. This implies that in the C2 and C3 cases the abundances in the C-shell shows evidence of Ne burning from below. For the ONe simulation set, the TEMPLATE, ONe1 and ONe2 simulations all show similar trends in the production factor. C decreases for enhanced $f_{\rm CBM}$ and Ne, Mg and Si all increase, in part due to the depth of the third C-shell (Section 3.3.2). The ONe3 simulation does not follow this trend. The production factor for Ne is less than that for the TEMPLATE, and Mg and Si are both higher. Si in particular is more than an order of magnitude larger than that from the TEMPLATE with a value of $P_f = 13.4$, compared to $P_f = 1.1$ for the TEMPLATE. The production factor for the Si simulations have the least deviation from the TEMPLATE. Figure 3.30 shows that the production factor for C decreases for increasing values of $f_{\rm CBM}$, whereas Ne and Ne ash both increase. Unlike the ONe simulations, the Si simulations don't show large dredge-ups of Ne ash into the C-shell (Figure 3.19, 3.25). In the Si1, Si2 and Si3 simulations, only a limited amount of mixing between the C-shell and the underlying Ne-shell is possible due to the large entropy gradients found between the shells (see Section 3.3.3, Figure 3.27). In these simulations, the production factor for C shows the largest variation from that of the TEMPLATE. During

core Si burning, Ne and O-shells form under the C-shell and promote C-shell dredge-ups (Figure 3.25). This decreases the ONe-core mass and the depth of the C-shell boundary (Figure 3.28), increasing the temperature at the bottom of the C-shell.

The CBM during the later stage evolution of these simulations can affect the production factor by mixing material processed in metal burning shells into the C-shell. Simulations that show large deviations from the `TEMPLATE` are those that have dredge-ups and shell mergers with the C-shell, and have enough time left in their evolution to mix that material passed the fallback mass.

3.4 Summary

In the `C` simulations (Section 3.3.1), enhenced CBM decreases the lifetime of the first C-shell and mixes more ash from below. The ash distribution mixed up by the first C-shell defines the starting point for the second C-shell. Enhanced CBM can push the bottom convective boundary deeper in mass into the ONe-core, burning C deeper in the star and mixing up C ash. During Ne, O and Si-core burning, enhanced CBM interacts with the C, Ne and O-shells by promoting dredge-ups and shell mergers. These mixing events can transport Ne ash found under the C-shells to the tops of these C-shells, provided there is sufficient time to do so.

When enhanced CBM is implemented during core Ne and O burning as in the `C` and `ONe` simulations, the interaction of the C and Ne-shells dredge Ne ash into the convective C-shells where it can be transported further out in mass (Section 3.3.1, 3.3.2). During this stage of evolution, the C-shell of the `TEMPLATE` simulation does not experience significant dredge-ups or shell mergers with the underlying material. Simulations with enhanced CBM have a number of C-shells that develop during this time (Figure 3.10, 3.19). During the growth of a new convective C-shell, dredge-ups can mix Ne ash from radiative Ne burning into the C-shell. In the `C3` simulation, with a large value of $f_{\rm CBM}$, a convective Ne-shell merges with the newly formed C-shell. Because these mixing events happen around 3.5 days before the end of the simulation, the material can be mixed throughout the C-shell before collapse, as the convective turn over time scale of the C-shell is $\approx$ 5hr.

The `Si` simulations show the interactions of the C, Ne, O and Si convective shells that develop late in the lifetime of the simulations (Section 3.3.3). Despite the close proximity of the shell formation, the entropy gradients between the C and O-shells that form inhibit shell mergers at times grater then $\approx$ 5hr until collapse. Because 5hr

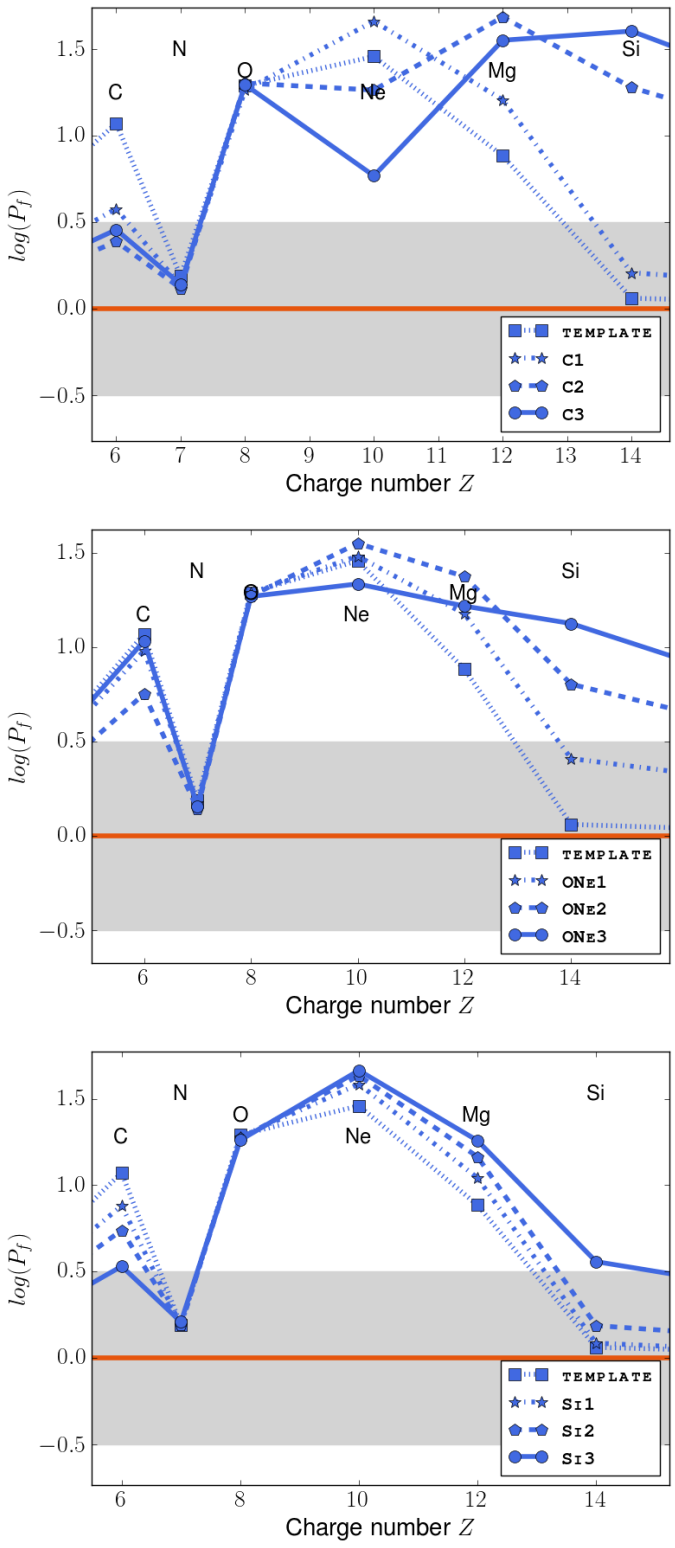

Figure 3.30: Production factors relative to the initial solar abundance for the `C`, `ONe` and `Si` simulations. The orange line represents no change in the abundance of the element and the grey shaded area represents an uncertainty in the solar abundance used in the simulations.

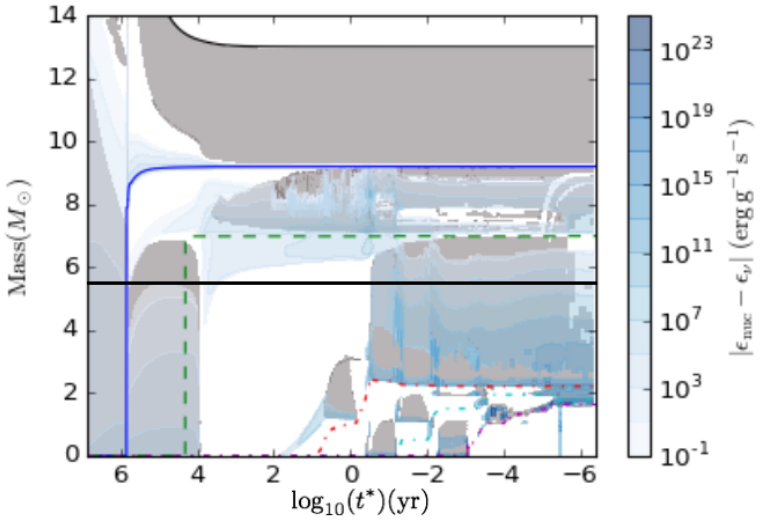

Figure 3.31: Kippenhahn diagram for the `S1` simulation. The solid black line is the delayed fallback mass cut, $M_{\rm delay} = 5.7{\rm M}_\odot$, given by Fryer et al. (2012). The mass of the star at collapse is less than the value of the rapid fallback mass, $M_{\rm rapid} = 15.5{\rm M}_\odot$.

is the convective turnover time scale of the C-shell during the end of the simulation, material mixed in by any dredge-ups or shell mergers that happen after this will not be ejected by the supernova explosion. This is because the fallback radius given by Fryer et al. (2012) of $M_{\rm delay} = 5.7{\rm M}_\odot$ sits near the top of the convective C-shell.

The evolutionary compactness of each simulation is dependent on the strength of the CBM (Section 3.3.4). The values $\xi_{2.5}$ range from 0.12 to 0.35 when taken at $log(t^*) = -6$. Simulations which experience enhanced CBM during the Ne and O-core burning stages (`C` and `ONe`) are largely non-monotonic whereas enhanced CBM in the `Si` simulations produce a lower value for $\xi_{2.5}$ with increasing values of $f_{\rm CBM}$. This means that in these simulations, the non-monotonicity in $\xi_{2.5}$ primarily comes from the C, Ne and O-core and shell interactions during those core burning stages but not during the end of Si and Fe-core burning.

Using the fallback prescription given by Fryer et al. (2012), the production factors from these simulations show large variations in C, Ne, Mg and Si (Section 3.3.5). As with the evolutionary compactness, largest deviations from the `TEMPLATE` occur in simulations that experience enhanced CBM during C, Ne and O-core burning. During these stages of evolution, enhanced CBM promotes dredge-ups of Ne ash into the C-shells where the ash can be mixed to the top of that shell. The delayed fallback mass given by Fryer et al. (2012) is $M_{\rm delay} = 5.7{\rm M}_\odot$ which lies under the upper convective

boundary of the C-shell. Because the these mixing events happen relatively early in the metal burning core evolution of the simulations, the Ne ash has time to mix across the C convective shell and surpass the fallback radius. The production factors of the `Si` simulations show relatively smaller deviations due to the lack of strong mixing events. Limited mixing is found later in the `Si` simulations between the C and O-shells although the entropy gradients between the convective shells are too large to lead to significant mixing.

3.5 Discussion

CBM during the time when a large C-shell has developed near collapse can change the amount of metals ejected during the supernova (Section 3.3.5). If the fallback can be modeled as a delayed supernova with a fallback mass of $M_{\rm delay} = 5.7{\rm M}_{\odot}$, then material mixed into the C-shell can be ejected provided it has enough time to be mixed to the top. With a convective turnover time scale of $\approx$ 5hr during Si-shell burning, a large increase in luminosity is needed to decrease the convective turnover time scale of the C-shell to a value less then the time left untill collapse. Dynamic events such as dredge-ups and shell mergers in the late time of evolution could potentially provide the luminosity, but these are not seen in the simulations. Although the `Si` simulations have tightly packed convective shells (Figure 3.22), they do not merge due to the large entropy gradients, and changes in the production factor are caused by the dredge-ups found earlier in the evolution (Section 3.3.5). Variations to the fallback mass on the order of a few solar masses would also not have a large effect on the production factors. The fallback mass is $\approx 1.5{\rm M}_{\odot}$ from the top of the C-shell and $\approx 3.5{\rm M}_{\odot}$ from the bottom. If the fallback mass varies within this mass range, material from below will still need to be mixed into the C-shell to be ejected.

Although the evolutionary compactness in the `Si` simulations decreases with increasing $f_{\rm CBM}$, the trends found in the `C` and `ONe` sets show non-linear behavior with respect to $f_{\rm CBM}$. As Sukhbold & Woosley (2014) found, the non-linear behavior of $\xi_{2.5}$ with respect to ZAMS mass is due to the interaction of the C and O burning shells. Both the `C` and `ONe` sets diverge from the `TEMPLATE` significantly during C and O burning, creating different numbers of C-shells as well as experiencing dredge-ups and shell mergers that change the ONe-core mass. The ONe-core mass of the `Si` simulations decrease with increasing CBM and do not show the non-linear deviation for the `TEMPLATE`. During the late stages of evolution in the `Si` simulations, the main

effect of the CBM is to decrease the C-shell boundary. Because this boundary is below $2.5M_{\odot}$ the values of $\xi_{2.5}$ represent the amount of material that is in the C-shell rather than any intricate shell interactions. This means that the variation found in $\xi_{2.5}$ is due to the interaction of the C, Ne and O convective regions during those core burning stages whereas during Si and Fe-core, the shell structure has little effect.

The variation in $\xi_{2.5}$ of $\Delta\xi_{2.5} = 0.23$ is due to two simulations with the highest values of $f_{\rm CBM}$(`Si3` and `C3`). If only the simulations implementing $f_{\rm CBM}$ values of 0.012 and 0.022 are considered, the variation in $\xi_{2.5}$ decreases but the non-linearity found in the evolutionary compactness is still present. This means that the impact of CBM on the compactness is a cumulative effect of convective shell interactions and is not just limited to the cases where large amounts of mixing change the structure.

Chapter 4

Summary, Conclusion and Further Work

"Let it be emphasized again, however, that users of this [mixing length] theory should be well aware of the possible quantitive unreliability of results obtained by its use." Cox et al. (1968)

4.1 Summary

The CBM model parameter $f_{\rm CBM}$ in the advanced stages of massive star evolution is unknown for the majority of convection zones. Massive star simulations with different CBM strengths show drastic differences in the internal CO-core structure during the advanced stages of evolution. The CBM of the convective cores and shells that emerge during this time have a direct impact on the presupernova structure and explodability of these models. The complex interaction of the convective C-shells and Ne burning regions have an influence on what will be ejected during the supernova explosion and possibly provide indirect observational evidence of the mixing mechanisms between these shells. The work described in Chapter 3 and summarized here does not answer the question of what the value of $f_{\rm CBM}$ should be, but rather attempts to better define the problem by emphasizing the dependence of massive star models on CBM strength.

MESA simulation core structure

The simulations presented in Chapter 3 show a large deviation from the `TEMPLATE` simulation in the structure with respect to the values of $f_{\rm CBM}$ of $(0.002, 0.012, 0.022, 0.032)$. Although artificially varying the strength of the CBM in the MESA simulations does not model the natural CBM that may be found in a star, mixing across convective boundaries has been shown to drastically change the advanced metal burning core of the $25 M_\odot$ model. Through the dredge-up mechanism, convective C-shell boundaries decrease in mass and are able to entrain Ne ash from previous radiative Ne burning events. Provided the star has enough time left in its evolution before it collapses, the Ne ash can be transported to the top of the convective C-shell. Because the material is transported further out of the star, it is possible for it to be ejected in the supernova explosion. The shell merger found between the C and Ne-shells in the `C3` simulation has the same effect in transporting material further out of the star, although the shell mergers found later in the evolution in the `Si` simulations have little effect on the composition of the C-shell. This is because the entropy gradients at the bottom of the C-shell are too steep for the material to mix.

Compactness

Varying the strength of CBM in the massive star models of Chapter 3 produces significant, non-linear differences in the values of the presupernova compactness, $\xi_{2.5}$. Sukhbold & Woosley (2014) found a range of $0.16 \lesssim \xi_{2.5} \lesssim 0.43$ for simulations run at $Z = 0.02$, over the mass range of $23 M_\odot$ to $26 M_\odot$ (Section 3.5). The values given by Sukhbold & Woosley (2014) represent the height of $\xi_{2.5}$ on the edge of the island of non-explodability found near $25 M_\odot$ and shows the non-monotonic dependence of $\xi_{2.5}$ with respect to ZAMS mass. The values of $\xi_{2.5}$ found by varying the strength of the CBM during the metal burning convective zones in the work presented here are $0.12 \leq \xi_{2.5} \leq 0.35$ (Section 3.3.4). Because the range of values of $\xi_{2.5}$ are on the order of those found by Sukhbold & Woosley (2014), the strength of CBM during the advanced stages of evolution is a significant factor in determining whether or not a massive star simulation will explode.

Although Sukhbold & Woosley (2014) found that $\xi_{2.5}$ is sensitive to the C-free core mass, they did not determine what mechanism caused this in detail. The CBM simulations in Section 3.3.4 show relatively large non-monotonic deviations from the `TEMPLATE` model during C, Ne and O-core and shell burning. During these burning

events, the C-shells experience large dredge-ups of Ne ash from below, dropping the C free core boundary in mass. These C-shells can also recede as convection stops, increasing the C free core boundary. The `ONe3` simulation experiences a C-shell recession during which time the evolutionary compactness increases (Section 3.3.2). When enhanced CBM is implemented during Si-core burning in the `Si` simulations, the resulting values of $\xi_{2.5}$ decrease with increasing $f_{\rm CBM}$. The non-monotonicity seen in the `C` and `ONe` simulations is not seen in this set. In this case, the largest structural difference found in these models is the mass of the C free core after the convective C-shell experiences a dredge-up during the core contraction just before Si-core burning (Section 3.3.3). After the dredge-up, the C free core mass is less for higher values of $f_{\rm CBM}$. The O free and Fe-core masses roughly show this trend as well in regions where the boundaries are approximately constant in time. One possible reason for the monotonicity found in the `Si` simulations could be because the C free core masses are less than the $2.5 M_{\odot}$, the characteristic remnant mass used in $\xi_{2.5}$ by O'Connor & Ott (2011). As the C free core mass drops, more material is pulled into the less tightly bound C-shell. This increases the radius enclosing $2.5 M_{\odot}$ and decreases $\xi_{2.5}$.

Changing the characteristic remnant mass ($2.5 M_{\odot}$) used to calculate $\xi_{2.5}$ would not eliminate the variation found in the MESA simulations. Decreasing the characteristic remnant mass would push this boundary closer to the O free or Fe-core boundaries, which show more variation during Si and Fe-core burning than the C-shell. If the characteristic remnant mass were increased, the relatively large amount of mass contained in the C-shell would begin to overpower the contribution from the core. The compactness would end up being dependent on the strength of the burning in the C-shell where higher C burning luminosity would push the upper convective C boundary further out to maintain hydrostatic equilibrium, increasing the radius containing the characteristic remnant mass and decreasing the compactness. Because the variation of $\xi_{2.5}$ is on the order of that found by Sukhbold & Woosley (2014) and shows non-linear variation during the advanced metal burning convection zones, the strength of CBM is a significant influence on the value and behaviour of $\xi_{2.5}$.

Sukhbold & Woosley (2014) states that for high $\xi_{2.5}$, the model should be harder to explode by any mechanism due to the low gravitational potential of the material in the core. Despite the correlation that has been found in $\xi_{2.5}$ with respect to the explodability of massive stars, the mechanisms present in the supernova explosion involve intricate interactions between physical mechanisums that are inherently 3D. Many of these physical mechanisms are either poorly modelled, unknown or not

included in the 1D models that the $\xi_{2.5}$ results are based off of.

Production Factor

If the massive star models were to explode, the structure and dynamics of the metal burning shells determine the composition of material that would be ejected by the supernova explosion. If the remnant mass can be given by the delayed fallback mass of $M_{\rm delay} = 5.7 M_\odot$ (Fryer et al. (2012), Section 3.3.5), then the MESA simulation of Section 3.2 will eject the material that does not form the remnant. Structurally, the material that will be ejected is all material lying just inside of the top of the convective C-shell (Figure 3.31). Because the C-shells are convective in the simulations, any material entrained into them from below will be mixed throughout the shell and brought to the top where it can be ejected, provided it has the time to do so. As with the compactness, the largest variation from the `TEMPLATE` simulation is found in simulations that implement enhanced CBM through C, Ne and O-core burning. These are the `C` and `ONe` simulations. Because the timing and position of the C, Ne and O-shells change with different values of $f_{\rm CBM}$, dredge-ups and shell mergers are possible at different locations in the simulations. Dredge-ups of Ne burning ash into the C-shell are present in both the `C` and `ONe` simulations with enhanced CBM but not in the `TEMPLATE` as the bottom of the C-shell remains roughly constant in mass throughout the evolution (Section 3.3.1, 3.3.2). The `C2` and `C3` show the increase in Mg and Si as Ne decreases, producing $log(P_f) \approx 1.5$ for both Mg and Si, whereas the `TEMPLATE` and the `C1` simulations don't significantly enhance these values above the initial composition. Although `C2` and `C3` have similar trends in the production factor, they mix Ne ash into the C-shell in different ways. The `C2` simulation has a C-shell dredge-up at the end of O-core burning which entrains the Ne ash from radiative Ne burning. In the `C3` simulation, as the third C-shell forms, radiative Ne burning begins below it. This radiative Ne burning transitions into convection and begins to entrain material from above and below until the C and Ne-shells merge (Section 3.3.1). Despite these mechanisms producing similar production factors in the MESA simulations, these are two different nucleosynthetic sites. The dredge-up is a gradual entrainment of material into a convective environment whereas the merger could be a highly dynamic mixing event that quickly transport species to regions of higher temperature. The `ONe` show less variation then the `C` simulations although the non-linearity with enhanced CBM is still present. In the `ONe3` simulation, the

dredge-up in the fourth C-shell is deep enough to reach O burning ash from the second O-shell, whereas the `ONe1` and `ONe2` only dredge-up Ne ash. The large variation from the `TEMPLATE` simulations is seen in the `C` and `ONe` simulations because of the interaction of the C, Ne and O-shells. When the C-shells recede, the C free core boundary increases in mass, Ne burning can occur at a higher mass and the enhanced CBM can dredge-up the frozen in compositions left behind. In the `Si` simulations, the C-shell has its last dredge-up at the end of the second O-shell. Because the interactions of the Ne and O-shells before this time are similar, the dredge-ups act to mix different amounts of the same material into the C-shell. This produces the monotonic behaviour of the production factor with respect to CBM strength seen in the `Si` simulations. Despite the lack of dredge-ups of the C-shell into Ne ash in the `Si` simulations, in the `Si1`, `Si2` and `Si3` simulations, O-shells form in close proximity to the bottom convective boundary of the C-shell (Section 3.3.3, 3.4). Although some material is transported across the boundary between them, these shells don't merge due to the high entropy gradients found there.

The production factor assumes that material outside of $M_{\rm delay} = 5.7{\rm M}_{\odot}$ is the material that will be ejected by the supernova. Below $5.7{\rm M}_{\odot}$, entropy and composition gradients can exist between the metal burning shells. Specifically, the entropy gradient at the bottom of the C-shell in the `Si3` simulation is $\approx 3/N_{\rm A}kerg$. Fluid instabilities durning the explosion such as Richtmyer-Meshkov instabilities act to mix material across a density gradient perpendicular to the direction of a propagating shock. If the proto-neutron star mass is less than the bottom of the C-shell, a shock could be launched that propagates through the shell structure underlying the C-shell. If the shock is strong enough and the composition gradients large enough, Richtmyer-Meshkov instabilities could develop on the boundaries and may be able to mix material from the stellar core out to the top of the C-shell on a time scale much faster than the convective turn over time scale. In this case, more of the metal content of the core will be mixed up and ejected.

The fallback mass from Fryer et al. (2012) used with the models as stated above, although it is not applicable to the MESA stellar evolution simulations presented in this study. The fallback prescription in the form presented by Fryer et al. (2012) is only dependant on the ZAMS mass and metallicity, and gives the type of explosion that would be possible (rapid or delayed). The work on the compactness in Section 3.3.5 shows that the explodability is dependant on the core structure and not just these two parameters. Despite this and because of the lack of a general method

for finding the remnant mass, the fallback mass given by the delayed explosion shows that it may be possible for the mass cut to appear somewhere in the C-shell. This means that if the delayed fallback mass is within a few solar masses of the remnant mass, the fallback mass will still be in the C-shell and still show the Ne ash enhancement, depending on the amount of time left in the stars life. If the fallback mass is above the C-shell, none of the material produced in the core can escape, except for in the shock driven mixing case stated above. The production factor would only show abundance signatures from H and He burning. If the fallback mass was less than the mass enclosed by the bottom of the C-shell, then the composition of the ejected material would change depending on the Ne, O and Si-shell structure at collapse.

4.2 Conclusion

The f_{CBM} value determined from the PPMstar simulation of the O-shell of a $25\mathrm{M}_{\odot}$ 3D model was found to be $f_{\mathrm{CBM}} = 0.03$ which was determined by solving the inverse diffusion equation with fractional volume profiles separated by a given time (Chapter 2). Although the diffusion coefficient showed noise in the centre of the convection zone from numerical instabilities, the boundaries were unaffected, producing a relatively smooth diffusion coefficient profile that fit the exponentially decaying CBM model remarkably well.

The simulations calculated using MESA spanned a range of f_{CBM} values of $(0.002, 0.012, 0.022, 0.032)$. When the enhanced CBM was applied to the C, Ne and O burning cores, the simulations showed dredge-ups and shell mergers between the C and Ne-shells producing Ne ash signatures in the production factors. The compactness values from the presupernova core were found in the range of $0.12 \leq \xi_{2.5} \leq 0.35$ which are significant when compared to the range of values found around the island of non-explodability given by Sukhbold & Woosley (2014) of approximatly $0.16 \lesssim \xi_{2.5} \lesssim 0.43$. The simulations show a non-monotonic variation in $\xi_{2.5}$ with respect to f_{CBM} when enhanced CBM is applied to C, Ne and O-core burning. When applied to Si-core burning, the enhanced CBM acts to decrease the bottom boundary of the C-shell, leading to a decrease in $\xi_{2.5}$. The enhanced CBM in the C, Ne and O burning cores promote dredge-ups that change the values of $\xi_{2.5}$ and lead to the non-monotonic behaviour. This evidence leads to the conclusion that CBM between C, Ne and O convection zones changes the explodability of the stellar model non-monotonically.

4.3 Further Work

No direct observations of the interior of stars can be made. Because of the importance of knowing the dynamics of the convection in the cores, simulations must be preformed. In Chapter 2, the PPMSTAR code was used to simulate the O-shell in a $25M_{\odot}$ model and a f_{CBM} value was found for the upper convective boundary. This was then used in the 1D MESA stellar evolution simulations (Chapter 3). But, because observations of these convection zones are not possible, the 3D codes that compute the convection are not validated.

The measurement of f_{CBM} is dependent on the amount of material that can mix through the convective boundary. This CBM is driven by the turbulent variable composition mixing at the boundary. If the codes used to simulate the turbulent convection within the stellar interior cannot model turbulence properly, then the model parameters measured from them will not be accurate and results generated from the informed 1D codes will not be useful. Because the convection is highly turbulent and the dynamics can be scaled along the inertial subrange, it is possible to compare the idealized code turbulence with turbulent variable density laboratory flows. The turbulent mixing tunnel (TMT) experiment, described in Appendix B, provides highly turbulent variable density mixing data over multiple mixing regimes. The data sets generated from this experiment consist of high-resolution local velocity and concentration measurements. This data could be used to compare to the code turbulence in terms of the mixing quantities of the flow.

Validation studies of 3D hydrodynamic codes are important in further improving stellar evolution codes. Because observations of these locations are impossible, high-resolution experimental data sets provide the best opportunity for the validation of the highly turbulent mixing found in stellar convection.

Appendix A

List of Varaibles

a	Radiation density constant
c	Speed of light
c_p	Specific heat
D_0	Diffusion coefficient (Equation 1.25)
$D_{\rm CBM}$	Exponentially decayed diffusion coefficient (Equation 1.25)
E_n	Nuclear energy from core burning (Equation 1.1)
$f_{\rm CBM}$	CBM efficiency parameter (Equation 1.25)
f_0	CBM boundary shift parameter
G	Gravitational constant
H_P	Pressure scale height
L	Luminosity
L_i	Luminosity due to the burning of i
$m,\ M$	Mass
P	Pressure
r, R	Radius
Re	Reynolds number, $Re = vl/\nu$
S	Entropy
T	Temperature
t	Time
t^*	Time left till core collapse
$t^{@}$	Time left till some evolutionary phase
z	Distance to the convective boundary (Equation 1.25)
$\alpha_{\rm MLT}$	Mixing length free parameter
α	Simi-convective mixing length free parameter

ϵ	Energy per unit time per unit mass
μ	Mean molecular weight
ν	Kinematic viscosity
$\xi_{2.5}$	Compactness (Equation 1.26)
ρ	Density
$\tau_{\rm n}$	Nuclear time scale (Equation 1.1)
$\tau_{\rm ther}$	Thermal time scale (Equation 1.2)
$\tau_{\rm dyn}$	Dynamic time scale (Equation 1.4)
$\tau_{\rm conv}$	Convective turn over time scale (Equation 1.5)
$\rm R_\odot$	Solar radius
$\rm M_\odot$	Solar mass
$\rm L_\odot$	Solar luminosity

Appendix B

The Turbulent Mixing Tunnel Experiment

B.1 Introduction

Turbulent mixing can strongly affect the evolution and structure of a variety of fluid flows throughout the universe. Thunder cloud formation and dissipation, chemical combustion (Pitsch, 2015) and boundary induced tidal mixing, such as that found off the south coast of Vancouver island (Cushman-Roisin & Becjers, 2008), are strongly influenced by turbulence that develops within the flows.

Convection can develop in regions around the proto-neutron star in core collapse supernovae (Fryer & Young, 2007). The convection found in the layers inside of stars can have large impacts on the stellar structure as well as causing violent dynamical flows (Herwig et al., 2014). Although these flows range from terrestrial to astronomical and span a large range of characteristic length and time scales, one commonality between them is their dependence on turbulent, variable density mixing. Because direct quantitative observation of these flows is, for the most part, impossible, it is left to construct physical models and perform simulations. Unfortunately, due to the strong turbulence that develops, the dynamic range of these simulations are not large enough to capture the large scale motions, while simultaneously rendering the smaller turbulent length scales. Capturing these small scales is important, specifically in variable density turbulence, because these are the scales at which kinetic energy is dissipated. This small scale turbulence determines the mixing rates and inevitably provides the mechanism that feeds back into the large-scale dynamics. Although sub-

grid models exist in order to try and capture the dissipative affects at these small scales, these models need to be validated against experimental data to ensure they can produce physically relevant results. Reliance on unvalidated subgrid models creates the potential for large misunderstandings in the physics of the flows stated above. In order to simulate these turbulent flows in a manner that is consistent with reality, it is critical to quantitatively understand the small scale dynamics of turbulent variable density mixing.

In order to understand turbulent variable density mixing, it is necessary to investigate the small scale mixing mechanisms present in these flows under a variety of flow conditions. The turbulent variable density jet found with in the turbulent mixing tunnel experiment (Gerashchenko & Prestridge, 2015) provides such an environment (Figure B.1). The experiment consists of a high density jet within a co-flowing lighter fluid, that experiences momentum and buoyancy dominated flow regimes as well as exhibiting a variety of subsonic flow instabilities. By using techniques designed to measure densities and velocities of the flow under high resolution, it is possible to quantitatively investigate the dynamical properties and small turbulent length scales. With data of such high quality it will then be possible to characterize the flow in terms of relevant dimensionless quantities and investigate the dissipation effects at length scales smaller then the Taylor micro scale. The varying levels of turbulence at different length scales can also be determined within these flow regimes. The results of this study will provide a solid foundation for the validation of simulated turbulence as well as furthering the understanding of turbulence theory.

B.2 Background

In order to investigate the mechanisms that are involved in any turbulent mixing process, it is necessary to look at the length scales involved in such an event. Consider an 'eddy' to be a turbulent motion contained in a region of characteristic length, l, that is somewhat coherent over that region (Pope, 2003). The idea of the energy cascade is that, for sufficiently high Reynolds number (Re), the large eddies that make up the large scale flow are unstable and break up forming smaller eddies, which are themselves unstable (Pope, 2003). This process continues until the length scale is small enough for the viscosity to effectively be able to dissipate the kinetic energy of the fluid motion (Pope, 2003). Kolmogorov's second similarity hypothesis divides these length scales into three ranges (Section B.5). The energy containing range consists of

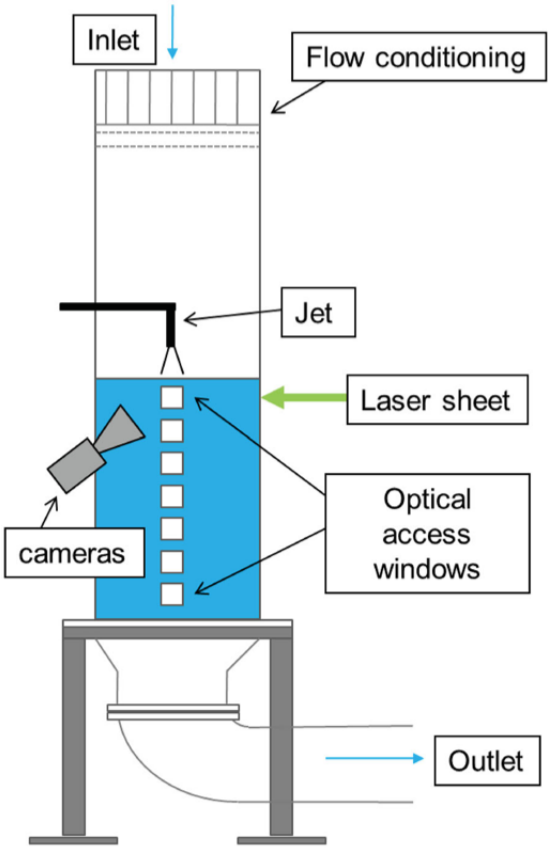

Figure B.1: Diagram of the experimental apparatus. The flow conditioner at the top of the tunnel reduces perturbations in the inflowing air before it passes the jet. Laser sheets illuminate the flow at a specific optical access window where cameras are positioned in order to image the flow. The fan that pulls air through the tunnel is positioned passed the outlet region labelled in the figure. Diagram is from Gerashchenko & Prestridge (2015)

the large scale motions which contain the majority of the kinetic energy of the flow. The Universal range is divided into two subranges, the Inertial subrange, dominated by inertial effects, and the Dissipation range, dominated by viscous effects (Pope, 2003). The Kolmogorov hypothesis assumes that the turbulence is homogeneous and isotropic (Section B.5), although, in reality, the turbulent length scales found in a flow may not be uniformly decreasing from the large eddy length scale (l_0) down to the Kolmogorov length scale (η). Within some length scale range, a flow with this characteristic will violate the homogeneity and isotropic assumptions needed for the Kolmegorov hypothesis. Convective plumes such as the ones described above can exhibit this characteristic as the large scale convective motions are not homogenous.

The down drafts and up drafts can exhibit some homogeneity but on a length scale much smaller then l_0. This has the direct effect of changing the amount of energy that can be dissipated by turbulence from large to small scales, violating some of the assumptions used in subgrid turbulence models.

Although the Kolmogorov length scales are important for a fundamental understanding of turbulence, experimentally they are difficult to determine. The Taylor micro-scale is defined as

$$\lambda_h(t) = [-\frac{1}{2}h''(0,t)]^{-\frac{1}{2}}$$

where $h(x,t)$ is either the longitudinal or transverse autocorrelation functions denoted by $f(x,t)$ and $g(x,t)$ respectively (Pope, 2003). These autocorrelation functions can be expressed in terms of the two point correlation, R_{ij} as

$$f(r,t) = \frac{R_{11}}{u'^2} = \frac{< u_1(\vec{x} + r\vec{e_1}, t)u_1(\vec{x}, t) >}{< u_1^2 >}$$

$$g(r,t) = \frac{R_{22}}{u'^2} = \frac{< u_2(\vec{x} + r\vec{e_1}, t)u_2(\vec{x}, t) >}{< u_2^2 >}$$

where $\vec{r}$ is a separation vector between two points $\vec{x_1}$ and $\vec{x_2}$, $u_1(\vec{x},t)$ and $u_2(\vec{x},t)$ are the longitudinal and transverse components of velocity at a point $\vec{x}$ and time t, u' is the root-mean square (r.m.s.) velocity and the angled brackets denote a mean (Pope, 2003). As with the Kolmogorov hypothesis, the Taylor micro-scale assumes homogeneous isotropic turbulence. A derivation of these quantities can be found in Pope (2003). Although the Taylor micro-scale doesn't have an explicit physical meaning, it is a small turbulent length scale that can be found within the inertial subrange. The Taylor micro-scale can be determined experimentally with an experiment of high enough resolution.

As well as determining the length scales of the small scale turbulent motions, because the experimental flow consists of inertial and buoyancy dominated regimes, it is important to examine the relevant dimensionless numbers. One of these numbers is the Atwood number, given by

$$A = \frac{\rho_1 - \rho_2}{\rho_1 + \rho_2}$$

where ρ_i are densities and ρ_2 is the density of the lighter fluid such that the Atwood number is always positive. The Atwood number gives a measure of the reduced density

difference between two fluids and can be helpful in scaling and stability calculations. A local version of the Atwood number can also be defined as

$$A_l = \frac{< \rho'^2 >}{< \rho >^2}$$

here, the prime denotes the variance of the density. This form gives an idea of local density variations with respect to the surroundings. Another dimensionless number related to the stability of the flow is the Richardson number, given by

$$Ri = \frac{g}{\rho} \frac{\nabla \rho}{(\nabla u)^2}$$

where g is the acceleration due to gravity. The Richardson number is a measure of the buoyancy effects over the shearing at a boundary. The Schmidt number is given by

$$Sc = \frac{\nu}{D}$$

and is a measure of the viscous diffusivity over the mass diffusivity where ν is the kinematic viscosity and D is the mass diffusivity. For turbulence, the Schmidt number characterizes the relative importance of the turbulent momentum transfer to the turbulent mass transfer. The Mach number is given by

$$Ma = \frac{u}{c}$$

where c is the sound speed of the fluids. Although the experiment is subsonic with $Ma < 0.6$, the sound speed will change depending on the mixture of the fluids, increasing as an inverse square for higher densities. The bulk Reynolds number is a measure of the momentum effects over the viscous effects and is given by

$$Re = \frac{ul}{\nu}$$

where u is a characteristic velocity and l a characteristic length scale. Because a turbulent flow evolves through a variate of length and time scales from the energy containing region down to the viscus subregion, the bulk Reynolds number alone is not sufficient in characterizing the flow. As the length scale decreases, so does the Reynolds number until it becomes unity at the Kolmegorov length scale. Reynolds numbers at these small scales are called turbulent Reynolds numbers. One of these

turbulent Reynolds numbers is defined in terms of the Taylor microscale and is given by

$$Re_T = \frac{u'\lambda_{h(t)}}{\nu}$$

where $\lambda_{h(t)}$ is the Taylor microscale and u' is the r.m.s. of the velocity fluctuations in the turbulent region. By comparing the dimensionless numbers of the flow, it will be possible to determine a variety of dynamical regimes, such as buoyancy or inertial dominance. The results of the turbulence study performed in these regimes can then be applied to other dimensionally similar flows.

To determine the length scales described above it is necessary to determine the velocity of the flow. One method of doing this is called particle image velocimetry (PIV). The PIV technique involves seeding the flow with tracer particles and imaging the flow with a camera twice per velocity measurement. The tracer particles are illuminated with a sheet of laser light in order to visualize them. The time difference between the images is kept small enough so that individual tracer particles can be identified in both images and a distance can be determined. Because the time difference between the images is known, a local velocity can be calculated. Practically, in order to analyse a large number of images, cross-correlation software is used to track regions of the images with similar tracer particle structure. The result of the PIV technique is a velocity field of the region of the image, which can then be used to determine the bulk flow velocities as well as look at the smaller scale motions.

For the variable density turbulent mixing considered here, it is also necessary to be able to extract density measurements from the flow. A technique called planar laser-induced florescence (PLIF) is used to measure the mixing of the fluids. Acetone vapour will fluoresce when illuminated by light with in the wavelength region 225nm-320nm with emission wavelengths with in 350nm-550nm (Lozano, Yip & Hanson, 1992). The idea is that, for two optically thin mixing fluids, acetone vapour is added to one. When the flow is illuminated by a laser at the appropriate wavelength, the acetone will fluoresce proportional to its concentration. This provides a map of concentration across the image of the flow. Because the emission lifetime is relatively short, 4ns (Lozano, Yip & Hanson, 1992), high resolution images of the flow can be taken provided the camera used could take sufficiently short exposures. By taking calibration images of the saturated fluid and the background, a scale can be generated to map the local density of the flow. This is possible because the florescence efficiency is largely independent of temperature, pressure and mixture composition so that the

image intensity is directly proportional to the composition of acetone vapour (Lozano, Yip & Hanson, 1992). With a two dimensional density map of the flow, it is possible to generate local stability values such as the Atwood number as well as determining the level of mixing for a given region. With values such as these the experiment can be analysed in terms of buoyancy or inertially dominated flow regimes. Also, the level of mixing can aid in determining the dissipation range of the small scale turbulent mixing.

B.3 Apparatus and Experiment

The experimental apparatus consists of a large vertical tunnel 5m long with a cross sectional area of 0.5m $\times$ 0.5m = 0.25m^2, open to the room on one end and driven by a fan on the other (Figure B.1). A flow controller, consisting of a honeycomb type mesh, is used far upstream in order to eliminate strong ambient perturbations in the inflowing air Gerashchenko & Prestridge (2015). Below this flow controller, a pipe is positioned in the centre of the tunnel providing the inflow for the jet. This inflow pipe has an inside diameter of 1.1cm, or one jet diameter (d_0=1.1cm) and is positioned in such a way as to reduce fluctuations in the tunnel flow caused by the pipe at the jet nozzle. Below the pipe is the observation section of the experiment consisting of nine removable panels spanning a vertical distance of 1.5m around the jet nozzle. These removable panels are on three of the four side walls of the tunnel and allow for transparent plates to be positioned at various distances along the jet. Three side walls needed to be transparent to allow for the laser light to enter the tunnel and for the PIV and PLIF cameras to simultaneously view the illuminated plane. Acetone vapour was used as a tracer of the jet for the PLIF images and diethylhexyl sebacate was used to produce the tracer particles necessary for the PIV. A more detailed description of the experimental apparatus can be found in Gerashchenko & Prestridge (2015) with some minor changes. The experiment was run with two jet fluids at fixed Reynolds number and varying Atwood number, sulphur hexafluoride (SF6) gas and air. The SF6 and acetone mixture has a density of 4.1kg/m^3 whereas the co-flowing air has a density of 0.94kg/m^3 providing an Atwood number of $A = 0.6$ (Gerashchenko & Prestridge, 2015). For the air jet the air acetone mixture had density of 1.13kg/m^3 producing an Atwood number of $A = 0.1$ (Gerashchenko & Prestridge, 2015). Two gases were used in this experiment in order to isolate the effects of variable density turbulent mixing (SF6 case) as compared to turbulent mixing with out strong density

differences (air case). This allows for the buoyancy and variable density effects to be distinguished from the effects of normal turbulent mixing. For each case 10,000 data points consisting of PIV and PLIF data were taken at $2.2d_0$, $16.2d_0$ and $30.0d_0$ from the jet nozzle. This large data set provides a solid foundation in which to base the flow statistics.

TSI PowerView Plus 11Mpx cameras used for both the PIV and PLIF images. In order for the PIV and PLIF data to be roughly consistent in time the images needed to be taken with in a small time frame of each other. The PIV data requires two images to be taken in order to determine the velocities and the flow must be illuminated by a 532nm laser, in this case a Nd:YAG double-pulse laser. The PLIF images were illuminated by a 308nm, XeCl excimer laser in order for the acetone to fluoresce. For this experiment the PIV images were taken before the PLIF images with exposures of 15μs and 50μs respectively (Figure B.2). Because the PIV data gives a velocity estimate at a time half way between the two images, there is a small error in comparing the densities from the PLIF images with the velocities obtained from the PIV images.

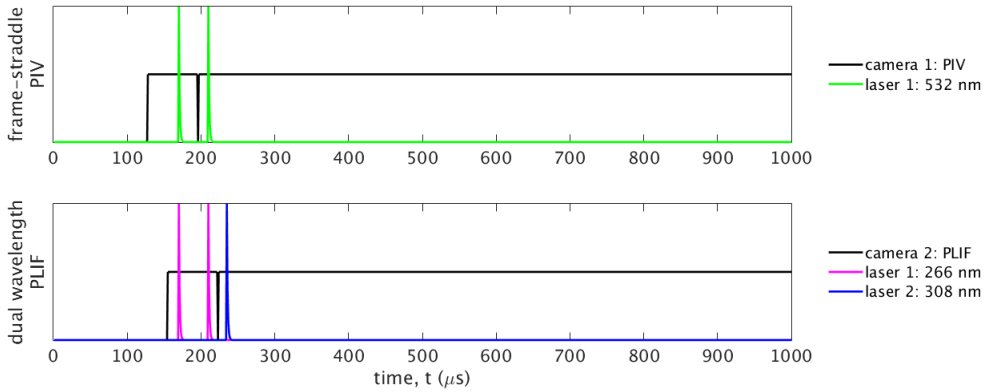

Figure B.2: Diagram of the laser pulse and camera timing. The top frame represents the PIV acuisition timing were the green line represent the laser pulses and the black line represents the camera shutter being open (value) or being closed (no value). The 266nm pulse was produced by the Nd:YAG laser and can also be used for PLIF measurements but that was not done here.

Before the data from the jet was collected, calibration images were taken. Images of the background and images of a calibration box saturated with acetone for both the SF6 and air cases were collected. These images were used to calibrate the densities for the PLIF measurements. The PLIF technique maps the density of the fluids from the intensity of light incident upon the CCD in the camera. Effects such as scattering

in the tunnel and the beam profile across the image must be removed from the jet images with the use of these calibrations. The laser sheet is also attenuated by the absorption of the laser light by acetone as it travels across the tunnel. This has the effect of creating an intensity gradient across the image that is non-negatable. In order to obtain the calibration images of the acetone saturated SF6 and air, a transparent box with inflow and outflow tubes was placed in the tunnel. This box was filled separately with the air acetone mixture and the SF6 acetone mixture until fully saturated, and once the camera was warmed up, 300 calibration images were taken for each case. Darkfield images were also taken with the camera covered in order to capture the effects of heat on the CCD.

Data collection of the jet flow was performed for the SF6 jet and the air jet at a distance of $16d_0$ from the jet nozzle. The $2.2d_0$ and $30.0d_0$ cases had already been performed. 10,000 data points were taken for both cases incorporating the PIV and PLIF data. Ambient air temperature, pressure and humidity measurements where taken in the room to track variations in the inflowing air. Temperature measurements were also taken inside the tunnel itself. The final data set consists of 10,000 data point for each of the three tunnel locations comprising both PIV and PLIF data.

B.4 Conclusion

For variable density turbulent mixing, the small scale motions act to mix the fluids, changing the mean molecular weight of the flows and therefore feeding back into the large scale dynamics. In order to better understand the turbulent mixing mechanisms found in these, and other flows, it is necessary to study the small scale mixing present at these high Res, and classify it in terms of the dimensionless numbers governing the flow regimes. Once the analysis has been performed on the turbulent mixing tunnel data, the results can be used to improve turbulence models and simulations through validation techniques such as direct comparison of experimental data to simulation results.

B.5 The Kolmogorov Hypothesis

A discussion can be found in Pope (2003).

Let $G \subset \mathbb{R}^3$ and $N \in \mathbb{N}$, where $\vec{x}^{(i)} \in G$ is a position vector at a fixed time, t, for $i \in \{0, 1, 2, ...N\}$. Let $\vec{y}^{(j)} \equiv \vec{x}^{(j)} - \vec{x}^{(0)}$ for $j \in \{1, 2, ...N\}$ where $\vec{x}^{(0)}$ is some fixed

reference point and let the velocity be given by

$$\vec{v}(\vec{y}^{(j)}) \equiv \vec{U}(\vec{x}^{(j)}, t) - \vec{U}(\vec{x}^{(0)}, t)$$

where $\vec{U}(\vec{x}, t)$ be the Eulerian velocity. The joint probability density function (PDF) of $\vec{v}(\vec{y})$ at the points $\vec{y}^{(j)}$ is denoted by f_N.

Definition: Local Homogeneity (Translational Invariance)

The turbulence is locally homogeneous in the domain G if for every fixed N and $\vec{y}^{(j)}$, the N-point PDF, f_N, is independent of $\vec{x}^{(0)}$ and $\vec{U}(\vec{x}^{(0)}, t)$.

Definition: Local Isotropy (Rotational Invariance)

The turbulence is locally isotropic in the domain G if it is locally homogeneous and the PDF is invariant with respect to rotation and reflection about the origin.

Hypothesis of Local Isotropy

Let $\mathcal{L}$ be the characteristic length of the largest flow scale. In a turbulent flow with sufficiently high Re, the turbulence is locally isotropic, if the domain G is sufficiently small such that

$$\| \vec{y}^{(j)} \| \ll \mathcal{L}$$

and is not near a boundary or other flow singularity.

The First Similarity Hypothesis:

For locally isotropic turbulence, f_N is uniquely determined by the viscosity, ν, and the dissipation rate, ϵ.

The Second Similarity Hypothesis:

let η the Kolmogorov length scale and $n \in \{1, 2, ...N\}$. If

$$\| \vec{y}^{(j)} \| \gg \eta \text{ and } \| \vec{y}^{(n)} - \vec{y}^{(j)} \| \gg \eta$$

for $n \neq j$, then f_N is uniquely determined by ϵ and independent of ν.

Bibliography

Cox J., Giuli R., Weiss A., Hillebrandt W., Thomas H., Ritter H., 1968, Reprint. Cox and Giuli's Principles of Stellar Structure. Cambridge Scientific Publishers. Print, 2005

Cushman-Roisin B., Becjers J., 2008, Introduction to Geophysical Fluid Dynamics. First Edition, Pearson Education Inc.

Denissenkov P., Herwig F., Bildsten L., Paxton B., 2012, The Astrophysical Journal, 762, 8

Ertl T., Janka H., Woosley S., Sukhbold T., Ugliano M., 2016, The Astrophysical Journal, 818, 23

Freytag B., Ludwig H., Steffen M., 1996, Astronomy and Astrophysics, 313, 497

Fryer C., 2009, The Astrophysical Journal, 699, 409

Fryer C., Belczynski K., Wiktorowicz G., Dominik M., Kalogera V., Holz D., 2012, The Astrophysical Journal, 749, 91

Fryer C., Young C., 2007, The Astrophysical Journal, 659, 1438

Gerashchenko, Prestridge K., 2015, Journal of Turbulence, 16, 1011

Grevesse N., Noels A., 1993, in Origin and evolution of the elements, Pratzo N., Vangioni-Flam E., Casse M., eds., p. 15

Herwig F., 2000, arXiv preprint astro-ph/0007139

Herwig F., Freytag B., Hueckstaedt R., Timmes F., 2006, The Astrophysical Journal, 642, 1057

Herwig F., Woodward P., Lin P., Knox M., Fryer C., 2014, The Astrophysical Journal Letters, 792, 5

Jones S., Andrassy R., Sandalski S., Davis A., Woodward P., Herwig F., 2016, MNRAS, 465, 2991

Jones S., Hirschi R., Pignatari M., Heger A., Georgy C., Nishimura N., Fryer C., Herwig F., 2015, Monthly Notices of the Royal Astronomical Society, 447, 3115

Kippenhahn R., Weigert A., 1990, Reprint. Stellar Structure and Evolution. Springer Verlag Berlin Heidelberg. Print, 1994

Langer N., Fricke K., Sugimoto D., 1983, Astronomy and Astrophysics, 126, 207

Lovegrove E., Woosley S., 2013, The Astrophysical Journal, 769, 8

Lozano A., Yip B., Hanson R. K., 1992, Experiments in Fluids, 13, 369

Meakin C., Arnett D., 2006, The Astrophysical Journal, Letter, 637, L53

O'Connor E., Ott C., 2011, The Astrophysical Journal, 730, 70

Oswalt T. D., Barstow M. A., 2013, Planets, Stars and Stellar Systems. Springer Science, Business Media Dordrecht

Paxton B., Bildsten L., Dotter A., Herwig F., Lesaffre P., Timmes F., 2011, The Astrophysical Journal Supplement Series, 192, 35

Paxton B. et al., 2013, The Astrophysical Journal Supplement Series, 208, 43

—, 2015, The Astrophysical Journal Supplement Series, 220, 44

Pitsch H., 2015, Annual Review of Fluid Mechanics, 38, 453

Pope S., 2003, Turbulent Flows. The Press Syndicate of the University of Cambridge. Print, 2005

Rauscher T., Heger A., Hoffman R., Woosley S., 2002, The Astrophysical Journal, 576, 323

Rosvick J., VandenBerg D., 1998, The Astronomical Journal, 115, 1516

Roxburgh I. W., 1989, Astronomy and Astrophysics, 211, 361

Schwarzschild M., 1958, Structure and Evolution of Stars. Dover Publications, Inc.

Sukhbold T., Ertl T., Woosley S., Brown J., Janka H., 2016, The Astrophysical Journal, 821, 45

Sukhbold T., Woosley S., 2014, The Astrophysical Journal, 783, 10

Woodward P., Herwig F., Lin P., 2015, The Astrophysical Journal, 798, 49

Woosley S., Heger A., 2007, Physics Reports, 442, 269

Woosley S., Heger A., Weaver T., 2002, Reviews of modern physics, 74, 1015

Woosley S., Weaver T., 1988, Physics reports, 163, 79